UNIVERSITY OF OKLAHOMA

GRADUATE COLLEGE

TECHNIQUES AND INSTRUMENTATION FOR PHASED ARRAY CALIBRATION

A DISSERTATION

SUBMITTED TO THE GRADUATE FACULTY

in partial fulfillment of the requirements for the

Degree of

DOCTOR OF PHILOSOPHY

By

RODRIGO MANUEL LEBRON GARCIA
Norman, Oklahoma
2020

TECHNIQUES AND INSTRUMENTATION FOR PHASED ARRAY CALIBRATION

A DISSERTATION APPROVED FOR THE
SCHOOL OF ELECTRICAL AND COMPUTER ENGINEERING

BY THE COMMITTEE CONSISTING OF

Dr. Jorge Luis Salazar-Cerreño, Chair

Dr. Caleb Fulton

Dr. Tian-You Yu

Dr. Boon Leng Cheong

Dr. Cameron Homeyer

To my parents, Andín and Leli, and to my beloved grandmother, Elvira

Acknowledgements

I would like to thank the following people who have helped me during this journey: my advisor, Professor Jorge Salazar, for his wise guidance through this research. His never-ending persistence, and passion for research motivated me to move forward despite the difficulties of experimental science; My mentor, Pei Tsai, for her spot-on questions and constructive criticism that helped to keep me on the right track; Professor Caleb Fulton, for the valuable insights regarding mutual coupling calibration that he shared with me.

I would also like to thank my fellow PhD students and friends, including: José Díaz, Javier Ortiz, Arturo Umeyama, Dr. Robin Irazoqui, Andrew Byrd, and Shajid Islam, for taking the time to discuss concepts and ideas with me and sharing their friendship with me, making my time in the lab more enjoyable; the members of the Phased Array Antenna Research and Development (PAARD) group, especially Thomas Brachtenbach and Kevin Constien, for helping me to perform the experiments presented in this work; Dr. Nafati Aboserwal, who was always eager to explain antenna concepts and theory to me; and Monica, for her love, company, and patience during my long study sessions. I would not have carried on if it was not for her immense emotional support.

The author would also like to acknowledge the support of the Advanced Radar Research Center (ARRC) for lending its facility and state-of-the-art antenna range, and the support of the Earth Observing Laboratory at the National Center for Atmospheric Research (NCAR), for providing the phased array test-bed and the custom-made antenna scanner utilized in this dissertation.

Table of Contents

List of Tables

List of Figures

Abstract

Active phased arrays suffer the inherent problem of excitation errors, i.e., incorrect phase and amplitude excitation of the antenna elements. Excitation errors degrade critical performance parameters since they increase sidelobe level and reduce antenna gain and beam pointing accuracy. To ensure the correct operation of the array, it is necessary to quantify and compensate the phase and amplitude errors of each antenna element. The compensation is accomplished by calibrating the phased array radar. Calibration challenges include the quantification and compensation of errors initially, as well as maintenance of the calibration state once the system is fielded. This dissertation presents research on improving the calibration of the active phased array front-end for radar systems. A combination of custom-made instrumentation with initial and in-situ calibration techniques is proposed to calibrate an active array test-bed. The test-bed consists of an 8×8 elements C-band array, and was developed in collaboration with NCAR-EOL to provide software and hardware features that enable the proposed calibration schemes.

Different calibration techniques were experimentally tested. First, an initial calibration technique for phased array prototypes is proposed. The technique employs a planar NF scanner to sample the excitation of each antenna element, and also to scan the embedded element antenna patterns of the prototype. The novelty of the approach is that it combines the collected excitation data with the scanned embedded elements to allow the prediction of both the co- and cross-polar pattern components of the array. On the other hand, to explore techniques that do not rely on external equipment and use built-in feedback mechanisms instead, mutual coupling-based calibration is reviewed and implemented. Two techniques were tested: an initial type, proposed by

Bekers et al., and a proposed in-situ type, conceived specifically for analog architectures, to track errors during fielded operation. It was found that mutual coupling calibration techniques are excellent options for in-situ applications, with a root mean squared error (RMSE) in phase and amplitude of 0.75° and 0.12 dB, respectively. Whereas, for initial type calibration, the tested mutual coupling-based technique yields a RMSE of 2.5° and $\geq$ 1 dB, respectively, which is not accurate enough to replace conventional park and probe for initial calibration of small arrays. Finally, to complement calibration theory, the required calibration instrumentation is reviewed, and more importantly, a novel scanner, designed exclusively for phased array front-end characterization, is introduced.

1 Introduction

1.1 Problem Statement

Phased array antennas are formed by a set of antenna elements that are coherently excited to obtain a desired beam pattern [1]. Their most important advantage is the possibility of producing a directive beam in a target direction by carefully choosing the phase excitation of each antenna element. Moreover, by electronically controlling the excitation of the antenna elements, it is possible to quickly steer the beam radiated by the array. This capability is especially attractive for radar applications, which is the motivation for modern radar systems to incorporate this technology.

Also, it is known that phased arrays suffer from inevitable excitation errors [2, 3, 4]. These errors occur due to hardware imperfections, as improper fabrication of the transmission lines and/or active components will result in deviations in the length of the electrical paths from their ideal value. The deviations cause the antenna elements to be fed with incorrect phase and amplitude values, adversely affecting the antenna pattern of the array. Furthermore, imperfections in the antenna aperture may cause aberrations in the patterns produced by an antenna element. Critical performance parameters such as side lobe level, antenna gain, and beam pointing accuracy are degraded as a result [5]. Therefore, it is necessary to assess and, when possible, correct the excitation and antenna element pattern errors perturbing the array.

The procedure that quantifies the excitation of an array is known as "calibration" [6]. The goal is to estimate the realized phase shift and gain of each antenna element with respect to each other, and then reconfigure the excitation hardware to a proper set of values. The literature regarding calibration is vast

and varied, and there is no universally accepted calibration technique. The criterion to select one technique over another depends upon the array architecture and size, and the available instrumentation setup. Moreover, sampling only excitation errors may not suffice to ensure a thorough assessment of the array performance; ultimately, it is necessary to evaluate the resulting beam pattern. As a consequence, from the point of view of the test engineer, it is crucial to define a basic guideline that specifies the necessary steps in order to assess the performance of a phased array, considering both excitation and antenna patterns

In addition, any calibration procedure implies the employment of specialized hardware to serve as a feedback mechanism that enables the output signals of the system to be sampled. The most common instrumentation for this purpose is an antenna test range, which consists of a robotic antenna or probe positioning system, and a vector network analyzer (VNA), typically enclosed in an anechoic chamber [7]. Although antenna ranges mainly function to scan antenna patterns, they can be repurposed to allow excitation sampling as well. However, there are certain disadvantages associated with their employment; for instance, since they are not primarily defined for calibration, they require software and/or hardware modifications to comply with calibration requirements. Also, because they are sizable and massive, they are not an option for calibration once the phased array system has been deployed. Two issues arise from these disadvantages. First, specialized instrumentation for phased array characterization is limited and needs to be further developed. Second, calibration during deployed operation represents a technological challenge that can not be solved by employing typical antenna ranges.

In this context, this study focuses on the fundamentals of phased array

calibration. It attempts to define guidelines on how to collect and process the data required to assess the performance of phased arrays. Also, it reviews the current state-of-the-art calibration hardware and introduces a novel robotic tool dedicated to phased array calibration, with improved and unique features that are key for a full characterization. Lastly, it investigates the limitations of current on-site calibration mechanisms, and proposes an in-situ type calibration technique. More importantly, all of the aforementioned objectives are tested and verified by experimental methods.

1.2 Motivation

Challenging projects are currently in development to construct the new generation of radar applications, and the phased array antenna has been chosen as their backbone. A notable example is the multifunction phased array radar (MPAR) initiative that aims to merge the current capabilities of aircraft surveillance and weather observation in the United States into a single network of novel phased array radars [8]. The endeavor has been undertaken by the National Weather Service (NWS) and the Federal Aviation Administration (FAA), who have joined efforts to define the MPAR requirements. A critical requirement is dual polarization capability [9, 10], which is much needed for hydrometeor classification in weather observations. However, dual polarized phased array radar for weather applications is a relatively new technology, with only a few previous publications [11, 12]. Thus, it requires more research on the subject to evolve into a more mature stage, and eventually, be suitable for the MPAR project.

Dual polarization capability on phased array radars is indeed a technology challenge; Zrnic and Doviak, and Wang and Chandrasekar [13, 14] summarized

an extensive list of performance requirements, and among them is the need for an isolation of -35 dB or better between polarizations. This requirement translates into a very low cross-polarization of the antenna aperture. For this tight tolerance, and others, the NWS requested the Massachusetts Institute of Technology Lincoln Labs (MIT-LL) to cooperate on an advanced technology demonstrator (ATD) [15, 16]. The ATD serves as a prototype to further study the dual polarized performance of phased array radars, including both front-end and back-end. Recently, Conway et al. [17] summarized the ATD evolution, and emphasized calibration efforts to tune the system. The ATD antenna panel plus front-end have been exhaustively tested on a custom made 5 m $\times$ 5 m NF chamber as part of this effort, as shown in Figure 1.1. The test efforts on the ATD described by Conway et al. represent an excellent example of the need for calibration of phased array radars, and it is especially important when assessing the polarization purity of dual polarized radars.

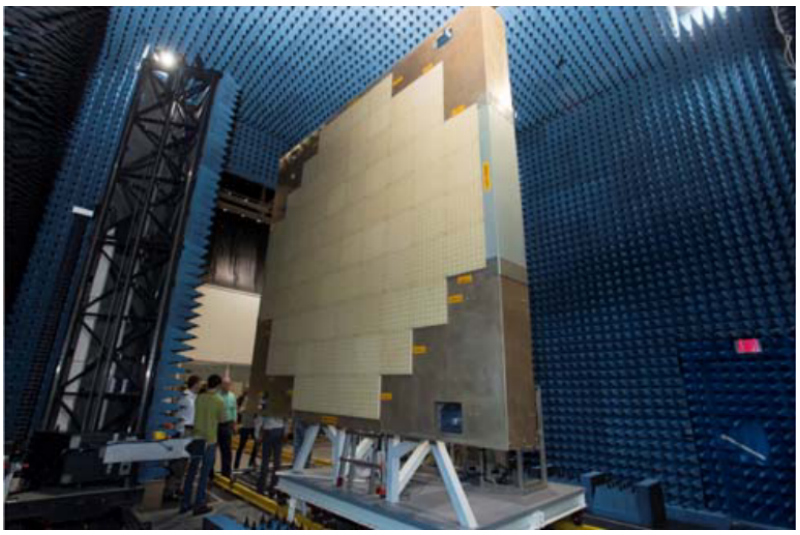

Figure 1.1: ATD antenna panel located on a custom made NF test chamber. Source: [17]

Another ambitious project is the development of a novel airborne phased

array radar (APAR) for weather observations [18]. The idea has been conceived by the Earth Observing Laboratoary (EOL) hosted at the National Center for Atmospheric Research (NCAR) and basically consists in mounting a dual polarized phased array radar, and a set of other sensors, on a research airplane to perform 3D wind and microphysical measurements. The proposal is illustrated in Figure 1.2. In this case, an integrated sidelobe level (ISL) of $\leq$ -65 dB is required [19], which is intended to be realized by amplitude taper of the array aperture in both receive and transmit modes. It is in the interest of NCAR-EOL to perform calibration and characterization of their phased array radar to ensure that the sidelobe levels are within the required levels. Moreover, due to the use of solid state high power amplifiers (HPAs) plus attenuators for phased array applications, a taper will generate an unwanted heat dissipation gradient across the antenna aperture, which may affect the radiation pattern of the array. It is understood then that heat distribution over the aperture is a concern, and it must be taken into consideration while characterizing a phased array.

As part of the APAR project, NCAR has built a line replaceable unit (LRU) prototype, consisting of an 8×8 active phased array, used to investigate the calibration requirements for the upcoming APAR project. The goals of the study are to define the steps to perform a complete assessment of the radiation patterns of the LRU, and to explore techniques that allow monitoring and correction of excitation errors during flight operation. To accomplish these goals NCAR has teamed up with the Phased Array Antenna Research and Development (PAARD) group hosted at the Advanced Radar Research Center (ARRC), which has lent its vast phased array expertise, together with its antenna ranges, to perform pattern measurements of the LRU. This col-

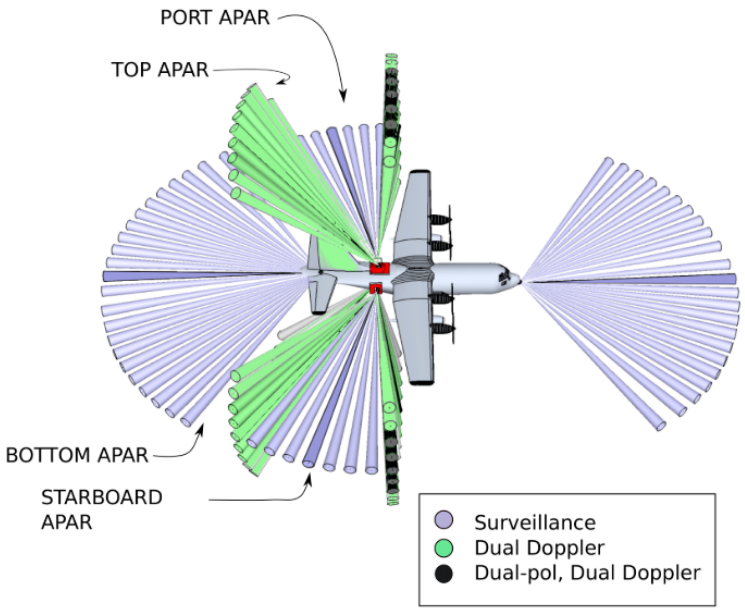

Figure 1.2: Proposed phased array radar arrangement of APAR. Source: [18]

laboration is one of the main motivations of this dissertation, which seeks to fulfill the research objective defined by the NCAR-EOL/PAARD-ARRC collaboration.

On the other hand, for the mmWave frequency spectrum, the upcoming fifth generation (5G) of communication technology has found phased array antennas to be a feasible option to satisfy its technical demands [20]. As a consequence, a great number of devices for mobile communication started to implement phased array technology, e.g., massive multiple input multiple output (MIMO) systems [21]. In addition, the automotive industry is also venturing into the implementation of mmWave phased array radars aiming to improve safety [22], and, ultimately, advance towards the longed-for self-driving capability. As a result, both industries are dedicated to developing a multitude of phased array prototypes, which, as in the case of MPAR and APAR, also require performance assessment and calibration.

1.3 Research Scope

The main motivation of this work is to provide guidelines on how to perform measurements to test phased array radar prototypes for the APAR and MPAR initiatives. Taking this into consideration, the proposed research aims to explore characterization and calibration techniques for phased array radars, and evaluate their implementation on prototypes.

The first step to accomplish this goal is to define suitable antenna measurement instrumentation to carry out the measurements. This requires reviewing the state-of-the-art of antenna ranges, and identifying the configuration that offers more benefits for phased array calibration. Moreover, as an effort to prepare for future phased array prototype testing, a novel automated tool is proposed. The proposed tool, named "RF Scanner", is based on an articulated robotic manipulator that has a suite of sensors attached onto its end. The sensor suite allows for RF sampling, surface inspection and thermal imaging of the antenna aperture. The robotic manipulator and sensor suite are placed inside an environmental chamber that enables control of the ambient temperature and humidity under which the tests are executed.

Once the equipment has been introduced, it is possible to direct attention to the calibration procedure. This study covers the complete calibration of a phased array, which includes initial calibration (exhaustive testing immediately after manufacture) and in-situ calibration (monitoring the current state of the array during fielded operation). The LRU prototype provided by NCAR is used as the device under test (DUT). Different calibration techniques are implemented on it, and their performances are evaluated.

For the initial calibration case, a measurement approach is needed that will allow a complete assessment of the performance of the phased array prototype.

The approach should detail all the necessary data to be collected to fully describe the antenna patterns synthesized by the LRU, and it should serve as a guide for initial calibration. Since antenna patterns are required for complete characterization, the measurement approach must also define the suitable antenna range configuration to perform it.

Next, to achieve in-situ calibration, it is necessary to explore testing instruments that do not rely on external equipment, i.e., the instrumentation should be built into the phased array system itself, and thus it can be performed regardless the deployment location. Consequently, this work applied mutual coupling-based calibration techniques, experimentally with the goal of evaluating the effectiveness of this feedback mechanism to estimate the excitation errors between antenna elements. More importantly, in order to comply with the constraints imposed by the LRU hardware, a hybrid technique was formulated by combining two other techniques. The propose hybrid mutual coupling technique provides a procedure to monitor the excitation of the active elements with respect to its initial state, obtained by a previous calibration effort.

Apart from the useful excitation estimation obtained from the mutual coupling-based techniques, it was also found that the raw data from mutual coupling data is extremely useful for quick diagnosis of element malfunction. In fact, the data collected using this mechanism not only detects element malfunction, but it also identifies its cause. Thus, this work describes a rationale ultimately leading to the identification of failed hardware components.

1.4 Contribution

This work focuses on the practice of measuring active phased arrays for performance assessment and excitation correction. It first describes the instrumentation required to measure the beam antenna patterns and excitation values of each antenna element. Then, different phased array calibration techniques are reviewed, tested, and experimentally validated. More importantly, improvements over the current state-of-the-art of instrumentation and calibration techniques were also proposed and demonstrated. These contributions are listed as follows:

- Propose and build a novel robotic phased array calibration tool, with environment temperature control and thermal imaging capabilities.
- Propose and experimentally validate a complete measurement procedure for performance assessment of phased array prototypes.
- Experimentally test a mutual coupling-based calibration technique that has only being validated by means of computer assisted simulations.
- Propose and experimentally validate a hybrid mutual coupling-based calibration technique for on-site monitoring of element excitation.
- Describe a methodology to diagnose hardware component failure using mutual coupling measurements.

A notable contribution of this work is the advancement of mutual coupling-based calibration techniques. The experiments conducted of this type of calibration provide valuable insights related to performance, such as estimation accuracy and feasibility depending on the hardware on which it is implemented. The techniques are discriminated in initial and in-situ types, and their corresponding accuracy is experimentally obtained in terms of root mean squared errors of phase and amplitude. Their feasibility is investigated under the

presence of edge effects. To the knowledge of the author, there are no prior publications that have experimentally tested the techniques implemented in this work.

Furthermore, the implemented in-situ type technique is a novel hybrid mutual coupling-based technique proposed by the author. It is conceived to provide fast and accurate phase and amplitude error tracking during field operation of phased arrays with analog beamformers. A main advantage of this technique is that it uses the active antenna elements themselves to perform the measurements, while at the same time being unaffected by edge effects. Results demonstrate that this technique provides better estimations than the initial type technique, which was also implemented.

During the experiments employing the aforementioned techniques, failure cases were detected. Failed antenna elements provide wrong data for calibration, and they compromise the estimations. For this reason, this work introduces a rationale capable of detecting failed antenna elements and identifying the hardware component that caused failure using mutual coupling measurements. This offers two advantages: first, since it is possible to quickly determine the health of the antenna elements, an antenna element found to be damaged may be excluded from calibration tests. Second, because the mutual coupling data contains information about the cause of the failure, the technique reduces failure diagnosis time and reduces the number of extra tests required to identify the failure cause.

To complement the presented mutual coupling techniques, and to offer a beginning-to-end solution for phased array calibration, improvements over current instrumentation and conventional techniques are also presented. For the instrumentation, a novel flexible scanner, based on a robotic arm manipulator,

is built and preliminarily tested. The scanner is designed specifically for the purpose of characterizing the performance of phased array prototypes. The scanner has the unique capability of allowing testing under different operation temperatures and scan geometries.

Finally, a complete step-by-step procedure on how to initially calibrate and verify correct operation is proposed and implemented. The procedure employs a NF planar scanner to perform both the park and probe calibration technique and scan antenna pattern measurements. The novelty of the proposed technique is that it combines the collected data of the TR modules, obtained by park and probe, and combines the data with the embedded element antenna patterns scanned by the scanner to calculate the resulting antenna array pattern. In other words, by exhaustive measurements of the antenna under test, enough information is obtained to predict any possible antenna beam pattern the prototype may synthesize.

1.5 Dissertation Overview

This dissertation is divided into five additional. Chapter 2 reviews the fundamentals of phased arrays and their calibration. It also uses an analytically simulated uncalibrated phased array pattern to illustrate the "misalignment" problem. Finally, a summary of the state-of-the-art of the calibration techniques is presented. Chapter 3 presents the instrumentation required for antenna measurements, including the equipment employed for the experiments performed in the next chapters. In addition, it also presents the novel robotic scanner designed specifically for calibration.

Chapters 4 focuses on calibration experiments using instrumentation external to the phased array system. It introduces the proposed methodology for

a complete initial calibration, and discusses the results of its implementation on the LRU using a planar NF antenna range. By contrast, Chapter 5 is dedicated to calibration techniques based on mutual coupling measurements, so it studies techniques that do not require external equipment. Initial and in-situ techniques are implemented on the LRU, and its misalignment estimations are compared to the results obtained from the more reliable calibration technique discussed in Chapter 4. In addition, it also describes how the raw mutual coupling data can be ingeniously analyzed to identify damaged components.

Finally, Chapter 6 summarizes the findings from each experiment, and presents the conclusions. Afterward, as a complement, the appendixes include technical details about NF planar measurements, including a list of abbreviations used in this dissertation.

2 Fundamentals of Phased Array Antennas and Calibration

2.1 Phased Array Antennas

2.1.1 Definition

A phased array antenna is a collection of antennas that are coherently excited in order to synthesize an antenna pattern. Each antenna of the array is denominated an antenna element. If the antenna elements are excited with a set of carefully chosen phase values, the main beam of the realized pattern can be steered to a target angular coordinate.

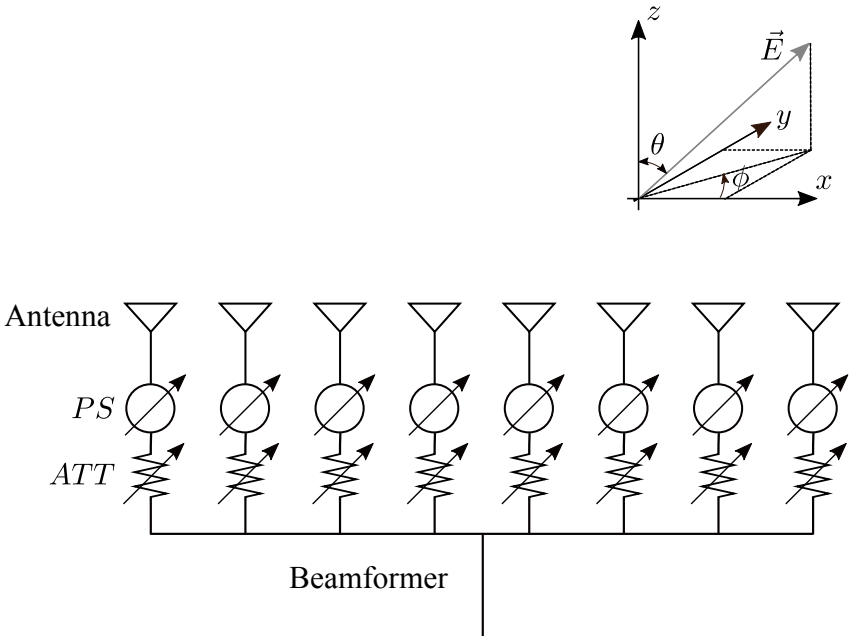

Figure 2.1: Basic architecture of the front-end of an active phased array antenna.

Figure 2.1 shows the basic components of an electronically steered phased array with analog beamformer. Each antenna element is connected to two variable microwave components, a phase shifter (PS) and an attenuator (ATT).

The phase shifter allows modification of the phase of the signal fed to the antenna element, while the attenuator, as the name indicates, attenuates the signal, changing its amplitude. The combined effect of both hardware components is equivalent to a multiplication of the signal by a complex weight defined by the configuration of both components. The phase is often controlled to define the steering angle, whereas the amplitude chosen tapers the aperture excitation of the array, which can reduce the sidelobe level (SLL). Finally, the feed network that excites the antenna elements is called the beamformer, which in the case of Figure 2.1, is of analog architecture. All the signals are added in complex domain on the beamformer, and the result is a single complex signal combining the effects of all elements.

2.1.2 Pattern Synthesis Equation

Lets examine the simple case of an N-element array in a linear or planar arrangement. The radiation pattern of the complete array is equal to the superposition of all radiated fields from each antenna element. If $f_n(\theta, \phi)$ represents the far field (FF) pattern of the nth antenna element, with origin in the center of the antenna element, as a function of the observation angles in spherical coordinates θ and ϕ, then the array radiation pattern will be equal to the sum of the complex values of $f_n(\theta, \phi)$ for all N patterns, with a phase-correction consideration due to the spatial offset given by the position of the element with respect to the phase center. This can be mathematically expressed [23] as

$$f_a(\theta, \phi) = \sum_{n=1}^{N} f_n(\theta, \phi) e^{-jk\hat{\mathbf{r}}\cdot\mathbf{r}_n}, \tag{2.1}$$

where $f_a(\theta, \phi)$ is the pattern of the array, $k = 2\pi/\lambda$ is the wavenumber, λ is the wavelength, $\hat{\mathbf{r}}$ is the unit vector in the θ and ϕ direction, defined as

$$\hat{\mathbf{r}} = \sin\theta\cos\phi\hat{\mathbf{x}} + \sin\theta\sin\phi\hat{\mathbf{y}} + \cos\theta\hat{\mathbf{z}}, \tag{2.2}$$

and finally, $\mathbf{r}_n$ is the position vector of the center of the nth element from the phase origin of the array. The phase correction term is given by $e^{jk\hat{\mathbf{r}}\cdot\mathbf{r}_n}$. Boldfaced notation indicates a vector quantity.

If the possibility of manipulating the phase and amplitude of the excitation of the individual elements is added, each $f_n(\theta, \phi)$ pattern will be multiplied by a complex gain w_n. Consequently, (2.1) can be updated to

$$f_a(\theta, \phi) = \sum_{n=1}^{N} f_n(\theta, \phi) w_n e^{-jk\hat{\mathbf{r}}\cdot\mathbf{r}_n}, \tag{2.3}$$

where,

$$w_n = A_n e^{j\psi_n}, \tag{2.4}$$

w_n is the complex weight assigned to the nth element, A_n is the amplitude attenuation, and ψ_n corresponds to the phase shift. In an analog active phased array, this weight is often realized by the phase shifter and attenuator in the TR module of the nth element.

In the array calibration context, the excitation values w_n can be seen as the actuators that allow the user to compensate the errors introduced by the RF components of the system. As will be seen during the description of the calibration techniques, the phased array calibration focuses on determining the excitation values that would yield the desired array pattern.

2.2 The Misalignment Problem

If the phase shift and amplitude applied to the excitation of the active antenna elements of a phased array antenna are incorrect, then the array is "misaligned". Misalignment has a detrimental effect over the resulting beam pattern, and can degrade performance parameters such as SLL, gain, and beam point accuracy [5].

The excitation errors that cause the misalignment are categorized as random or systematic [3]. Random errors are related to manufacturing tolerances, component aging, and non-uniform transmission line lengths, which translate into independent phase and amplitude excitation errors between elements. On the other hand, systematic errors are highly correlated, and they present some sort of pattern, e.g., periodic errors due to quantization, often produced by employing digital phase shifters or attenuators. In addition, the adverse impact of systematic errors is often far greater than the impact of random ones. For this reason, it is desired that calibration remove systematiic errors such that an array will be affected only by random errors post calibration.

To illustrate the effect of excitation errors, and the difference between the impact from random and systematic types, a simulation of array patterns is used. The simulated array geometry is a 64×64-elements planar array. It has a square lattice employing a $d = \lambda/2$ separation distance between elements. The antenna elements are assumed to have an isolated pattern of $f_n = \cos\theta$, similar to infinitesimal ideal dipoles. The beam is pointed at -45° in azimuth, and a Chebyshev taper of -40 dB is applied.

First, the expected pattern for this array configuration is simulated using (2.1). Afterwards, two misalignment cases are simulated, one perturbed by random errors, and the other by systematic errors. For the random errors

case, the phase and amplitude of all elements were given an error with gaussian distribution, as depicted in the top left part of Figure 2.2.(a). The root mean squared error (RMSE) in phase is 10°, and in amplitude is 1 dB. By contrast, for the systematic error case, it was assumed that the antenna elements located on the same column have equal excitation errors. Still, the errors added to the columns for the systematic case had the same values as the ones for the random case, 10° and 1 dB.

The results of the three cases are shown in Figure 2.2. The figure shows a comparison of the effect of each error case to the expected case. Figure 2.2.(a) illustrates that the SLL is most affected, whereas the gain and beam pointing show no noticeable change. For the random errors case, the obtained maximum SLL exceeds by $\approx$ 4 dB the target SLL of -40 dB (indicated by the horizontal red dashed line). By contrast, for a systematic error, of the same RMSE order, the obtained SLL exceeds the target level by more than 10 dB, a much worse outcome. On the other hand, the 2D patterns seem to indicate that the systematic error case, shown in Figure 2.2.(b).(iii), has better results than the random case, shown in Figure 2.2.(b).(ii). Indeed, the pattern shape is better for the former case, however, the systematic nature of the error adversely affected certain areas of the pattern more than others, causing more errors on a critical performance parameter, the SLL. The simulation clearly demonstrates that systematic errors are more serious than random ones.

2.2.1 Impact of Excitation Errors on Beam Patterns

After calibration and misalignment compensation are performed, the array should be affected by random errors only. Thus, it is important to link the levels of phase and amplitude random errors to corresponding maximum tol-

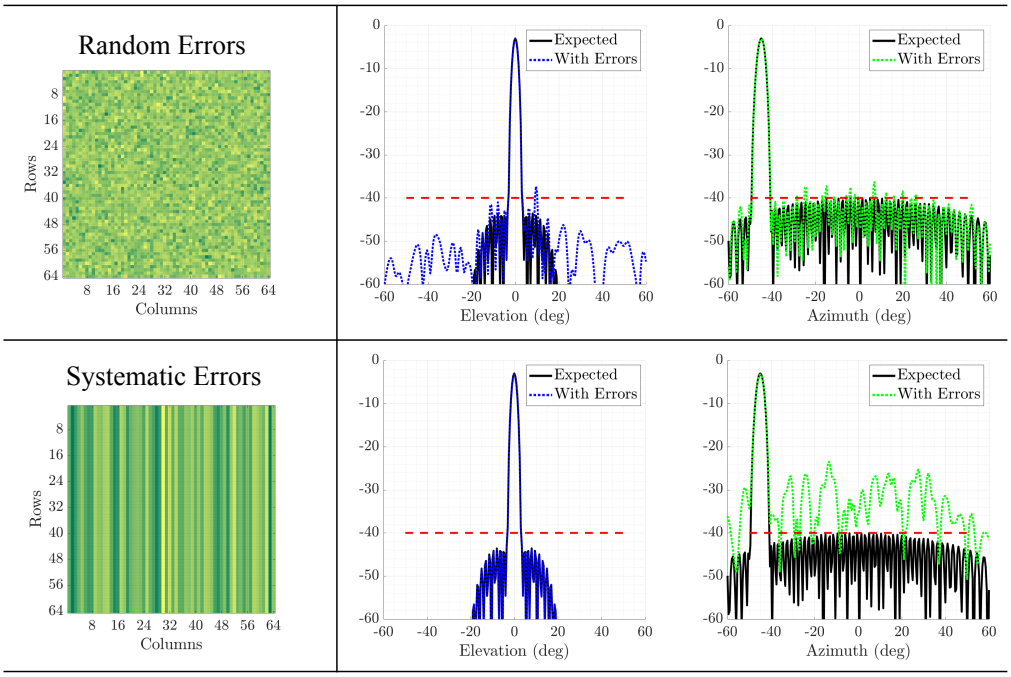

(a)

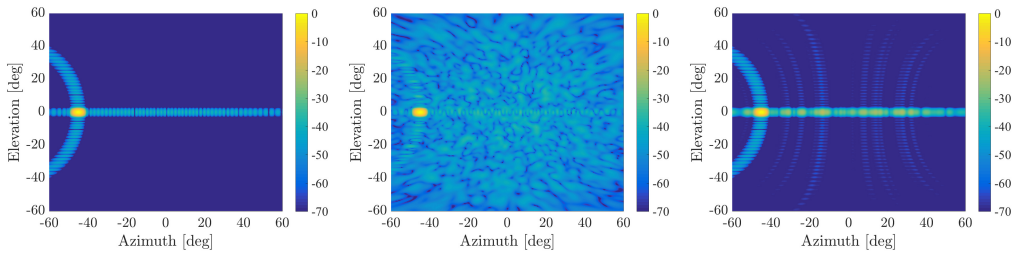

(i) Expected (ii) With random errors (iii) With systematic errors

(b)

Figure 2.2: Example of the impact of random and systematic errors on the pattern of a phased array. The random error has a gaussian distribution with a RMSE of 10° in phase, and 1 dB amplitude, whereas the systematic case assumes the same excitation error on elements that belong to the same column. (a) Elevation and azimuth cuts. (b) 2D antenna patterns.

erable errors in performance parameters, i.e., correlate random error levels to pattern deterioration. The phased array handbooks authored by Mailloux [1] and by Hansen [24] present a complete survey of the effects of random errors on the antenna pattern. This dissertation uses the theory compiled in the

aforementioned references to exemplify the misalignment effects on sidelobe levels, antenna directivity, and beam accuracy.

Before proceeding, it is important to define the magnitudes that will quantify the excitations errors so that they may serve as a metric to link misalignment error levels to their corresponding effect on the array pattern. The literature defines the root mean squared error for phase, σ_Ψ, and amplitude, σ_δ, to be their metrics, and they are calculated as

$$\sigma_\Psi = \sqrt{\frac{1}{N}\sum_{n=1}^{N}|\psi_n - \psi_n^{\mathrm{T}}|^2}, \tag{2.5}$$

and,

$$\sigma_\delta = \sqrt{\frac{1}{N}\sum_{n=1}^{N}\left(\frac{|A_n - A_n^{\mathrm{T}}|}{A_n^{\mathrm{T}}}\right)^2}, \tag{2.6}$$

respectively. N is the total number of elements of the array, ψ_n is the excitation phase of the nth antenna element, ψ_n^{T} is the target phase excitation for the nth element. In the same manner, A_n and A^{T} are the realized and target amplitudes of the nth element. Also, the amplitude error can be approximated in dB using [1],

$$\sigma_\delta^{dB} = 20\log_{10}(1+\sigma_\delta) \approx 8.68\sigma_\delta. \tag{2.7}$$

1 - Sidelobe Level

SLL is the performance parameter of a phased array beam pattern most susceptible to misalignments. Thus, the maximum tolerable misalignment level is often defined according to SLL requirements. A method to calculate the achievable SLL given certain σ_Ψ and σ_δ error values, has been proposed by Hsiao [5]. Hsiao acknowledged that the realized SLL on a phased array will be higher than the target SLL value, S^T, due to the unavoidable effect of random

errors. As a consequence, he proposed that a target SLL will be achieved by exciting the array for a lower SLL, called the designed sidelobe level, or S^d. In this manner, when the errors inevitably increase the realized SLL, they will reach the S^T value. For this, Hsiao statistically predicts the σ_Ψ and σ_δ errors allowed to not exceed S^d versus the ratio S^d/S^T, for a probability p.

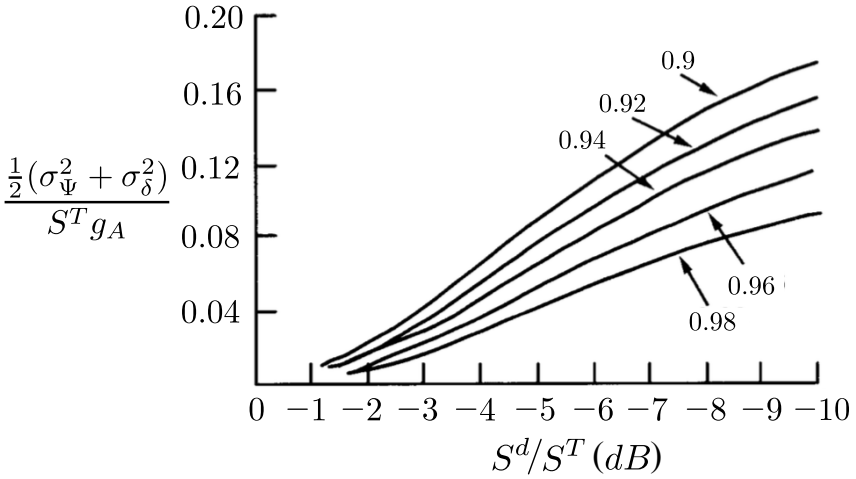

Figure 2.3: Normalized error level vs. the ratio between the designed SLL, S^d, and the target SLL, S^T. Source: Adapted from [1].

The approach by Hsiao is better described by examining its results reproduced in Figure 2.3. The abscissa of the plot, representing the ratio S^d/S^T, is always negative because S^d is deliberately chosen to be lower than S^T to compensate for the random errors effect. The ordinate represents the normalized error, given by the following:

$$\frac{\frac{1}{2}(\sigma_\Psi^2+\sigma_\delta^2)}{S^T g_A}, \tag{2.8}$$

where g_A is called the directivity of the ideal pattern with isotropic element patterns [1]. The term σ_Ψ should be given in radians, and σ_δ should be dimensionless. Each of the curves plotted in the figure represents the probability of

the peak SLL not exceeding S^T.

The value of g_A for a linear array is calculated using

$$g_A = \frac{\sum_n^N (A_n)^2}{(\sum_n^N A_n^2)}, \tag{2.9}$$

For a large planar array it can be calculated as

$$g_A = \pi g_{Ax}\, g_{Ay}, \tag{2.10}$$

where g_{Ax} and g_{Ay} are the directivities of linear arrays with lengths equal to the number of columns and rows of the planar array, respectively. Because the directivity g_A is dependent on the aperture illumination, which is defined by the taper used to yield the target SLL, g_A is a function of S^T.

The trade-offs between the involved parameters are interpreted by reading the curves. For instance, the lower the S^d is defined, the higher the errors that are admissible. This is analogous to moving to the right on the plot, which makes the normalized error greater, and thus, resulting in a higher tolerable error. Also, for a high probability of not exceeding S^d, the tolerances are tightened, which is clearly indicated by the different probability curves that yield a lower normalized error for higher probability values.

The challenge from the point of view of the array designer is to keep errors low, so the designed SLL is closer in value to the target one. This is because the lower the defined S^d, the more taper should be added to the elements, which translates to a more inefficient power aperture distribution.

To further illustrate the relation between random misalignment errors and the SLL, the expected SLL for the example shown in the previous section (2.2.1) is calculated, and the process is summarized in Table 2.1. Hsiao's

Table 2.1: Calculation of the necessary S^d/S^T ratio to obtain a target SLL S^T for a given σ_Ψ and σ_δ error level. The antenna is a planar square phased array of 64×64 elements, using a Chebyshev taper to achieve S^d.

Magnitude	**Symbol**	**Value/Unit**
RMSE phase	σ_Ψ	0.175 rad (10°)
RMSE amplitude	σ_δ	0.115 (1 dB)
Target SLL	S^T	-40 dB
Probability	p	0.98
Ideal linear array directivity	$g_{A_x} = g_{A_y}$	17.045 dB
Ideal array directivity	g_A	39 dB
Denominator factor	$S^T g_A$	-1 dB
Normalized error	$\frac{\frac{1}{2}(\sigma_\Psi^2+\sigma_\delta^2)}{S^T g_A(S^T)}$	0.028
SLL ratio (Figure 2.3)	S^d/S^T	$\approx$ -4 dB

curves indicated that for the 64×64 array example of Figure 2.2, a combined error of 10° and 1 dB will require a S^d/S^T ratio of ≈ -4 dB. This means that, in order to ensure a peak SLL of -40 dB, the designed SLL should be 4 dB less, i.e., $S^d = -44$ dB. Moreover, this result should not be a surprise, as it was found in Figure 2.2 that, for the same error level, the peak SLL is 4 dB higher than expected. Hence, both studies suggest defining S^d to be 4 dB less than S^T, which equals -40 dB.

2 - Beam Pointing

The beam pointing accuracy is the difference between the desired and realized angular location of the beam peak. It is possible to predict the beam pointing RMSE, σ_θ, for an equally-spaced linear array of N_{lin} elements, using [24],

$$\sigma_\theta^2 = (\sigma_\Psi^2 + \sigma_\delta^2)\frac{\sum_{-N_{lin}/2}^{N_{lin}/2}(A_n^{\mathrm{T}})^2 k^2 d^2 n^2}{\left(\sum_{-N_{lin}/2}^{N_{lin}/2} A_n^{\mathrm{T}} k^2 d^2 n^2\right)^2}, \tag{2.11}$$

where A_n^{T} is the amplitude of the nth element, k is the propagation constant, and d is the separation between elments. If the linear array is also uniformly excited, and large enough, $N > 10$, (2.11) can be simplified [25] to

$$\sigma_\theta = \frac{2\sqrt{3(\sigma_\Psi^2 + \sigma_\delta^2)}}{kd\cos\theta_0 N_{lin}^{3/2}}. \tag{2.12}$$

Where $\cos\theta_0$ is an extra term added to model the effect of steering the beam θ_0° off boresight.

For a square array, of dimensions $N = N_{lin} \times N_{lin}$, it can be assumed that σ_Ψ is the same as in (2.12) but averaged $\sqrt{N_{lin}}$ times [25], i.e., for a square uniformly excited array, the beam pointing error is,

$$\sigma_\theta = \frac{2\sqrt{3(\sigma_\Psi^2 + \sigma_\delta^2)}}{kd\cos\theta_0 N_{lin}^{2}}. \tag{2.13}$$

For all equations, σ_Ψ should be given in radians, and σ_δ should be dimensionless. As a result, σ_θ is given in rad.

Expressions (2.11), (2.12) and (2.13) indicate that σ_θ decreases with the number of elements in the array. Thus, the larger the array the less sensitive its beam pointing accuracy is in the presence of random errors. This behavior is accentuated in the case of a square array.

It is possible to calculate the σ_θ for the example shown in Figure 2.2 using Figure 2.13 by assuming the array is uniformly excited. As before, the errors are defined as 10° and 1 dB, and the beam is steered at $\theta_0 = 45°$. The resultant σ_θ is $4.6° \times 10^{-3}$, which is approximately half the value of the often tolerable error of 0.01° [18]. The reason for this is that the array is large enough that the error is reduced by averaging. However, if the array was linear, the error would have been increased $\sqrt{N_{lin}} = 8$ times to 0.037°, which is a large enough error to be considered. These results are summarized in Table 2.2.

Table 2.2: Calculation of the beam pointing accuracy for a given σ_Ψ and σ_δ error level.

Magnitude	**Symbol**	**Value/Unit**	
Number of elements	$N_x \times N_y$	64× 64	1×64
RMSE phase	σ_Ψ	0.175 rad (10°)	
RMSE amplitude	σ_δ	0.115 (1 dB)	
Target θ angle	θ_0	45°	
Beam point accuracy	σ_θ	$4.6° \times 10^{-3}$	0.037°

Table 2.3: Calculation of the directivity variation for a given σ_Ψ and σ_δ error level.

Magnitude	**Symbol**	**Value/Unit**
RMSE phase	σ_Ψ	0.175 rad (10°)
RMSE amplitude	σ_δ	0.115 (1 dB)
Directivity variation (2.14)	D/D_0	-0.19 dB

3 - Directivity

Skolnik [26] proposed that the directivity change may be calculated as

$$\frac{D}{D_o} = \frac{1}{1 + \sigma_\Psi^2 + \sigma_\delta^2}, \tag{2.14}$$

where D_0 is the original directivity of the antenna, i.e., the directivity expected for an array without random errors. D is the directivity resulting from errors affecting the antenna elements. Furthermore, as in the previous equations, σ_Ψ should be given in radians, and σ_δ should be dimensionless.

The change in directivity due to random errors is independent of the array size, and often its variation is almost negligible. For instance, continuing with the 64×64 example from Figure 2.2, an error of 10° and 1 dB will result in a variation of only 0.19 dB, as calculated in Table 2.3.

2.3 Calibration of Phased Array Antennas

As previously noted, misalignment errors affect the realized beam antenna pattern on a phased array. Moreover, it was illustrated that misalignment greatly increase the SLL, and it also adversely affected the beam pointing accuracy and directivity. These problems are accentuated if the error distribution is systematic instead of random. Undoubtedly, the misalignment problem can compromise the performance of a phased array-based system, so this problem needs to be addressed by the test engineer. This is the context in which phased array calibration originated.

Calibration of a phased array attempts to quantify misalignment in order to characterize the excitation error distribution. In addition, when actuation mechanisms, e.g., phase shifters and attenuators, are available, calibration serves to compensate for the measured errors.

The concept of calibration of phased arrays will be introduced by discussing the following general calibration procedure:

1. Quantify the differences in terms of amplitude and phase between the different elements of the array (misalignment).
2. Perform measurements for transmit and receive modes.
3. Repeat previous steps for all frequencies and operating temperatures of interest.
4. When TR modules (phase shifters and attenuators) are are available in the front-end of the array, repeat the calibration for each state of attenuation and phase shift combination.
5. Select a suitable configuration of phase and amplitude values based on the measured results.
6. Monitor and update the resulting calibration periodically according to

the current state of the system.

Step 1 refers to the main goal of phased array calibration, determining the misalignment between antenna elements, while steps 2-4 cover several other parameters that must be considered. Electronically steered phased arrays are composed of active microwave components that invalidate the reciprocity theorem. As a result, a transmit path is not necessarily the same as its corresponding receive path, and thus both paths must be tested. Also, the excitation errors are a function of the temperature and frequency of operation. For this reason, tests must be repeated to cover the expected temperature and frequency ranges of operation.

Step 4 concerns internal errors of the hardware associated with the TR modules. For example, the performance of phase shifters is not ideal because they incorrectly add an amplitude variation in the process of producing a phase shift [27]. This is inversely the case for attenuators, which add an unwanted phase shift while changing the amplitude. Step 4 suggests testing all possible combinations of phase and amplitude configurations in order to acknowledge the imperfections of the hardware.

Once the errors are known, step 5 explains that they must be compensated for using the sampled data. The compensation is realized through the TR module of the array, and consists of choosing a phase and amplitude configuration that is close in value to the previously defined target excitation.

The last step introduces the concept of monitoring or tracking the state of the array. Component aging and external factors, such as the temperature of operation, may introduce variations in the expected function of the TR modules or antenna aperture. Therefore, it is not enough to perform a calibration once, before the equipment is in operation. It is just as important

to periodically test if the calibration performed is holding.

The compensation part of the calibration procedure (step 5) is relatively simple. Once the errors are known, the user can simply choose a configuration more similar to the target one. However, the first part of the procedure, to quantify the misalignment errors, is not straightforward and represents an engineering challenge because it depends on both the uniqueness of the phased array hardware and on the available instrumentation to perform the measurements. In order to illustrate this problem, and simultaneously present several solutions for different cases, the current state-of-the-art on this topic is reviewed.

2.4 State-of-the-Art

The literature regarding phased array calibration is vast and diverse, and it encompasses several cases of ingenious procedures on how to sample and isolate the excitation errors of various array architectures and configurations. However, although extensive, the literature is scattered among a number of different works. Thus, readers interested in the topic are forced to study techniques from different sources in order to produce an overview of it, drawing their own conclusions. In this context, this work reviews the current state-of-the-art on phased array calibration, in an attempt to compile current challenges.

In its most simple form, the standard calibration technique, called "park and probe" [28], consists of using a Cartesian robotic manipulator to position an antenna probe in front of an antenna element of the array, and then sample the radiated field of the element. The procedure is repeated until all elements of the array are sampled. The collected data is then, compared and the differences in amplitude and phase between the elements can be calculated.

However, this technique is not universal, and is limited by implicit requirements. For instance, in order to sample only one element each time, the rest should be terminated to their corresponding matching load, which requires an extra hardware feature that allows the element to be switched between enabled and terminated states. Moreover, a robotic scanner is a bulky system that is not always available when the array is deployed for operation.

These limitations illustrate the difficulties encountered when a phased array system must be tested. The difficulties are related to the uniqueness of the hardware that must be tested and the required instrumentation to sample it. Since phased array systems have a wide variety of applications and configurations, e.g., from satellite space borne applications [29], to ground-based, fully digital radar for weather observations [30], several different techniques have been conceived to cover all these cases. In the interest of making this high number of solutions more accessible, they may be grouped under different categories. Thus, for a given application, the suitable solution could be determined by identifying the categories compatible with the application, and then choosing the technique common to all of them.

Before starting the review, two previous works that serve as introductions to the topic are worth mentioning. The first is authored by Fulton [31], which offers a review of the most relevant techniques, with a special focus on digital architecture technology, and the second by Şeker [32], which presents the fundamentals of calibration.

2.4.1 Initial and In-situ Calibration

Tthe most important criterion to consider in phased array calibration is if it can be performed during operation. Sarcione et al. [33] documented that,

for a complete calibration of a phased array radar, two procedures are needed: (1) initial calibration - exhaustively testing the equipment under controlled environmental conditions, and (2) in-situ calibration - monitoring the state of the array while in operation to ensure that the system holds its intended configuration [31]. Initial techniques are accurate, thought time consuming, and may require specialized instrumentation. By contrast, in-situ techniques must be fast, and performed under unknown external conditions.

Another calibration categorization classifies techniques according to the type of feedback mechanism employed, namely, whether or not feedback is *external* or *built-in*. External feedback relies upon instrumentation extrinsic to the system, whereas built-in feedback concerns a mechanism designed from the start to be part of the system. External types are almost exclusively implemented on initial type calibrations, due to the difficulty of installing external instrumentation once the system has been deployed. On the other hand, built-in mechanisms are particularly convenient for in-situ applications because the hardware is self-contained and already integrated into the system when deployed. Nevertheless, built-in mechanisms may also be suitable for initial calibration applications, provided these mechanisms are accurate enough to calculate the misalignment between the elements.

2.4.2 External Calibration

External types of calibration procedure are performed using near field (NF) and far field (FF) instrumentation, and thus, they can be classified into *NF* and *FF*. An example of a NF type is the aforementioned park and probe technique [28, 33, 34, 35, 36], which relies on a NF scanner to move the probe along the array to test all elements, see Figure 1.1.(a) for an illustration. Section 4.2.1

provides a detailed description of this fundamental technique. Moreover, as already described, because the performance of the TR modules is not ideal, an attempt to set the excitation to a target phase may also incur an unwanted amplitude variation, and vice-versa. As a result, in addition to considering the misalignment between elements, the error added by the imperfect operation of TR modules must also be taken into account [27, 37, 38].

FF types, depicted in Figure 2.4.(a), which utilize FF calibration towers to test the array [39, 40, 41, 42, 43] offer both advantages and disadvantages in comparison with NF types. The advantage of performing measurements at FF distances is that the sampled field is the same as that which will reach the target antenna or object. However, the signal is highly attenuated due to the long range, resulting in poor signal-to-noise (SNR) levels. In NF ranges, SNR levels are much higher. Assumptions must be made in order to correlate the sampled field in NF range to its corresponding value in FF. Further discussion about instrumentation and phased array measurements is summarized in the literature [44, 34].

2.4.3 Built-In Calibration

Built-in types can be categorized according to two main types of feedback mechanisms, *specialized* hardware or mutual coupling (MC). The specialized hardware type involves incorporating into the phased array architecture a feedback mechanism whose main purpose is testing the antenna elements. For example, Herd [45] included a closed loop feed network to inject a pilot signal into the elements, and, in a similar fashion, Lee et al. [46] added a transmission line signal injector embedded at the radiating aperture. Both mechanisms aim to introduce a known signal through the front-end of the array to detect

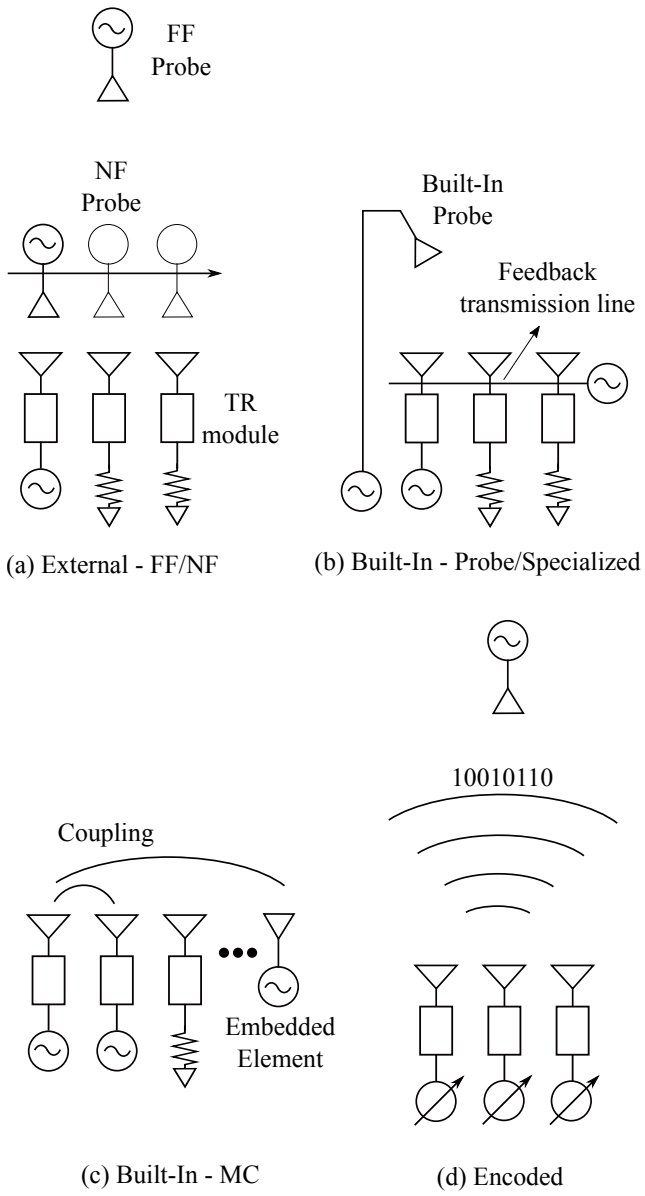

Figure 2.4: Diagrams of different calibration techniques.

errors, as shown in Figure 2.4.(b). In addition, another example using specialized added hardware relies on an on-board NF probe fixed in the NF region of the aperture of satellites [47, 48, 49].

In contrast to the specialized hardware approaches, MC-based calibration cleverly employs the inherent mutual coupling between antenna elements to

test the array using the active elements themselves as test probes, Figure 2.4.(c). The pioneer of this approach is Aumann [50], who noticed that the mutual coupling between antenna elements can be used as the feedback mechanism to sample the radiation characteristics of their neighbor elements. By quantifying this effect it is possible to estimate the performance of the array and use this information to calibrate it. Coupling between neighboring elements is measured by sending a signal from one element and receiving with another. For digital arrays this capability is built-in in its architecture. However, for an analog architecture, it is necessary to have two independent beamformers, one for transmit and another for receive, to enable simultaneous transmission from one element and reception with another.

Because both the transmission and reception networks of an array are susceptible to errors, it is necessary to use data processing algorithms to isolate transmission errors from reception errors. Additionally, because the number of possible element pairs that can be tested is very large, and increases with the number of elements in the array, a MC-based technique must unambiguously define which element pairs should be tested. The literature offers different approaches that focus on these two considerations, i.e., data processing and pair selection [51, 52, 32]. A noteworthy example has been presented by Bekers et al.[53], which presents a mathematical approach that is capable of processing as many coupling measurements as are available, resulting in a more accurate estimator than its predecessors.

The MC approach originally proposed by Aumann relies on the assumption that coupling between elements is the same as long as the pairs of elements have a similar geometrical disposition, e.g., the two couplings between an element and its left and right neighbors are the same. This assumption holds only

when the array is large. But for small arrays, the discontinuities occasioned by the edges render the assumption invalid.. To avoid this assumption, another approach for MC measurements has been proposed by Agrawal and Jablon [54]. The technique can be described as a "before/after" concept. First, MC samples of the calibrated system are performed and stored as a "before" state. Next, when the system is deployed, the "after" state is sampled. The errors are obtained by comparing both states. To perform the MC measurements, Agrawal and Jablon suggest using embedded elements for the sole purpose of testing the antenna elements. Examples of this approach are presented in [23, 33], which combine the MC technique for in-situ calibration purposes with the park and probe technique for initial calibration.

To this point the cases studied have been suitable for analog architectures, without mention of digital architectures. Nevertheless, MC-based calibration techniques are particularly convenient for the latter since an MC sampling capability is inherent to them. Proof of this is the work of Fulton [55], who conceived a robust before/after MC approach to calibrate digital arrays without using embedded elements. Moreover, Mitchell [56] proposed a full calibration of digital arrays by combining the work by Beckers et al.[53], for initial calibration, with the before/after approach from Fulton [55], for in-situ applications.

2.4.4 Encoded Calibration

A great portion of the methods cited above require the tested elements to be excited while the rest are terminated to their corresponding matching load. However, since this possibility is not always guaranteed, arrays must be tested while multiple elements are active. Under these circumstances, the signal sampled is the combination of the signals proceeding from the active

elements, which represents a problem to the test engineer, who must isolate them in order to compute the misalignment. A solution to this issue is to manipulate the phase of the antenna elements, and in some cases also the magnitude, according to a certain "encoding" technique. A mathematical algorithm is then used to decode the individual signals from the combined sample, as shown in Figure 2.4.(d).

Techniques that apply to this type of phase manipulation can be categorized as *encoded*. One of the oldest encoded techniques documented was proposed by Mano and Katagi [57] in 1982. The proposed technique is called rotation of the electric vector (REV), and consists of sampling power only measurements while cycling the phase shifter of an antenna element. Then, by using vector algebra it is possible isolate the field vector of the cycled element. It was conceived for cases when it is not possible to sample the signal of a single element, and when phase information about the sampled signals is not available. A discussion about the associated error of the technique is presented in [58], a faster version based on Fourier transforms is introduced in [59], and an improved version that considers the excitation error introduced by a digital phased shifter is shown in [60]. Other cases similar to the REV can be found in [39, 61, 62, 63].

An alternative approach to REV that also uses a phase encoding algorithm is proposed by Silverstein [64, 65]. He devised a remote calibration technique that toggles the phase configuration of the antenna elements following an orthogonal code. The technique is compatible with both analog and digital architectures. In addition, several variations from this approach have been proposed [66, 67, 68, 69, 70, 71].

Finally, Table 2.4 summarizes the references cited in this review. The table

Table 2.4: Summary of the state-of-the-art of calibration techniques, categorized in (Ini)tial, (I)n-(S)itu, (Ext)ernal, (B)uilt-(I)n, NF, FF, (Dir)ect sample, (Enc)oded, MC, and, (Dig)ital.

Ref.	Note	Ini	I-S	Ext	B-I	NF	FF	Dir	Enc	MC	Dig
[28]	PP	x		x		x		x			
[35]	PP	x		x		x		x			
[33]	PP/Embedded	x	x	x	x	x		x		x	
[36]	PP	x		x		x		x			
[34]	PAA measurements	x		x		x	x	x			
[27]	TR modules direct	x				x		x			
[38]	TR modules direct	x				x		x			
[37]	TR module characterization	x				x		x			
[39]	REV	x	x	x			x		x		
[41]	Improved REV	x	x	x			x		x		
[40]	Adaptive nulling	x	x	x			x		x		
[42]	Cylindrical array/Polarimetric	x		x			x	x			
[47]	On-board probe		x		x	x			x		
[45]	Closed loop feed network		x		x			x			x
[46]	Signal injector		x		x			x			
[49]	On-board probe/Deformation		x		x	x		x			
[48]	On-board probe/Deformation		x		x	x		x			
[50]	MC-based	x	x		x					x	
[52]	MC-based	x	x		x					x	
[51]	MC-based	x	x		x					x	
[32]	Review of Cal/MC/PP	x	x	x	x	x		x		x	x
[53]	MC-based high accuracy	x	x		x					x	x
[54]	Embedded - Before/After		x		x					x	
[23]	PP/ MC-based Before/After	x	x	x	x	x				x	
[55]	Before/After		x		x					x	x
[56]	MC-based for Digital	x	x		x					x	x
[57]	REV/Power only	x	x	x	x		x		x		
[58]	REV/Power only		x		x	x			x		
[59]	REV/Power only		x		x	x			x		
[60]	REV/Power only		x		x	x			x		
[61]	REV and NF	x	x	x	x	x			x		
[62]	REV/Power only		x		x	x			x		
[44]	Review of hardware	x		x		x	x	x			
[64]	Orthogonal coding		x	x			x		x		x
[65]	Orthogonal coding		x	x			x		x		x
[67]	Validation of orthogonal coding		x	x			x		x		x
[69]	Phase coding		x	x		x	x		x		x

is meant to be used as a guide that points to a technique compatible with the categories presented by the review.

2.4.5 Pseudo Calibration

Other approaches worthy of mention have attempted to improve the performance of the array without necessarily calculating excitation errors. Because these cannot be catalogued as true calibration techniques, they may be described as pseudo calibration.

One of the first phased array diagnostic techniques was documented by Ransom and Mittra in 1970 [72], who proposed a theory of scanning an array using a NF scanner, and then, by taking advantage of Fourier transform properties, computing the fields distribution on its aperture. By visual inspection of the fields distribution, one could identify if an element is defective and not working properly. Later, this technique was formulated and experimentally validated by [73]. This primitive procedure is limited to only detecting defective components, and it does not provide information about the excitation of each element. Hence, it cannot be considered a true calibration technique.

Another approach to correct for array imperfections arises in the case of small arrays. Since this type of array is not large enough, mutual coupling affects each element differently, precluding proper beamforming. To compensate for this problem, the literature [74, 75] rrecommends assuming that the pattern of a small array is the weighted sum of the ideal element pattern plus added perturbation due to MC effects. Then, it derives a compensation complex weight matrix to correct this effect.

2.5 Chapter Summary

This chapter focused on the fundamentals of phased array antennas and their calibration.It started by defining phased array antennas, indicating their main components, and presenting the analytical formulation to obtain result-

ing patterns. Next, it described the motivation behind the study of phased array calibration techniques by illustrating the adverse effects of the excitation misalignment problem. Excitation errors can be systematic or random, and the adverse effect of systematic errors are worst than of random errors. Calibration methods were described to quantify the errors and correct them such that, after calibration, only random errors must remain. Moreover, a quantitative description of how random errors affect the realized pattern of an array was provided.

With the goal of giving the reader an overview of the current challenges in phased array calibration, an extensive review of the state-of-the-art was presented. The review revealed several different approaches, conceived for a wide variety of system and instrumentation setups. As a consequence, it was proposed to categorize each approach under different criteria. As a result, the review was divided into initial vs. in-situ types, as well as external versus built-in feedback instruments, NF versus FF measurements, and specialized signal injection loops versus mutual coupling samples. All of these categories were briefly described and exemplified through proper citation. Finally, to offer the reader a tool to easily identify a technique according to the previous criteria, a summary of the state-of-the-art was presented in Table 2.4.

3 Instrumentation for Phased Array Antenna Characterization and Calibration

3.1 Introduction

This chapter discusses the instrumentation necessary to perform phased array measurements and calibration. It starts by reviewing the current-state-of-the-art of antenna measurement ranges used to test phased arrays. The reviewed scanners and instrumentation include: the commercial 150 cm $\times$ 150 cm NF planar scanner located at the Radar Innovations Laboratory (RIL), which was used to perform phased array calibration experiments (Chapter 4); the custom-made calibration 60 cm $\times$ 60 cm scanner designed by NCAR-EOL to characterize small phased array prototypes, which was used to perform the experiments in Chapter 5; and cases exemplifying the new trend of implementing articulated robotic manipulators for RF and antenna measurements.

In addition, a novel microwave instrumentation concept, the denominated RF Scanner, is introduced. The RF Scanner is a tool conceived specifically for phased array characterization and calibration. It has the capability to test phased arrays under different temperature conditions, inspect the surface of the antenna using image processing, and perform RF measurements of its elements.

3.2 State-of-the-Art

An overview of antenna measurements for phased array antennas can be found in the literature [44, 34]. As with any other antenna, a phased array antenna may be measured with the help of a NF or FF test range, but often a NF planar range is preferred since its probe positioning capability allows for

testing each antenna element at boresight, which is much needed to determine the health of each element [35]. In addition, array antennas often have planar apertures to synthesize narrow pencil-shaped beams, the type of configuration for which planar scanners are designed to test [76].

An example of a commercial NF range, compatible with phased array measurements, is shown in Figure 3.1. The case illustrated is an 8×8 phased array antenna prepared to be tested by the NF planar scanner of the RIL. This setup is the same used in Chapter 4 to fully calibrate and measure antenna patterns of the 8×8 dual polarized phased array prototype.

The main component of the antenna range is the Cartesian robotic manipulator. This particular manipulator allows four degrees of freedom: three of them allow linear movements in the $x-$, $y-$ and $z-$axes, and the fourth one is a rotational joint connected to the probe mount that allows polarization control. In this manner, the three linear actuators allow positioning the probe anywhere within a 2D rectangular plane, and the rotational joint allows the probe to orient itself according to the polarization of the antenna under test (AUT). Thus, the rotational joint can control horizontal (H) or vertical (V) testing. The maximum allowed scan window, in $x-$ and $y-$ is 150 cm × 150 cm.

The antenna probe is often a standard open-ended waveguide (OEWG) antenna of dimensions compatible with the frequency test. The manipulator and AUT sit inside an anechoic chamber that both isolates the inside from external RF signals, and prevents unwanted reflections from the surroundings to interfere with the measurements by means of microwave absorbers.

This setup is suitable for receiving measurements of the AUT. For transmit mode extra features are required [77]]. For instance, most phased array trans-

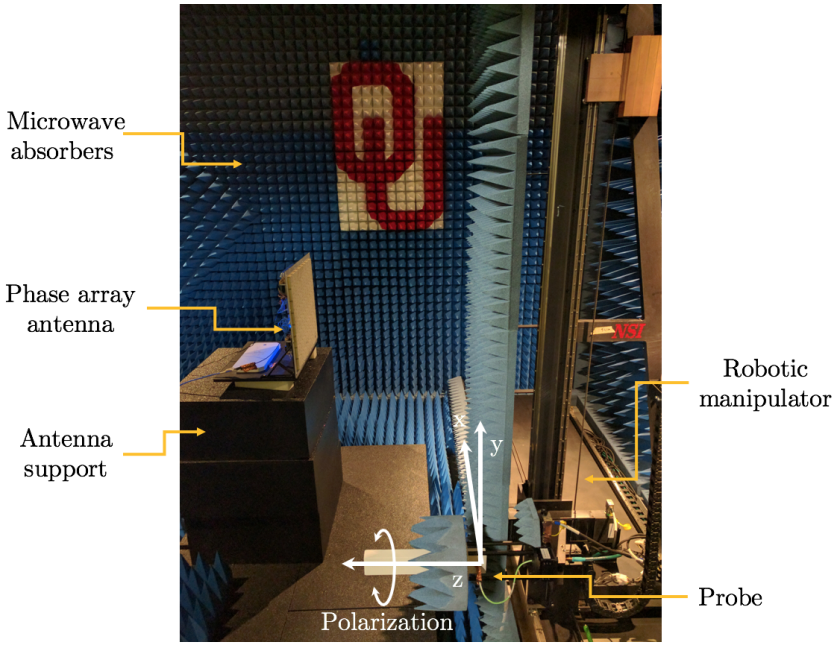

Figure 3.1: Planar NF test range inside an anechoic chamber, located at the Radar Innovations Laboratory, The University of Oklahoma.

mit microwave paths include high power amplifiers that allow pulsed operation exclusively. Thus, the instrumentation, e.g., the vector network analyzer, must be compatible with pulsed measurements. Moreover, if the AUT is large and has high power capabilities, an especially high-power-graded absorber must be used to cover the chamber due to fire risk.

A disadvantage of a commercial NF scanner is its high price. Further, commercial NF chambers are designed specifically for measuring antenna patterns, not for phased array calibration. However, if the required functionality is only to perform a park and probe test, then it is possible to build a custom-made calibration scanner that is both simpler and more affordable than a commercial NF scanner. Proof of this is the Cartesian scanner developed by NCAR-EOL, shown in Figure 3.2.

The scanner consists of a Cartesian manipulator with the same degrees of freedom as the commercial scanner shown in Figure 3.1. The scanner is

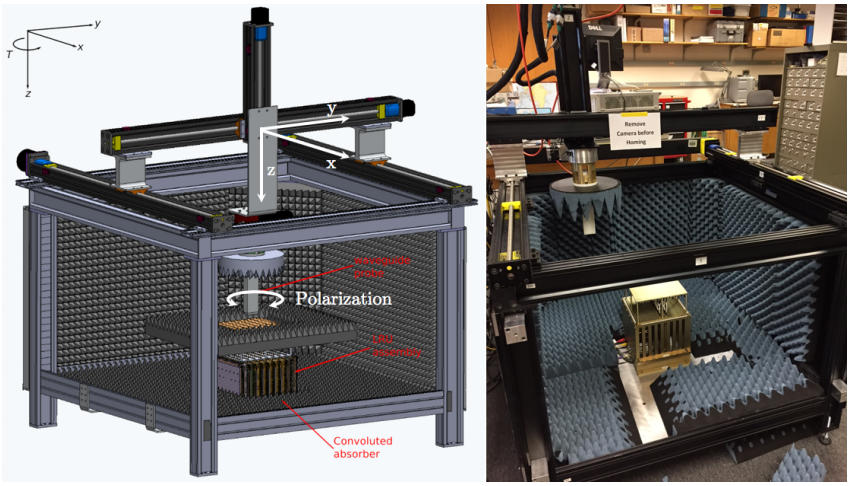

Figure 3.2: Cartesian scanner devised for calibration of the LRU. Left: Rendered design of the scanner, showing its components. Right: Picture of the scanner, located at the National Center for Atmospheric Research-Earth Observing Laboratory. Source: courtesy of Pei-sang Tsai.

embedded within a metallic box lined with microwave absorbers, and within which the AUT is mounted. The main purpose of the scanner is to perform park and probe measurements to the Linear Replaceable Unit (LRU) being developed by NCAR-EOL. For this, a program written in LabView is used to coordinate the movement of the actuators, configure the TR modules of the AUT, and the control the RF instrumentation. The maximum scanning window for this setup is only 60 cm $\times$ 60 cm, approximately a third of the area covered by the commercial option.

Indeed, the reduced size of the Cartesian scanner makes it unsuitable to perform full NF scans to obtain antenna patterns. However, it is an outstanding tool to explore calibration issues on phased array prototypes. This tool was instrumental in providing a ground truth for evaluating the mutual coupling-based calibration techniques detailed in Section 5.

Both of the examples introduced above are suitable for S-, C- and X-bands. However, for antennas on the mmWave band, the instrumentation is

not compatible. Frequency extender modules are commonly required to reach frequency bands above 25 GHz. Moreover, at such frequencies the size factor of the transmission lines is reduced, and components like RF cables, connectors and antenna probes also reduce in size, and become incompatible with lower frequency applications.

The reduced size associated with mmWave wavelengths leading to a reduced antenna scanner size actually offers opportunities for new approaches to antenna measurement. The shorter distances involved in mmWave allow the employment of articulated robotics. These are more versatile manipulators and work within limited workspace. For instance, the National Institute of Standards and Technology (NIST) took advantage of the size reduction and developed the configurable robotic millimeter-wave antenna (CROMMA) facility [78, 79] shown in Figure 3.3.

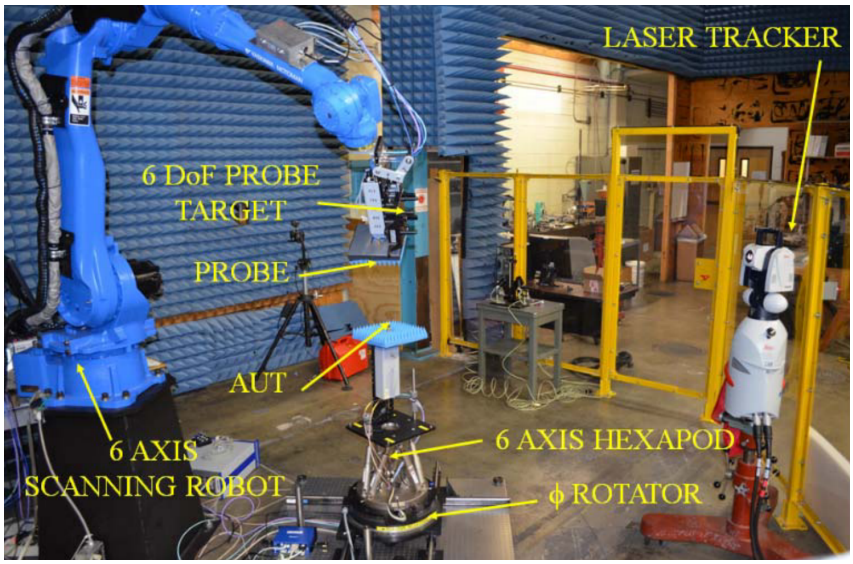

Figure 3.3: The CROMMA facility. It employs an articulated robotic manipulator in conjunction with an extremely accurate AUT positioner to perform antenna measurements at mmWave. Source: [80].

CROMMA consists of a mmWave antenna scanner based on an articulated

robotic manipulator. The robotic manipulator is in charge of positioning the antenna probe. Another robotic manipulator, a remarkably accurate hexapod, is used to setup the AUT. Finally, a laser tracker is implemented to improve the positioning accuracy of both manipulators. The positioning accuracy of the robotic manipulator is 70 μm. For NF scans, the minimum required accuracy [81], σ_{pos}, is

$$\sigma_{pos} = \frac{\lambda}{50}. \tag{3.1}$$

The maximum frequency allowed under this condition is $\approx$ 85 GHz. However, by adding the laser tracker as position feedback, the positioning can be improved to an impressive $\sigma_{pos} < 25$ μm, enabling devices at frequencies of up to 300 GHz to be tested.

An articulated configuration for the robotic manipulator was chosen over a Cartesian one because it allows movement with six degrees of freedom. Hence, by having the robotic manipulator position the antenna probe, it is possible to perform planar, cylindrical, spherical, and indeed any arbitrary scan path. This configuration is more flexible and convenient than traditional test configurations that require a specific positioner for each scan configuration. Similar work, with more modest accuracy, has been proposed by [82, 83].

The ARRC has also explored the use of robotic manipulators, and has implemented a compact robotic arm to test radome attenuation for weather radar applications [84, 85]. The instrument consists of a reflectometer attached to a robotic arm; the setup is located inside the protective radome of a radar, as shown in Figure 3.4. The reflectometer captures the energy reflected back by the radome and its surroundings. By applying time-domain gating, the reflections from the radome are discriminated and isolated from

clutter. A robotic arm is employed to carry the reflectometer according to a semi-spherical scan. Although this is not a direct antenna measurement application, it is an excellent example of the use of articulated robotics for automation of RF measurements.

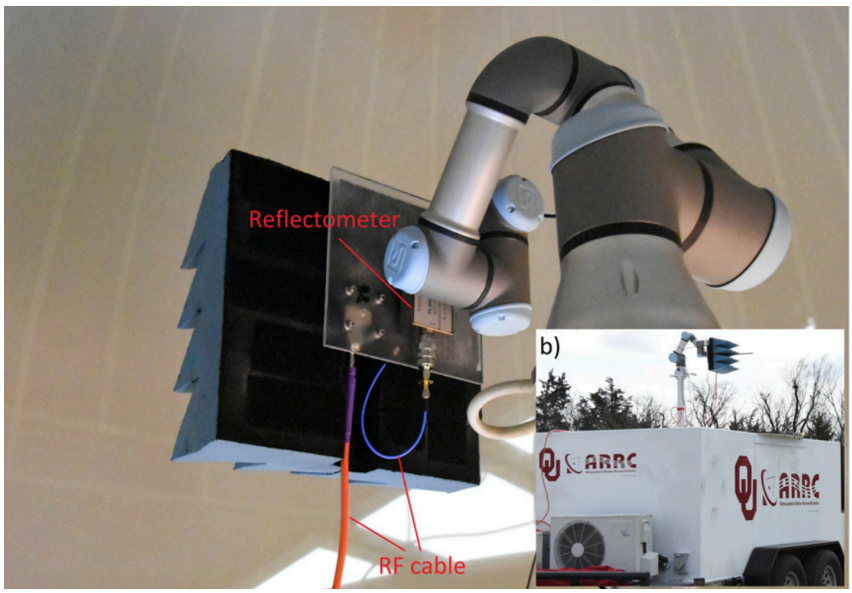

Figure 3.4: Weather radar radome attenuation scanner, developed by the ARRC. Source: [85].

3.3 6-axis Robotic RF Scanner

Literature regarding instrumentation specific to phased array calibration is lacking. Most existing techniques suggest using a common NF planar scanner to perform the park and probe technique [28, 35], or using built-in equipment, as reviewed in the previous chapter. However, when information about the performance of an array under different temperature conditions is necessary, a standard NF scanner cannot offer a complete characterization of the phased array aperture. Moreover, a NF planar scanner is limited to calibration of only planar phased arrays, whereas, if more degrees of freedom were available, as

in the case of the CROMMA [79], conformal arrays could also be calibrated.

In this context, the ARRC have been developing an automated robotic solution for phased array calibration [86, 87]. An articulated robotic manipulator is used to carry an arrangement of sensors to efficiently characterize a phased array-based system using the park and probe technique. This particular system was designed to be flexible and support different types of antenna shapes, including planar and conformal. Moreover, the proposed tool also allows testing within a range of 0-50 °C, and a closed loop probe-element alignment mechanism.

3.3.1 System Description

A block diagram depicting the components of the scanner and their arrangement is shown in Figure 3.5. The core of the scanner is an articulated robotic manipulator in charge of positioning tasks. A sensor suite is attached at the end of the manipulator. The sensor suite consists of a mechanical structure upon which most of the sensors are mounted. Its main function is to support the sensors and their wiring, and to provide them with the appropriate conditions for operation. The AUT is located immediately in front of the robotic manipulator to enable the manipulator to freely move the sensor suite over the AUT. Furthermore, a microwave amplifier or attenuators might be added to condition the signal to suitable power levels. All of these components sit inside an environmental chamber that controls the operation temperature at which the tests are performed.

The sensors selected to perform data acquisition are a High Definition (HD) camera, an antenna probe, and a thermal imaging camera, all of them mounted on the sensor suite. The HD camera, which is capable of digitally processing

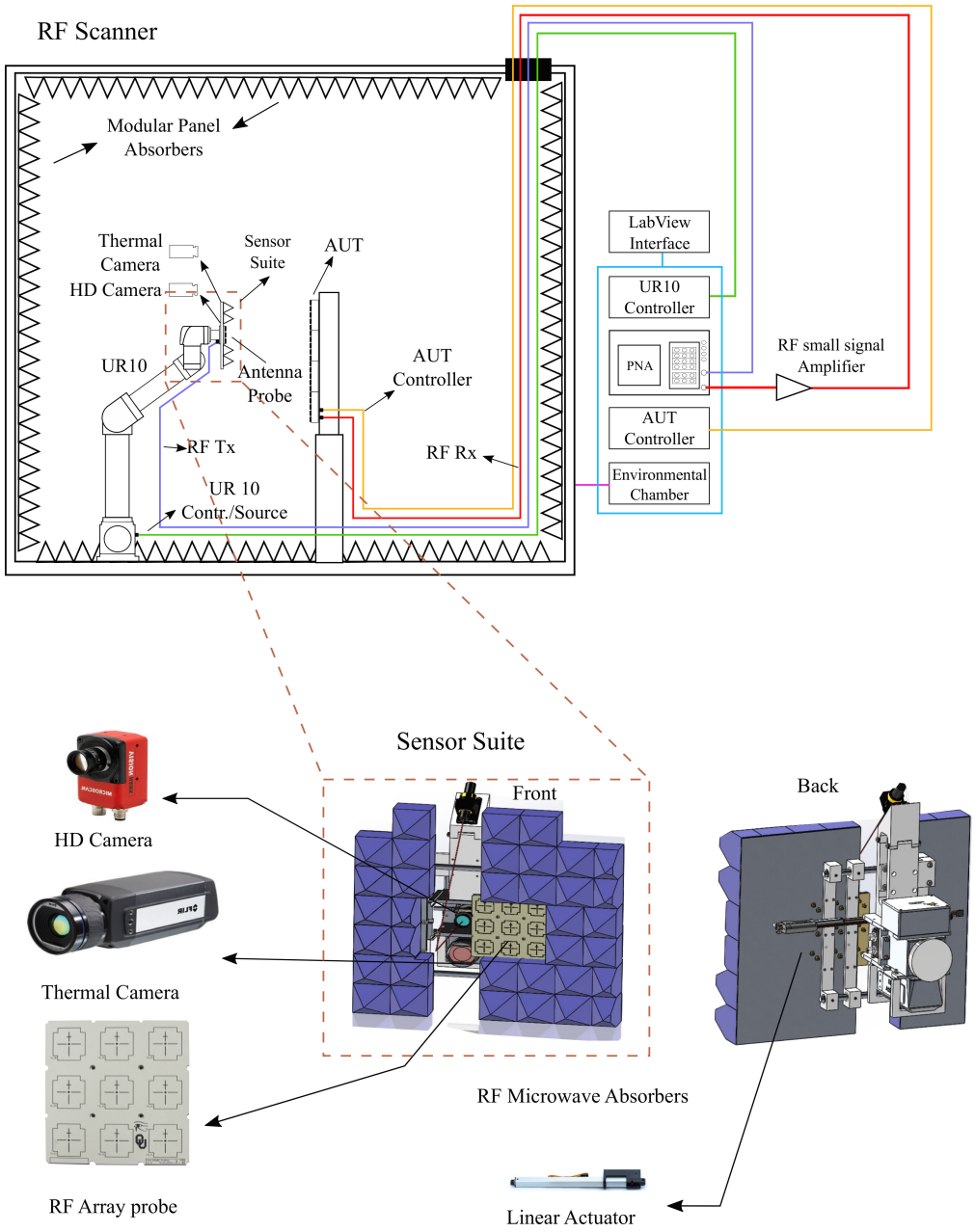

Figure 3.5: Block diagram of the RF scanner illustrating its main components. Source: [86]

images, is used to locate the exact center of the antenna elements. The antenna probe samples the electric fields in front of the antenna elements. Finally, the thermal camera snaps thermal pictures of the temperature distribution

on the surface of the antenna array. This sensor and actuator arrangement allows the automated tool to perform repeatable measurements of the radiation characteristics of all antenna elements over a range of 0 to 50 °C operation temperatures.

A picture of the RF scanner is shown in Figure 3.6. The robotic arm selected is the UR10 model from Universal Robots [88]. The arm is rated as a collaborative type, i.e., it is safe for a person to be around while in operation. This manipulator is capable of 100 μm position accuracy, which, according to (3.1), allows NF scans of up to 60 GHz. However, the current VNA and wiring hardware are rated to a maximum frequency of 18 GHz.

In addition, the robotic arm has a reach ratio of 1.3 m, but once the sensors are mounted on it, the scanner can only cover a plane of 80 cm $\times$ 80 cm. As a consequence, although the scanner is capable of performing NF to FF rasters, the limited planar scan window size is not convenient for devices of low frequency. It may be possible to extend the NF raster area by implementing non-canonical scans, e.g., scans that are neither spherical, cylindrical nor planar, as proposed by [89], but this is beyond the scope of this research, and is suggested for future research.

A detailed description on how the system operates as well as an explanation of the interaction among the sensors it implements is given next.

3.3.2 Proposed Operation

The scanner operation procedure is summarized using the flow diagram in Figure 3.7. As shown in the figure diagram, the procedure starts by setting up the test temperature, which is controlled by the environmental chamber. The temperature value is defined by the operation conditions of the phased

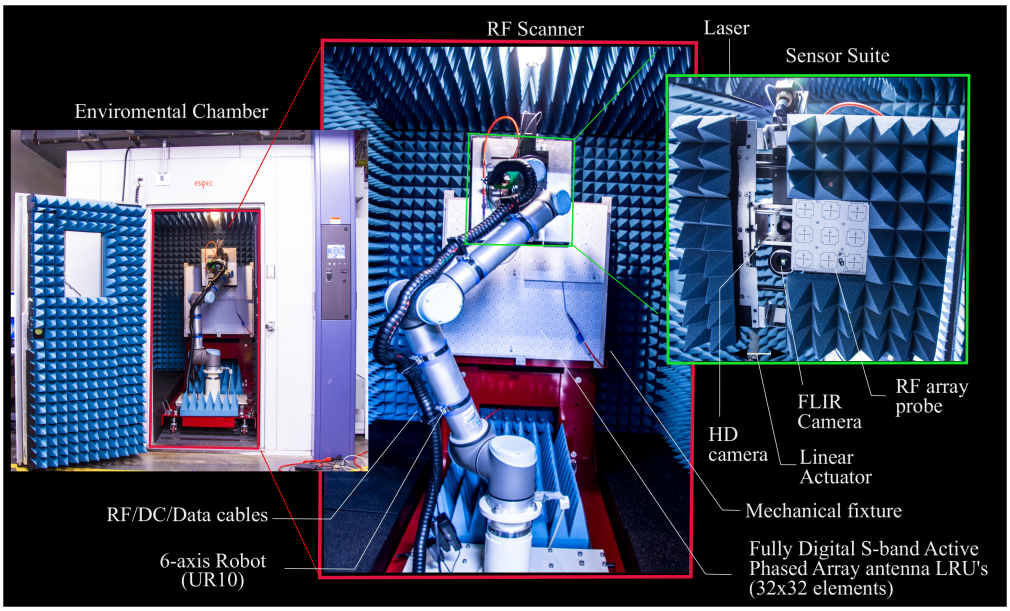

Figure 3.6: Picture of the RF scanner sitting inside the RIL at The University of Oklahoma. Source: [86]

array-based system. The interior of the chamber, containing the robot, AUT, instrumentation, and wiring, is kept under constant temperature by the automated action of the chamber. The scanner halts for an interval of at least 3 hours to allow the components to reach thermal equilibrium with their environment, ensuring in this manner that all components be at the test temperature.

Once the temperature is uniform inside the chamber, the scanner proceeds to position the probe at boresight of the antenna element to be sampled. In principle, if the robotic manipulator reference system is precisely aligned with the reference system of the AUT, then positioning the robot at the front of the antenna element should be easily achieved by a command to move the robot to a predefined set of coordinates. However, manufacturing errors and mechanical obstacles may preclude the alignment of the AUT and manipulator, which will cause the probe to be off-center of the antenna element.

Moreover, temperature variations may change the relative position of the

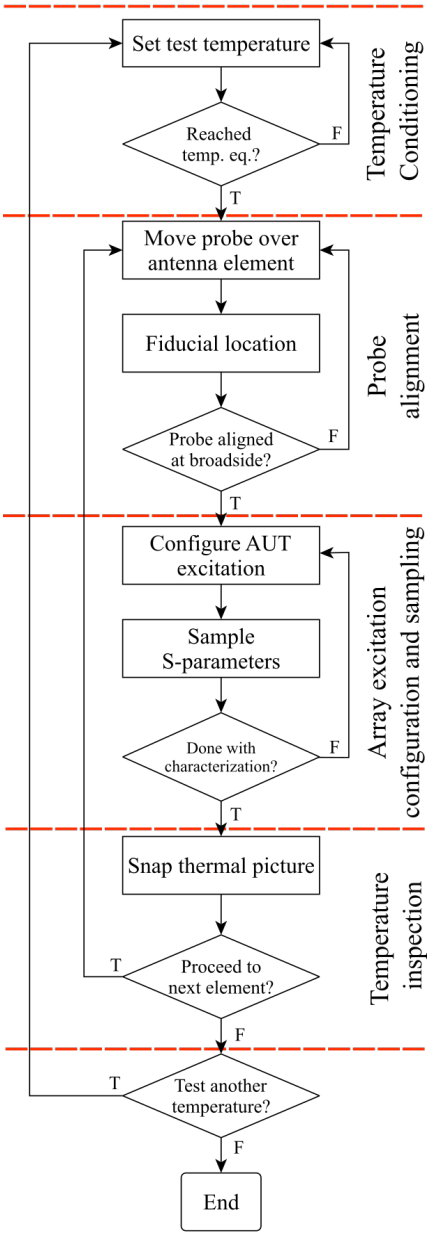

Figure 3.7: Flow diagram explaining the scanner operation during phased array system characterization. The complete procedure collects sufficient data to represent the radiation characteristics of the antenna array, that will be further processed to calibrate its antenna patterns.

AUT with respect to the manipulator, introducing yet more offsets between the probe position and the boresight of the antenna element. As a result, the

HD camera is used as a feedback sensor to ensure the correct positioning of the probe.

To accomplish this task, the HD camera inspects the surface of the antenna and uses real-time machine vision algorithms to recognize a fiducial image indicating the center of the element, as shown here in Figure 3.8.(b). After recognition the scanner will command the robot to correct its position, and use the camera another time to check the current state. The process iterates until a user-predefined error tolerance has been attained, which indicates that the probe is finally aligned.

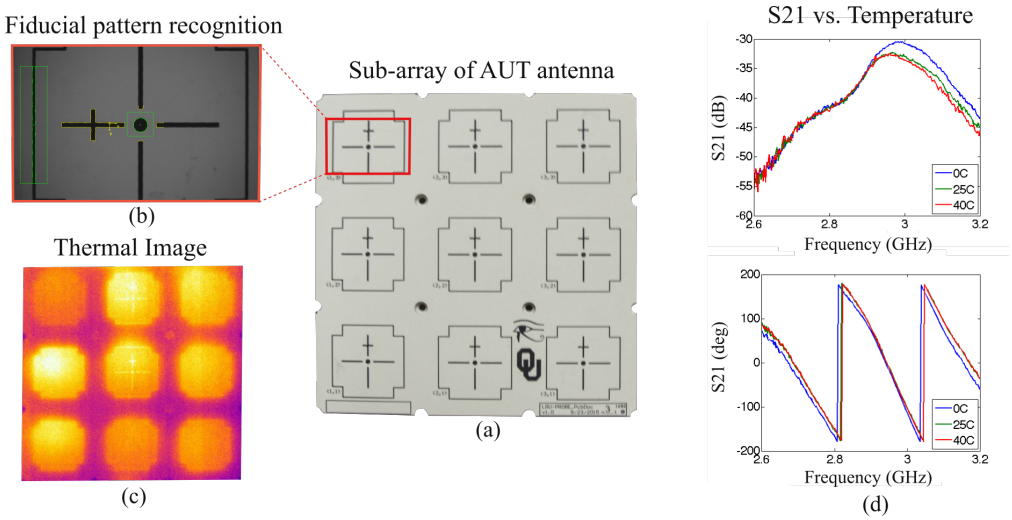

Figure 3.8: Proposed capabilities of the RF Scanner. (a) 3×3 phased array employed as antenna probe. (b) Recognize fiducial patterns marking the location of an antenna element. (c) Thermal image of the surface of an AUT. (d) Examples of the phase and amplitude of the S21 parameters between the AUT and antenna probe under different temperatures. Source: [86]

The following step is the RF characterization stage. The objective is to sample the fields radiated by a specific antenna element, using the probe and the VNA. Additionally, depending on the frequency range of operation and internal circuitry of the AUT, signal conditioning components such as amplifiers and attenuators might be necessary. First, the array controller should config-

ure the excitation of the antenna element according to a predefined sequence of excitation states to be tested. Second, the scanner will order the VNA to perform an S-parameters measurement. Figure 3.8.(d) shows an example of these measurements. The results will be stored on the main computer, and later processed for array calibration. These steps will be repeated according to the number of excitation states defined in the test sequence.

After concluding the radiation sampling the thermal camera is used to snap a thermal image of the surface area of the array. The image contains valuable information about the heat distribution along the antenna array, and can also be used as a feedback of the temperature equilibrium dwelling period. Figure 3.8.(c) shows the thermal image of the surface of a 3×3 phased array antenna.

Afterwards, the procedure will be repeated for the remaining antenna elements to be sampled. This includes applying the positioning feedback loop for the position of the next element, and sampling its RF characteristics in the same way the scanner did for the previous element. At the end of this stage the complete array has been scanned and the collected data is sufficient for calibration purposes. Nevertheless, the data is only representative of the array performance under the temperature at which it was tested. The above detailed procedure will be fully replicated, but for another operative test temperature, until the full characterization of the array is achieved.

3.4 Chapter Summary

This chapter reviewed current technology used for antenna measurements. It revealed that the most common antenna range for calibration is the NF planar scanner, which is suitable for performing park and probe tests. Moreover, it also presented the new trend of involving articulated robotic manipulators,

with several degrees of freedom, in antenna measurements in general. The multiple degrees of freedom on this type of manipulator allows a single setup to implement various scan strategies.

A novel tool for phased array calibration has also been presented. The RF scanner is capable of testing the performance of phased arrays under different temperature conditions, from 0-50 °C, since all the equipment is enclosed in an environmental chamber. It is also capable, of performing park and probe tests on planar or conformal phased arrays, at frequencies up to 18 GHz. It is equipped with an HD camera for identifying the center of each antenna element, and can snap thermal pictures of the surface of the antenna aperture.

4 Near Field Calibration for Phased Array Antennas

4.1 Introduction

During the development of a phased array radar, the designers must ensure that the scan capability of the antenna is acceptable. It is common then to manufacture antenna prototypes, and test them using antenna test ranges [90, 91]. The measurement of the antenna patterns of a phased array is an extensive endeavor since the array is able to produce an infinite number of beams, depending on the combination of phase shift and amplitude excitations applied to its antenna elements. Furthermore, in some cases the prototype is a linear replaceable unit (LRU) that includes the front-end of the radar system, which is composed of the antenna, antenna feed, TR modules, and beam former. The large number of hardware components on a LRU makes it prone to phase and amplitude excitation errors, i.e., the complex weight excitations on each antenna element are affected by errors.A characterization of the phased array system, also known as initial calibration, must be performed to compensate for these introduced errors to quantify these "misalignments". In this context, the goal of this chapter is to propose, test, and validate a complete initial calibration procedure for performance assessment of phased array radar prototypes.

The most attractive capability of phased array antennas in radar applications is to electronically steer their beam, which allows fast scans and render mechanical pedestals unnecessary. Thus, the main objective of the performance assessment of phased array antennas is to evaluate the beams steered at each target observation position. As a result, the most basic assessment procedure will require scanning the beam-steered patterns of the antenna un-

der test (AUT). This can be accomplished by direct or indirect measurements. The direct measurement of beam-steered patterns, as its names indicates, consists of directly scanning the patterns when the array is fully active. On the other hand, indirect measurements can be obtained by synthesis of the embedded element patterns, i.e., the pattern of an active element while the other elements are match terminated [92]. The embedded element patterns act as a base from which any other beam pattern can be synthesized. An example of this can be found in [67].

The indirect approach has the advantage that any other beam could be synthesized using a finite set of base patterns, and it may be the only alternative when the combined power level of the full active array is too high to be managed by the available instrumentation. This, was described in [93] which proposed measuring small subarray clusters instead of the full array to reduce the total radiated power. Of course, the decision to use a direct or indirect approach depends on the number of active elements in the array, making the indirect approach more attractive when the number of elements is not high. In any case, a complete procedure for performance assessment should include both approaches.

Moreover, when the AUT includes TR modules, the misalignment errors due to hardware imperfections must be quantified so they can be compensated for using the capabilities of the available TR modules. The conventional method for sampling misalignment errors is to use an antenna probe to test each antenna element separately. This method, often called "park and probe" [94], was first introduced by [28], and consists of using a robotic scanner to automatically position the probe at boresight of each element, and then sampling its excitation, while the rest of the elements are match terminated. Thus, the

process of defining a complete characterization procedure requires addressing the misalignment issue. For this reason, an initial calibration of the phased array system should not only be dedicated to capturing beam-steered patterns, but should also include a characterization technique, such as park and probe, that quantifies the misalignment errors.

To this point an initial calibration must include: characterizing the array hardware, scanning the embedded elements of each active element, and finally scanning the realized beam-steered patterns. Note that, by collecting the excitation data of each element, as well as having the embedded element patterns, the performance of the array in essence has been completely defined. Any pattern that can be produced by the array is only a weighted sum of embedded element patterns [95], and hence, if both the excitations and embedded patterns are known, then any beam can be accurately predicted. This approach is different from previous ones because in the past prediction was only based either on the excitation data, or on the embedded elements.

As a result, it is proposed that a complete initial calibration technique must include the following: characterizing the excitation hardware and using the result to correct for misalignment; scanning the embedded element patterns of the active elements; using the collected data to predict the beam patterns of interest; and finally, directly scanning these defined patterns. In this manner, the user will have complete knowledge of the steering capabilities of the system.

In order to support the proposed procedure the LRU test-bed developped by NCAR-EOL has been experimentally tested according to the defined guidelines of the procedure. The case study demonstrates the benefits of following the procedure, and it also serves as an example of how to implement it.

The chapter is arranged as follows. The proposed procedure is introduced

in Section 4.2. The instrumentation and description of the LRU used for the case study are presented in 4.3.1. The procedure and results of the experiments performed are discussed in sections 4.3.2 and 4.4, respectively. Lastly, the validation of the pattern prediction technique is demonstrated in 4.4.4. For more information about the procedure, the reader can refer to [96], which is a previous publication of the author regarding this theory.

4.2 Theory

The main objective of the proposed initial calibration is to define what data should be collected, and how it has to be processed to produce results that allow the phased array radar designer to evaluate the prototype under test. This technique is intended to be seen as a guide, describing the complete set of tests required to perform a thorough characterization of a phased array-based system.

Each test is described as a stage of the initial calibration. The tests are detailed in the following subsections.

4.2.1 Excitation Characterization

The excitation of each active element, also known as its complex weight, corresponds to its phase and amplitude configuration. In a phased array, the phase and amplitude of its elements are actuated by means of a phase shifter and attenuator, respectively. These components often present non-ideal behavior that, for instance, forces the phase shifter to change not only the phase of a signal, but also its amplitude. The same can be said of an attenuator, which adds an unaccounted phase shift to a signal which was supposed to be modified in amplitude only. These effects cause difficult proper

beam synthesis, since the resultant pattern is affected by such excitation errors. Hence, the errors due to the excitation components must be measured.

Moreover, transmission lines, the beamformer, and the antenna feed may have fabrication errors as well, causing the electrical paths of the antenna elements to be different. The result is that different antenna elements have different excitation gains. These errors between antenna elements should also be quantified.

For this reason, the first step of the initial calibration is to implement a characterization technique that can test each antenna element to measure the differences among them, and that can also sample the different phase shift and attenuation combinations to capture the non-ideal behavior of the phase shifter and attenuators. An example of a valid characterization technique is the widely-used "park and probe" technique, described next.

4.2.2 Park and Probe Technique

The theory of the park and probe technique described in this work is based on the excellent description offered by Şeker [32]. Figure 4.1 presents a diagram of the traditional park and probe calibration technique of a N-elements array antenna. The figure shows an antenna probe being positioned in front of the nth antenna element, while the other antenna elements are terminated to their corresponding transmission line impedance. It also displays the TR modules attached to the antenna elements, which are in charge of conditioning the transmit and receive signals going through the antennas. The figure completely describes the path of a signal being transmitted or received by either the probe or the antenna element.

Any measurement performed between the nth antenna element and the

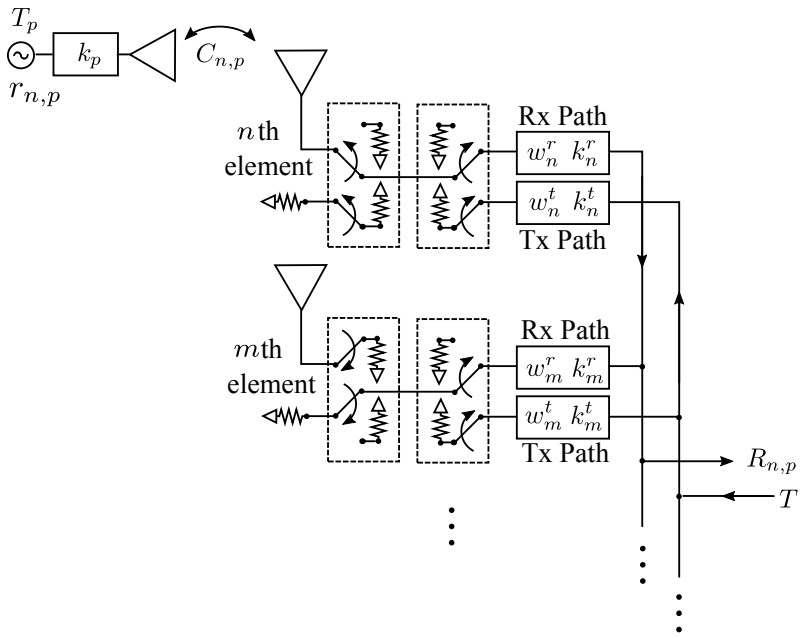

Figure 4.1: Coupling diagram for calibration measurements in arrays with analog beamformer networks, using an external antenna probe. Test the nth element in receive.

probe, i.e., transmit with the probe and receive with the antenna element, and vice-versa, can be viewed as the signals received by the probe, $r_{n,p}$, and the signal received by the antenna element, $R_{n,p}$. From Figure 4.1 one can formulate an equation that represents the signal received by the antenna element as

$$R_{n,p}(w_n^r) = k_n^r w_n^r C_{n,p} k_p T_p, \tag{4.1}$$

where $R_{n,p}$ is the signal transmitted from the probe and received by the nth antenna element, k_n^r is the unknown error due to effects of the receive module, w_n^r is the complex excitation weight in receive mode set by the user for the nth element, $C_{n,p}$ is the coupling between the probe and the nth antenna element, k_p represents losses due to the probe, and finally, T_p is the signal transmitted from the probe to the nth element. The term k_n lumps together the effect of the active component as well as the effect of the transmission lines, antenna,

and analog beamformer.

Likewise, the signal received by the probe is expressed as,

$$r_{p,n}(w_n^t) = k_p C_{n,p} w_n^t k_n^t T. \tag{4.2}$$

where $r_{p,n}$ is the signal transmitted from the nth antenna element and received by the probe, k_n^t is the unknown error due to effects of the transmit path, w_n^t is the complex excitation weight in transmit mode set by the user for the nth element, and finally, T_n is the signal transmitted by the nth element to the probe.

Table 4.1 lists all variables involved in (4.1) and (4.2), and specifies whether they are:

Known either defined by the user or measured prior the application of the calibration technique.

Measured during the calibration procedure.

Unknown due to hardware and measurement instruments errors.

The procedure requires to test all antenna elements of interest, often using a robotic manipulator to automatically and accurately position the probe at boresight of the tested antenna element. The NF sampling of all antenna elements must be performed at the same probe-to-antenna distances, usually 3λ to 5λ.

Since the antenna elements are identical and they are tested under similar conditions, then the coupling between probe and any antenna element is assumed to be identical, i.e.,

$$C_{n,p} = C_{m,p}. \tag{4.3}$$

Table 4.1: List of variables involved in the NF at boresight calibration technique. Adapted from [32]

.

Magnitude	**Symbol**	**State**
Signal from the probe received by the nth element	$R_{n,p}$	Measured
Signal from the nth antenna received by the probe	$r_{n,p}$	Measured
Signal transmitted from the probe to the nth antenna	T_p	Known
Signal transmitted from the nth antenna to the probe	T	Known
Amplitude/phase configuration in receive mode (complex weight)	w_m^r	Known
Amplitude/phase configuration in transmit mode (complex weight)	w_m^t	Known
Losses due to the probe antenna	k_p	Unknown
Coupling between the probe and the n-h antenna element	$C_{n,p}$	Unknown
Amplitude/phase errors of the nth element in receive mode, due to active components, transmission lines, antenna and analog beamformer	k_n^r	Unknown
Amplitude/phase errors of the nth element in transmit mode, due to active components, transmission lines, antenna and analog beamformer	k_n^t	Unknown

Next, comparing received and transmitted signals from any mth and nth element pair, and using (4.3), the resulting ratios are

$$\frac{R_{n,p}(w_n^r)}{R_{m,p}(w_m^r)} = \frac{k_n^r w_n^r C_{n,p} k_p T_p}{k_m^r w_m^r C_{m,p} k_p T_p} = \frac{w_n^r k_n^r}{w_m^r k_m^r}, \tag{4.4}$$

and

$$\frac{r_{p,n}(w_n^t)}{r_{p,m}(w_m^t)} = \frac{k_p C_{n,p} w_n^t k_n^t T}{k_p C_{m,p} w_m^t k_m^t T} = \frac{w_n^t k_n^t}{w_m^t k_m^t}. \tag{4.5}$$

Expressions (4.4) and (4.5) contain important information about the dif-

ferences between the radiation of any two antenna elements. They show that any discrepancy between the mth and nth elements will be determined by the unknown error terms k_m^r, k_n^r, k_m^t and k_n^t, and by the user defined excitation weights w_m^r, w_n^r, w_m^t and w_n^t. More importantly, these expressions demonstrate that the differences in amplitude and phase between sampled fields of different elements can be quantized using the measured values $R_{n,p}$, $R_{m,p}$, $r_{p,n}$ and $r_{p,m}$.

These expressions make it possible to define error ratios, K^r and K^t, among the elements in receive and transmit modes, respectively, in relation to an arbitrarily-defined reference element, ref. By substituting the reference element for the mth element in (4.4) and (4.5), the error ratios are defined as

$$K_n^r = \frac{R_{n,p}(w_n^r)}{R_{ref,p}(w_{ref}^r)}, \tag{4.6}$$

and

$$K_n^t = \frac{r_{p,n}(w_n^t)}{r_{p,ref}(w_{ref}^t)}. \tag{4.7}$$

Moreover, if the weight coefficients are chosen to yield the same phase and amplitude excitation for all elements, i.e, $w_n^r = w_m^r = w_{ref}^r = w^r$ and $w_n^t = w_m^t = w_{ref}^t = w^t$, (4.6) and (4.7) will be reduced to,

$$K_n^r = \frac{k_n^r}{k_{ref}^r}, \tag{4.8}$$

and,

$$K_n^t = \frac{k_n^t}{k_{ref}^t}, \tag{4.9}$$

respectively.

Thus, using magnitudes that can be measured with the help of the probe, the complex expressions (4.6) and (4.7) may be used to calculate the amplitude

and phase errors between any nth element and the reference.

4.2.3 Embedded Element Patterns Measurement

After characterizing the excitation of the phased array system, it is necessary to scan their embedded element patterns. This is accomplished by employing an antenna test range, e.g., a planar NF chamber, which is also compatible for park and probe tests, or a FF chamber. In addition to amplitude data, the scanned data must contain phase data so it can be post-processed in complex domain. The scanned nth element must be configured to a predefined $w_n^{embedded}(phs_{stg}, att_{stg})$ complex excitation which is a function of the combination of a selected phase shift stage, phs_{stg}, and of a selected attenuation stage, att_{stg}. The remaining elements are required to be terminated to their match impedance [92].

The embedded element patterns are critical to characterize any phased array. These measurements serve as a base for any array pattern to be calculated. Having these fundamental patterns allows the prediction of different steered and tapered antenna array patterns, which is helpful in deciding what patterns are more critical.

Two main reasons point to the importance of these patterns:

1. The array pattern is a weighted sum of the embedded element patterns [95]. Hence, the embedded element patterns are the base on which any array antenna pattern can be built.
2. The measured patterns are valid for all frequencies. By contrast, a beam-steered array pattern for a specific angle is only valid for a single frequency.

An embedded element pattern is an antenna pattern that reflects the im-

pact of the array environment on the element. For instance, a microstrip patch antenna pattern, while often predicted by analytical equations assuming an infinite ground plane, is nevertheless always etched on a finite ground plane, which adds unwanted edge diffractions [97, 98, 99, 100, 101]. Moreover, when an antenna element radiates in the presence of other antenna elements, the inherent mutual coupling forces the other antenna elements to be excited as well. As a result, mutual coupling also perturbs the pattern of an antenna element in an array environment. Thus, a measured antenna embedded element pattern can be seen as an antenna element pattern that considers the combined environmental effects of both edge diffractions and mutual coupling.

In an effort to mathematically describe the embedded antenna pattern measured on an antenna range, the work of Steyskal and Herd [74] may be used as a base to formulate the synthesized array pattern considering mutual coupling. For an N-element array with analog beam former, the FF array antenna pattern at coordinates θ and ϕ, $f_a(\theta, \phi)$, can be expressed in matrix form as

$$f_a(\theta,\phi) = \begin{bmatrix} 1 & 1 & \cdots & 1 \end{bmatrix} \begin{bmatrix} f_1 & 0 & \cdots & 0 \\ 0 & f_2 & \cdots & 0 \\ \vdots & \vdots & \ddots & \vdots \\ 0 & 0 & \cdots & f_N \end{bmatrix} \begin{bmatrix} C_{1,1} & C_{1,2} & \cdots & C_{1,N} \\ C_{2,1} & C_{2,2} & \cdots & C_{2,N} \\ \vdots & \vdots & \ddots & \vdots \\ C_{N,1} & C_{N,2} & \cdots & C_{N,N} \end{bmatrix} \begin{bmatrix} w_1 \\ w_2 \\ \vdots \\ w_N \end{bmatrix}, \tag{4.10}$$

or also, expressed as,

$$f_a(\theta,\phi) = \mathbf{TFCW}. \tag{4.11}$$

Where $\mathbf{T}$ is a $1\times N$ matrix consisting of ones,

$$\mathbf{T} = \begin{bmatrix} 1 & 1 & \cdots & 1 \end{bmatrix}. \tag{4.12}$$

The terms f_n represent the isolated pattern of the nth antenna element on its embedded location in the array, which includes the phase offset due to its location off phase center, and diffractions from the ground plane edges. All involved pattern terms f_n are a function of θ and ϕ, $f_n = f_n(\theta, \phi)$. $\mathbf{F}$ is a diagonal matrix conformed by the f_n terms:

$$\mathbf{F} = \begin{bmatrix} f_1 & 0 & \cdots & 0 \\ 0 & f_2 & \cdots & 0 \\ \vdots & \vdots & \ddots & \vdots \\ 0 & 0 & \cdots & f_N \end{bmatrix} = diag\left(\begin{bmatrix} f_1 \\ f_2 \\ \vdots \\ f_N \end{bmatrix} \right). \tag{4.13}$$

$C_{n,m}$ are complex coupling values between antenna elements n and m, and $\mathbf{C}$ is the coupling matrix:

$$\mathbf{C} = \begin{bmatrix} C_{1,1} & C_{1,2} & \cdots & C_{1,N} \\ C_{2,1} & C_{2,2} & \cdots & C_{2,N} \\ \vdots & \vdots & \ddots & \vdots \\ C_{N,1} & C_{N,2} & \cdots & C_{N,N} \end{bmatrix}. \tag{4.14}$$

Finally, $\mathbf{W}$ is a $N \times 1$ matrix containing the complex weights w_n,

$$\mathbf{W} = \begin{bmatrix} w_1 \\ w_2 \\ \vdots \\ w_N \end{bmatrix}. \tag{4.15}$$

Expression (4.11) is a matrix equation that indicates how the patterns f_n of an element located on the array are affected by the mutual coupling effect. Matrix $\mathbf{T}$ represents the effect of the analog beamformer, which sums the

patterns modified by the coupling terms $C_{n,m}$ to form the array beam f_a.

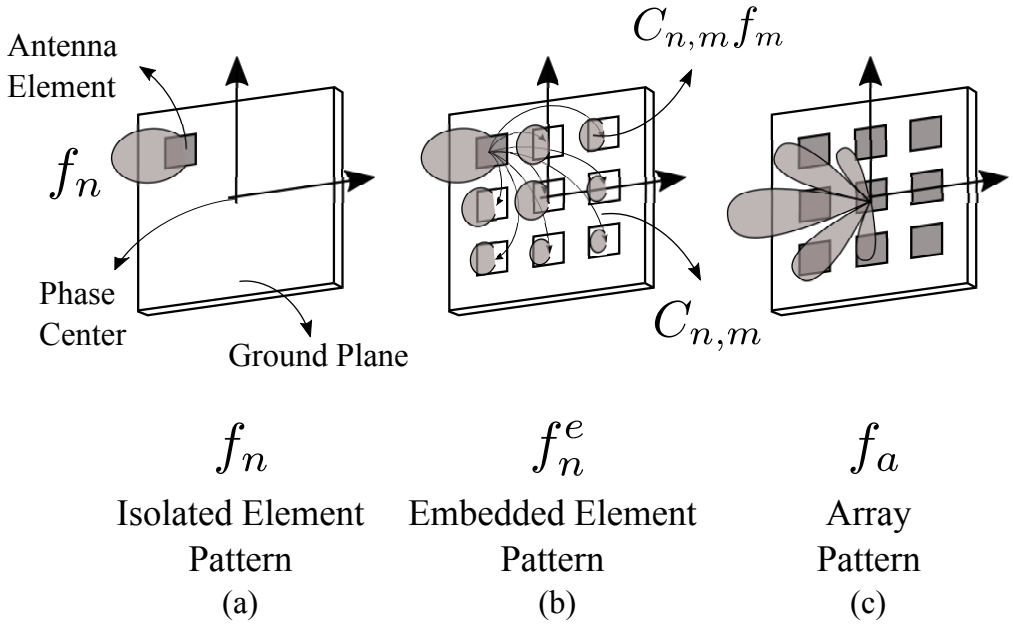

Figure 4.2: Illustration of the pattern synthesis on a phase array. (a) f_n: The top left element, located on the ground plane, is active. (b) f_n^e: The top left element is active; neighboring elements are excited by mutual coupling interactions. (c) f_a: all elements are excited

The embedded element pattern, f_n^e, is obtained when only the nth element is excited, i.e., $w_n = 1$ and $w_{m\neq n} = 0$. In this manner, the $\mathbf{W}$ matrix results in:

$$\mathbf{W_n} = \begin{bmatrix} 0 \\ \vdots \\ 1 \\ \vdots \\ 0 \end{bmatrix}. \tag{4.16}$$

Replacing $\mathbf{W}$ for $\mathbf{W}_n$ in (4.11), makes $f_a(\theta, \phi) = f_n^e$, which results in the

following summation:

$$\begin{aligned} f_n^e &= \mathbf{TFCW}_n \\ &= C_{1,n}f_1 + C_{2,n}f_2 + \cdots + C_{n,n}f_n + \cdots + C_{N,n}f_N \\ &= C_{n,n}f_n + \sum_{i=1, i\neq n}^{N} C_{i,n}f_i \end{aligned} \tag{4.17}$$

The resultant (4.17) expression states that the embedded element pattern of the nth element is not only the result of its own f_n pattern times the self coupling term $C_{n,n}$, but depends also on the added effect of mutual coupling exciting neighboring elements. See Figure 4.2 for graphical depiction of the differences between f_n, f_n^e and f_a.

4.2.4 Beam-Steered Patterns Measurement

The main objective of characterizing the antenna patterns of a phased array antenna is to analyze its performance at different beam-steered positions. This section directly analyzes the beamformed patterns at different beam pointing directions, using the same instrumentation as the embedded element scan. To define the excitations associated with each beam, a set of complex weights w_n^r are selected using [23]:

$$w_n^r(phs_{stg}, att_{stg}) = arg_{w_n^r} min \left| K_n^r(w_n^r) - w_n^{target} \right|, \tag{4.18}$$

where w_n^{target} is the target complex weight which is desired to be applied to the nth element.

For a uniformly spaced planar array the phase component of w_n^{target} is

derived from the progressive phase shift between elements [102],

$$\beta_x = -kd \sin\theta_0 \cos\phi_0, \tag{4.19}$$

$$\beta_y = -kd \sin\theta_0 \sin\phi_0, \tag{4.20}$$

where k is the wavenumber in free space, d is the element separation, and θ_0 and ϕ_0 are the coordinates of the main beam position. The amplitude of the w_n^{target} is defined according to the desired amplitude taper, e.g., uniform, Taylor or Chebyshev.

An example of beam-steered scanned patterns is presented by [103]. A detailed procedure was applied to study the effect of a wet radome on phased array antenna patterns. The beam of the array was steered at different angle positions, and the antenna patterns were collected using the NF planar scanner shown in Figure 3.1.

4.2.5 Array Pattern Prediction

The synthesis of an array antenna pattern f_a at the observation angles θ and ϕ is calculated [95] as

$$f_a(\theta, \phi) = \sum_{n=1}^{N} f_n^e(\theta, \phi) w_n, \tag{4.21}$$

where N is the number of active elements in the array, f_n^e is the embedded element pattern of the nth element, and w_n is the complex excitation applied to the nth element. The patterns f_n^e are the ones collected in Section 4.2.3. The complex weights w_n implemented in (4.21) are the set of w_n^r selected in Section 4.2.4 to create the calibrated beam-steered pattens, but normalized to the level at which the embedded element patterns were measured. In other

words,

$$w_n = \frac{w_n^r}{w_n^{embedded}}, \tag{4.22}$$

where $w_n^{embedded}$ is the measured excitation value with attenuation and phase shift configuration corresponding to the configuration used while measuring the embedded elements, for the nth element.

4.3 Case of Study - APAR LRU

In order to demonstrate the extended initial type characterization technique proposed in Section 4.2, the line replaceable unit (LRU) radar demonstrator, which is part of the airborne phased array radar (APAR) project, was experimentally tested according to the guidelines of the proposed technique. The goal of the experiment is to characterize and calibrate the antenna radiation patterns of the LRU. In this context, the objectives of this case study experiment are to:

- Characterize the performance of all TR modules.
- Capture embedded element patterns for both V and H polarizations.
- Measure beam-steered patterns.
- Predict antenna array patterns using the collected data, and compare the results with measured beam-steered patterns.

This case study tested the LRU in receive mode only. For transmission mode, the TR module technology requires instrumentation capable of synchronized pulsed measurements, which is incompatible with the current capabilities of the Radar Innovations Laboratory's NF scanner. Moreover, in transmission mode, radars generate high power signals that are often above the maximum allowed power level of the instruments.

The following sections illustrate the experimental setup, detail the experiments performed, and discuss the results.

4.3.1 System Description and Requirements

All measurements were performed using the NF scanner located at the Radar Innovations Laboratory. Basically, the procedure consists of using the scanner to control both instruments, to scan the patterns, and to configure the operation of the LRU phased array demonstrator. In this manner, once the LRU has been correctly installed inside the chamber, it is possible to automate the complete procedure, making any further direct contact between operator and the AUT unnecessary.

A depiction of the LRU is presented in Figure 4.3.(a), where the chassis on which the LRU is mounted can be appreciated, as well as the physical TR module printed circuit board (PCB), and the front of the antenna aperture. The LRU consists of eight TR module PCBs, each of them containing 8 TR modules, for a total of 64 elements. The antenna is a dual-polarized aperture coupled 8×8 microstrip phased array, fed by the TR module PCBs.

The schematic of the LRU is provided in Figure 4.3.(b). It shows that the eight PCBs are connected using power combiners to form two independent transmit and receive beamformers. Each of the TR modules PCBs contains eight TR module channels that are fed by two independent internal 1 to 8 corporate feeds. The independent internal feeds make it possible to simultaneously transmit with one or more elements and receive with another, a feature that is critical for mutual coupling measurements. Also, each TR module consists of the following: a 6-bit phase shifter (PS) and a 6-bit attenuator (ATT) for conditioning the RF signal in phase and amplitude, respectively; a high

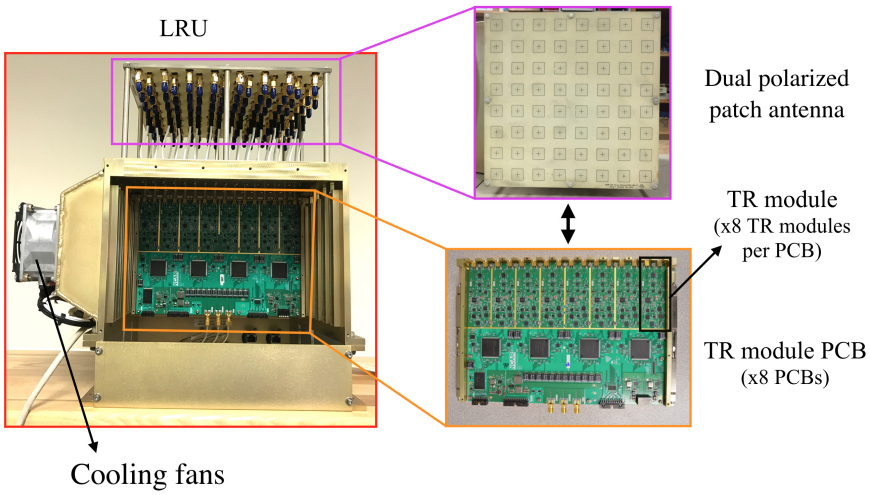

(a)

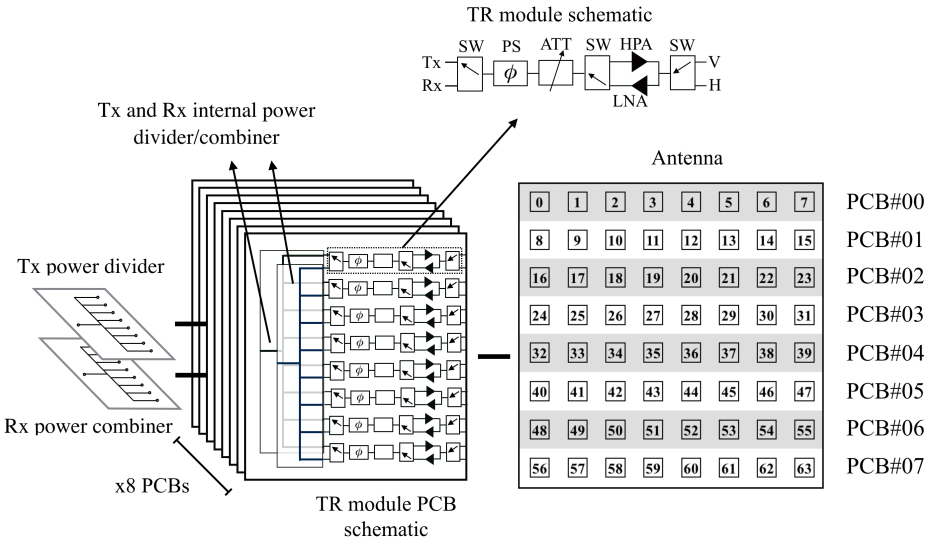

(b)

Figure 4.3: Depiction of the Line Replaceable Unit (LRU). (a) Picture of the LRU chassis, containing the PCB TR modules and dual-polarized microstrip patch antenna. (b) Schematic of the components of the LRU, including power combiners connecting all eight TR module PCBs; schematic of a TR module channel; and, antenna elements numeration.

power amplifier (HPA) for the transmitted signal; a low noise amplifier (LNA) for the received signal; and switches (SW) for commuting the electrical path between reception and transmission, and for choosing the antenna polariza-

tion. The phase shift step of the PS is $\Delta_{PS} = 5.625°$, and the attenuation step is $\Delta_{ATT} = 0.5$ dB.

In addition, a block diagram of the complete setup is shown in Figure 4.4. This figure identifies the main components of the experimental setup: the PC, which commands the procedure; the NF scanner, manufactured by NSI, the instrument that performs the experiments; and the antenna under test, which is capable of being configured according to test requirements.

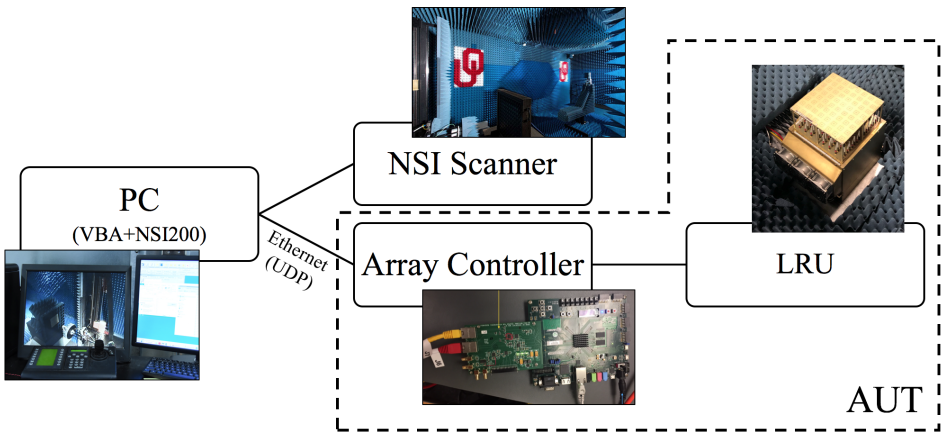

Figure 4.4: Block diagram of the experimental setup. The main components and instruments (NSI Scanner) are identified and their relations are properly depicted.

The PC belongs to the NF chamber, functioning as the processing unit, and has been adapted to command the AUT using the native scripting capability of the NSI2000 software. The PC is communicating with the AUT using an ethernet (UDP) protocol that is managed by the Array Controller of the APAR LRU. The Array Controller handles the communication and translates the received commands into orders that can be executed by the LRU. In this way the PC has control over both the instrument and the AUT.

Here is a typical procedure:

1. The PC executes a script written in Visual Basic (VB) using the NSI2000

library. It starts by initializing the scanning parameters.

2. The PC sends a command, defined by the script, to the AUT. The Array Controller receives the command and configures the LRU excitation.
3. The PC triggers a scan.
4. Repeat steps 2 and 3 until all requested tests are executed.

The arrangement of the instrument and AUT is depicted in Figure 4.5. The LRU was located on top of microwave absorber blocks inside the NF chamber, and carefully aligned to the scanner's probe. In order to reduce the reflections from the metal structure of the AUT, absorber foam was used to cover the periphery of the LRU.

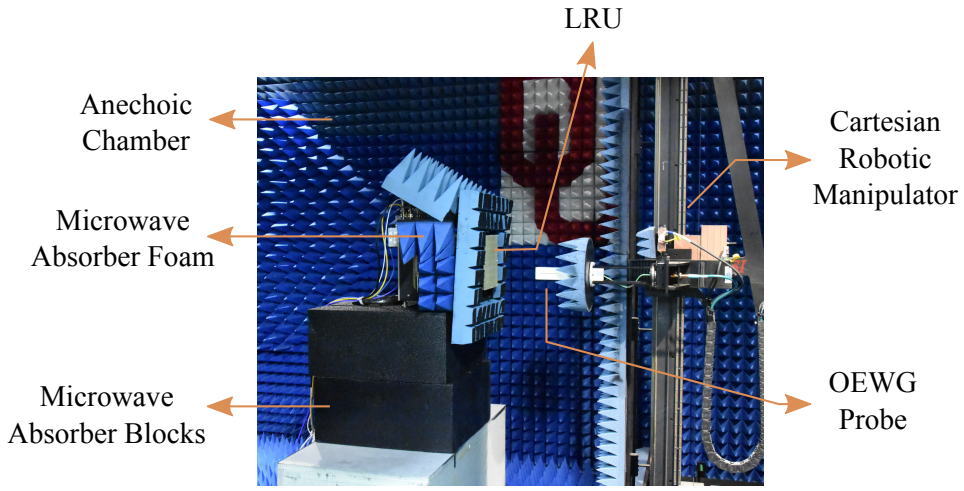

Figure 4.5: Picture of the 8×8 C-Band active array LRU sitting inside the NF anechoic chamber. The arrangement depicted is exactly the same used for all experiments performed on this chapter.

4.3.2 Experiment Procedure

The initial NF characterization and calibration of the LRU was carried out in four stages. The first stage, characterization, consisted of collecting the phase and amplitude data of each active antenna element, and quantifying

the misalignment among elements. The second stage captured the embedded element patterns, which are required to simulate the antenna patterns of the array. The third stage consisted of measuring beam-steered antenna patterns. For this, the LRU configuration was selected using the data collected in stage 1 to correct misalignment errors. Finally, the last stage uses the TR module data collected in stage 1 in conjunction with the embedded element patterns collected in stage 2 to synthesize, i.e. predict, the antenna patterns of the LRU. To verify that the predicted patterns are valid, the scanned patterns from stage 3 are used as a reference for comparison.

A step-by-step description of the experiments performed in each stage follows. In addition, a description of the technical details of the NF planar antenna measurements performed in this chapter is presented in Appendix A.

Stage 1 - Characterization of the TR Modules

The characterization stage is essential for the initial calibration of the LRU. It allows quantification of the performance of the attenuators and phase shifters contained in the TR modules. The objective is to use the park and probe technique to sample, for all channels in the array, each phase shift and attenuation stage combination in their array environment.

To accomplish this, the first step is to align the array to the NF robotic manipulator. This translates into having the aperture of the antenna under test (AUT) positioned parallel to the scan plane of the antenna probe, ensuring that the probe-AUT distance is the same during the entire scan. The antenna probe and antenna element should have their boresights aligned. The probe-to-AUT distance for all the experiments of this chapter was $4\lambda_0$, where λ_0 is the wavelength corresponding to the lower limit of the tested frequency range.

Afterwards, the procedure is:

1. Positioning of the probe exactly in front of the first element of the array.
2. Sending of excitation phase shift and attenuation parameters to the LRU controller by the NSI2000 software.
3. Triggering of an S-param measurement by the NSI2000 software.
4. Repeating steps 2 and 3 for all 64 phase shifts $\times$ 64 attenuations, for a total of 64×64=1024 samples per TR module.
5. Rotating 90° to test the other polarization, and repeating step 4.
6. Move to next element and repeat steps 1-5, for all 64 elements.
7. Export collected data for all frequencies of interest. In this case, 5.35 GHz.

Notice that for the LRU case, the attenuators and phase shifter are the same for both polarizations due to the architecture of the TR modules. As a consequence, in step 5 it is not necessary to test all combinations of phase shift and attenuation, since this information can be obtained from the data collected in step 4 for the first polarization tested. However, one sample at the default attenuation and phase shift stage must be performed for the second polarization so that this information may be used to normalize the data obtained for the first polarization.

As indicated by the park and probe theory, given in Section 4.2, only the tested element is active when sampled. The remaining elements should be terminated to their corresponding transmission line impedance value.

Once the data has been collected, the amplitude and phase differences between elements are calculated using (4.6) and (4.7).

Stage 2 - Embedded Element Patterns

To capture the embedded element patterns of the LRU, the array should be aligned to the NF scanner window, just as in stage 1. Afterwards, the following steps are executed:

1. Sending of excitation parameters to APAR by the NSI2000 software. Only one element is to be excited to an arbitrarily-defined $w_n^{embedded}$, while the remaining ones should be disabled, i.e., terminated to their corresponding match impedance. In this case $w_n^{embedded}$ corresponds to the complex weight obtained when $phs_{stg} = 0$ and $att_{stg} = 0$.
2. Triggering of a pattern scan by the NSI2000 software.
3. Repeating for all 64 elements and 2 polarizations, for a total of 128 patterns.
4. Exporting collected data for all frequencies of interest. In this case, the results are shown at 5.35 GHz.

Stage 3 - Beam-steered Patterns

First the excitation data was processed to select a set of w_n^r values using (4.18), just as explained in Section 4.2.4. In this case no taper is implemented. The array is uniformly illuminated, hence all target amplitudes are chosen as unity, i.e., $|w_n^{target}| = 1$.

The procedure to capture the patterns is the same as that described in stage 2, with the exception that in this case all elements are active and configured to their corresponding w_n^r stage.

Stage 4 - Array Antenna Pattern Synthesis

The pattern prediction is computed using (4.21), using the set of w_n^r values obtained in stage 3, and the f_a patterns scanned in stage 2. The objective of this stage for this particular case study is to evaluate the agreement between predicted and measured patterns.

4.4 Measured Results

4.4.1 TR Module Characterization

To illustrate the TR module characterization data, the sampled amplitude and phase of consecutive stages of attenuation and phase shift are shown in Figure 4.6. Figure 4.6.(a) presents the sampled amplitude, as blue circles, and phase, as red circles, for all attenuation stages at a fixed phase stage. Since the attenuation stages are tested and the phase configuration is kept constant, the results should show a linear variation of the magnitude and a constant phase for all attenuation stages. The linear variation of the amplitude is clearly seen in the top plot of Figure 4.6.(a). Nevertheless, the phase also varies at different attenuation stages even though the phase stage is kept constant, as shown in the bottom plot. This plot shows that the phase can vary $\approx 40^\circ$ by changing only the attenuation configuration of the TR module.

This non-ideal behavior of the phase excitation is due to unwanted effects on the electrical path of the attenuator, which alter the phase even though only the attenuation was expected to change. Moreover, the phase change plot shows a trend, namely, that the phase consistently decreases with the attenuation stage, demonstrating that this is a systematic error and not a random one. The 40° phase drift is a critical error for two reasons: first, it is a considerably high error, and second, it is also a systematic error. Hence, as

discussed in Chapter 2, this critical error has a significant adverse impact on the synthesized beam.

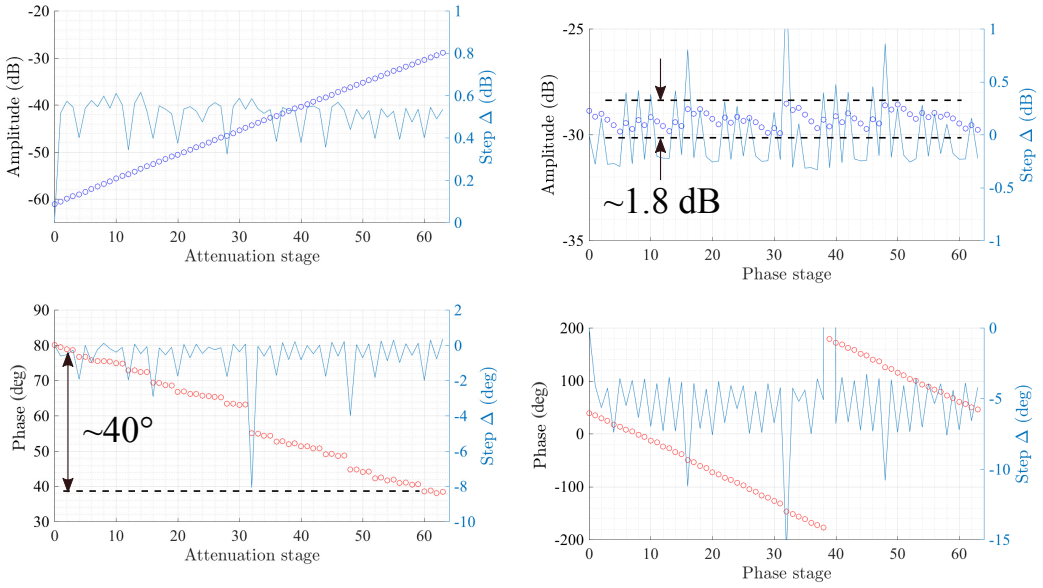

(a) Measured excitation values at a fixed phase shift stage, for all attenuation stages.

(b) Measured excitation values at a fixed amplitude stage, for all phase shift stages.

Figure 4.6: Sampled amplitude and phase data. Samples are plotted for TR module 0 as circles, blue for amplitude, and red for phase, at consecutive stages of attenuation (left), and at consecutive stages of phase (right). The step axis indicates the difference between the value of the current stage and the value of the preceding stage. Notice the bottom left plot ideally should appear as a straight horizontal line since the phase stage is kept constant. In a similar fashion, the top right plot should also be a straight horizontal line.

The continuous light blue curve, present in all plots of the figure, represents the step, Δ, in amplitude or phase, between consecutive stages. The amplitude plot at fixed phase stages, i.e., the top plot of Figure 4.6.(a), indicates a trend of a step of 0.5 dB between consecutive amplitude stages, which is expected since the attenuator modules used in this TR module have attenuation increments of 0.5 dB per stage. However, in this case, the step Δ plot also displays a ripply and cyclical shape, which indicates that the steps are not always 0.5 dB, and

instead vary systematically according to the chosen amplitude stage. This is also another clear example of unwanted systematic errors due to imperfect TR module hardware.

Figure 4.6.(b) presents an analogous situation, but in this case keeping the attenuation stage constant, and varying the phase stage. Hence, the magnitude ideally should be constant and the phase should change in steps of $\Delta_{PS} = 5.625°$. Nonetheless, the top plot demonstrates that the magnitude is not constant, and instead; it ranges approximately from -30 to -28.2 dB, which represents an unwanted variation of 1.8 dB. The phase plot at a fixed attenuation stage, i.e., bottom plot of Figure 4.6.(b), shows that the phase varies linearly with the phase stage, just as expected. Its step Δ plot indicates that between consecutive phase stages, the phase changes between from 4° to 8°. Ideally the steps should all be 5.625°, as mentioned before, but there are systematic cyclical errors specific the phase stage selected that prevent it.

The systematic errors of 40° and 1.8 dB found during the characterization of the TR module performance, Figure 4.6, represent a big concern for the correct operation of the phased array. For example, when applying a taper to the array by choosing higher attenuation stages, a systematic phase shift error is also added. Hence, tapered patterns necessarily require compensation in order to remove systematic errors. A similar problem arises when choosing the phase stages for beam steering, since a systematic amplitude is introduced due to the non-ideal behavior of the phase shifters. These errors are one of the main motivations for performing phased array calibration.

The amount of TRM data collected is very large, making it difficult to display all of it. To summarize the results, a plot enabling comparison of the amplitude and phase of each TR module at a fixed value of phase and attenu-

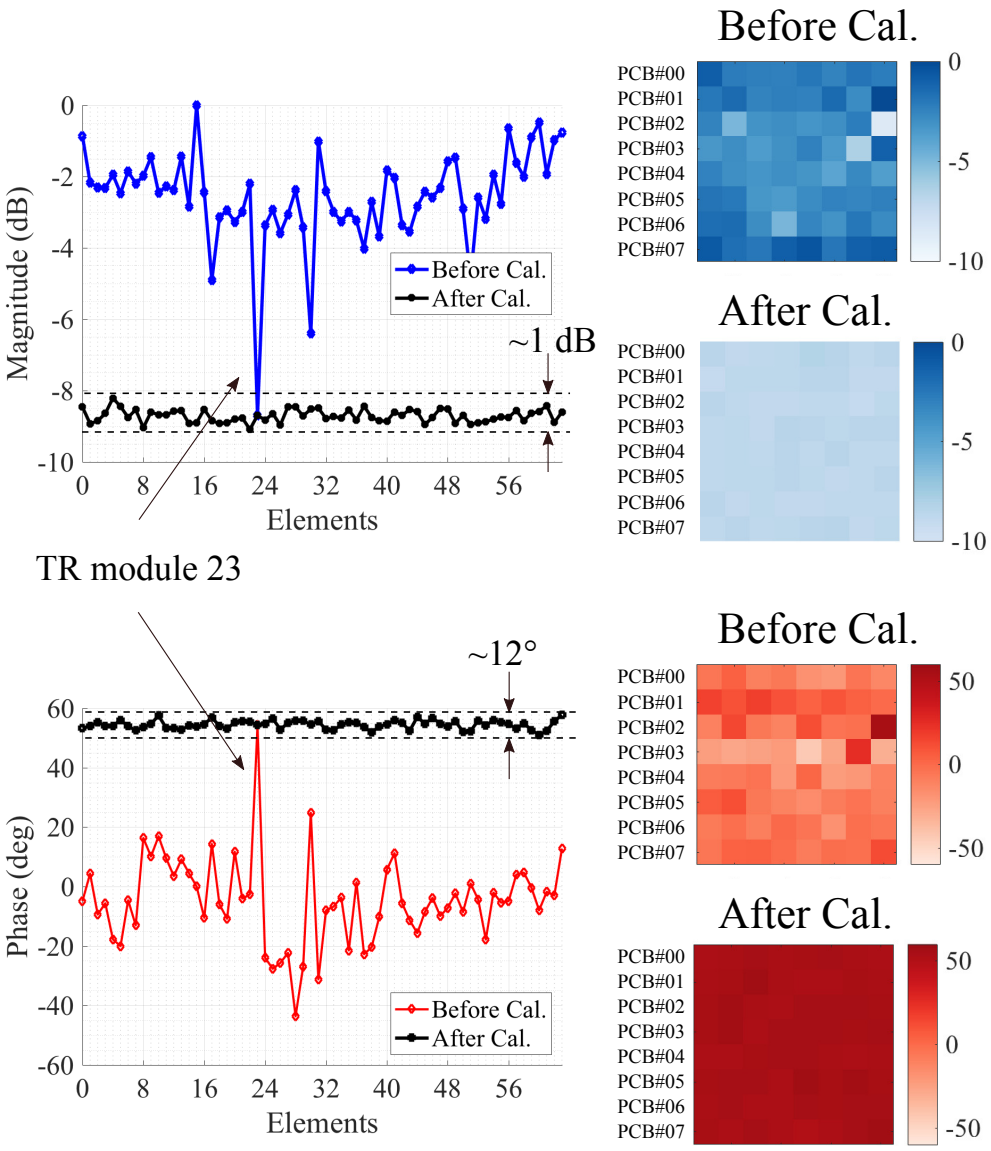

Figure 4.7: Sampled amplitude and Phase, for H-polarization, representing all 64 elements. Data is plotted in 1D (left), and in a 2D 8×8 grid arrangement (right). All TR modules were configured to 0 dB attenuation and 0 degree phase shift (att_{stg} =63, phs_{stg} =0). The top plot represents the amplitudes, and the bottom demonstrates the phase. The data was normalized with respect to the element with the highest amplitude value.

ation stage is generated. Figure 4.7 shows 8×8 arrangements, representing all 64 elements of the array. For the "Before Cal." case, all TR modules were configured at minimum attenuation stage (att_{stg} =63) and no added phase shift

(phs_{stg}). Ideally the 8×8 grid should display a homogeneous color, and likewise, the blue (amplitude) and red (phase) curves should be horizontal. This is because it is expected that at the same att_{stg} and phs_{stg} stages, all channels should behave similarly. However, as mentioned in the previous paragraph, there are errors in the TR module hardware that add a different bias to all elements. Thus, different color tones appear on the "Before Cal." plot.

Both phase and amplitude data in Figure 4.7, show that TR module number 23 has excitation values completely off the average. Element 23 presents a phase of 54.4° and a extremely low amplitude of -8.7 dB below the max value, this low amplitude corresponding to the minimum amplitude measured for all elements. Because these errors deviate the most compared to any other element, this translates into a beamforming problem, where element patterns do not add coherently. A deviation of 8.7 dB is a considerably large error. A closer inspection of active element 23 revealed that the cause of the error was a bad solder of the antenna connector.

Additionally, apart from the obvious random errors shown in Figure 4.7, there are also systematic errors difficult to notice.The 2D plot at the top, right shows that the elements belonging to PCBs 00, 01, and 07 have darker colors, indicating higher amplitude than the remaining boards. Moreover, the 2D "Before Cal." phase plot (lower, right in Figure 4.7) shows that the 4th row, corresponding to the elements of PCB 03, has a lighter tone than the rest, which translates into lower phase values than the other rows. These observations denote that elements on the same PCB board have similar excitation errors, hence, one can expect errors grouped in rows. This is a systematic type of error, occasioned by the particular architecture of the LRU, which implements a PCB board per row.

Apart from illustrating the initial misalignment errors of the LRU, Figure 4.7 also presents the state of the array after calibrating it for uniform illumination at boresight by using (4.18). The 2D "After Cal." cases for amplitude and phase show a more homogenous color pattern, as expected from a uniformly excited array. The top left plot, which represents the before and after calibration amplitude curves, indicates that after calibration the amplitudes are contained in a span of 1 dB, or ± 0.5 dB. The calibrated phase excitations are limited to a peak to peak change of 12°, or $\pm 6°$. These error ranges are expected; they are a result of the criterion selected for calibration, which chooses complex weights closer in both phase and amplitude to the target value. Thus, all the chosen excitations deviate from the target $\pm\Delta_{ATT} = 0.5$ dB and $\pm\Delta_{PS} = 5.625$ °, at most.

Alternatively, if one chooses a different criterion than the one in Figure 4.7, for example, choosing to prioritize amplitude errors over phase, then it will be possible to reduce the error span from 0.5 dB to half this value. This is due to the fact that a target value in between two consecutive states is at most half a step away from one of them. In this case, the trade-off is an increase in the spread of phase errors.

Finally, in this case, a selection criterion was made to equalize the amplitude of all elements to the amplitude corresponding to the element with the lowest value. This selection criterion was motivated by the fact that all elements were configured to yield maximum power. Hence, the elements with more power have to be attenuated to level down to the element with lowest power. As a consequence, even though the excitations were equalized and carefully chosen, the antenna gain is reduced.

4.4.2 Embedded Element Patterns

To illustrate the results of scanning the embedded element antenna patterns of an array using a NF planar scanner, Figure 4.8 presents the measured antenna patterns of element 27. In this case the elements of the LRU are microstrip patches characterized by typically having a low directivity of 8 to 9 dBi, and a beam width of $\geq 60^{\circ}$ [102]. Hence, the co-polar pattern of a patch antenna is a broad beam. On the other hand, the cross-polar components have nulls on the principal planes, and higher field values off this region, as shown in the 2D plots at the top left of Figures 4.8.(a) and 4.8.(b). The phase data, not shown in the figure, is also critical information since the embedded element patterns must be coherently summed to obtain the array pattern.

As a consequence of the beam shape of the co- and cross-polar patterns of a microstrip antenna, two issues arise from the antenna pattern scan point of view. First, due to the wide beam nature of the co-polar component of the pattern, NF planar scans are not advised for low gain antennas (see Table A.1). When an antenna pattern is wide, i.e., low gain, a planar scan is unable to scan enough fields to properly capture the radiation propagating in directions off boresight unless it extends the NF scan plane to unpractical lengths. In other words, a planar scan of a low gain antenna suffers truncation.

The core of a NF to FF transformation is a Fourier transform that converts the fields sampled in the Cartesian domain into the K_x, K_y and K_z wave spectrum, where K is the wavenumber. Truncation on a Fourier transformation can be seen as a windowing effect. Since the scan window is finite, the reconstruction of a broad beam will be missing information regarding the high harmonics. As a consequence, an unwanted oscillation is added to the calculated beam, and this is the reason why there are higher order oscillations noticeable

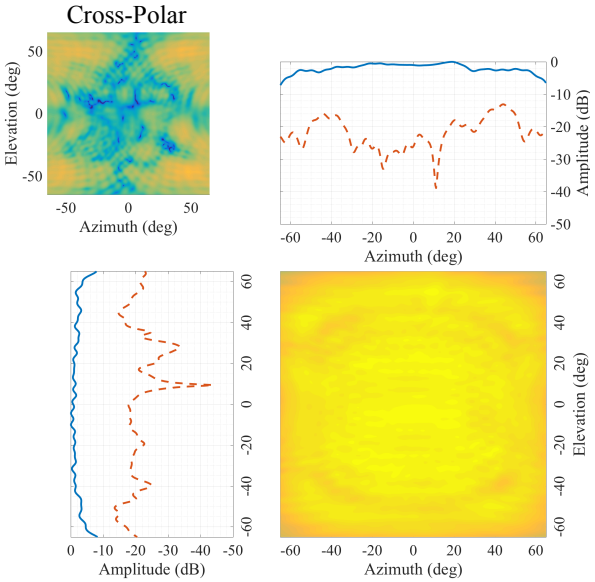

(a) V-Polarization

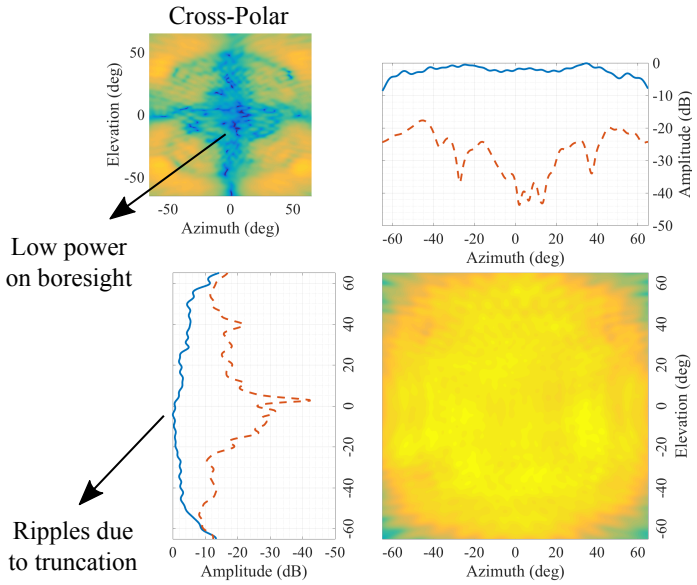

(b) H-Polarization

Figure 4.8: Scanned 2D plots and principal cuts of the embedded element patterns of element 27. (a) V-Polarization; (b) H-Polarization. The co-polar component is indicated by continuous lines, and cross-polar components by the dashed ones.

in the principal cuts of the embedded elements patterns.Consequently, the FF estimation of the embedded element patterns should not be used to analyze the performance of the particular element. However, the embedded element patterns are valid and useful to reconstruct the pattern of the array, which is a proper high gain pattern, using (4.21).

The second issue is related to the cross-polar component. At boresight of the cross-polar component, a null is expected. Hence, in this region, the SNR of the scanned fields is low. The deep null at boresight of the cross-polar component makes this angular sector of the cross-polar antenna pattern more susceptible to unwanted reflections caused by the AUT-instrumentation interaction. When the cross-polar components are summed together to compute the array pattern, using (4.21), the boresight region is perturbed by an accumulated reflection error. As a result, post-processed array patterns derived from the cross-polar component of the embedded elements will have poor accuracy at the boresight region, as will be demonstrated in Section 4.4.4.

4.4.3 Beam Steered Patterns

As a summary of the extensive scanning procedure, the overlapped scanned patterns over the principal planes are presented. The array was uniformly excited, and the set of complex weights w_n^r for each antenna element was chosen using (4.18). Figure 4.9 shows the co- and cross-polar azimuth beam-steered patterns from -45° to +45° on steps of 5° for both polarizations. The continuous lines indicate the co- component while the dashed lines correspond to the cross-polar component, the color blue represents the E-plane pattern, and the green the H-plane pattern. The elevation scan is shown in Figure 4.10.

For an ideal, uniformly illuminated array, the SLL expected is -13 dB,

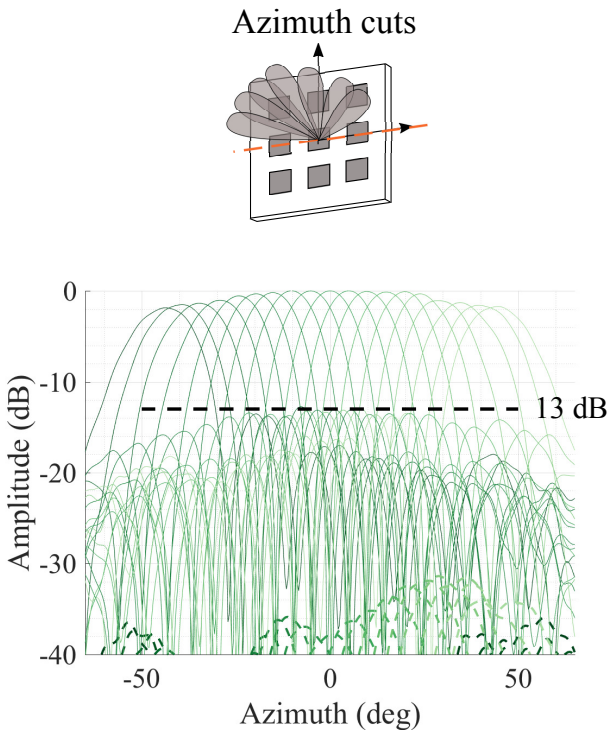

(a) V-Polarization, H-plane cuts

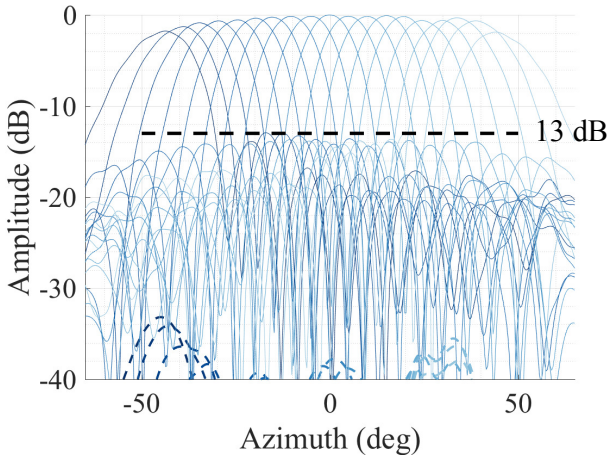

(b) H-polarization, E-plane cuts

Figure 4.9: Measured beam-steered antenna patterns, corresponding to azimuth -45° to +45°, in steps of 5°, uniform illumination. (a) Patterns corresponding to V-polarization. (b) Patterns corresponding to H-polarization. The co-polar component is indicated by continuous lines, and cross-polar components by the dashed lines.

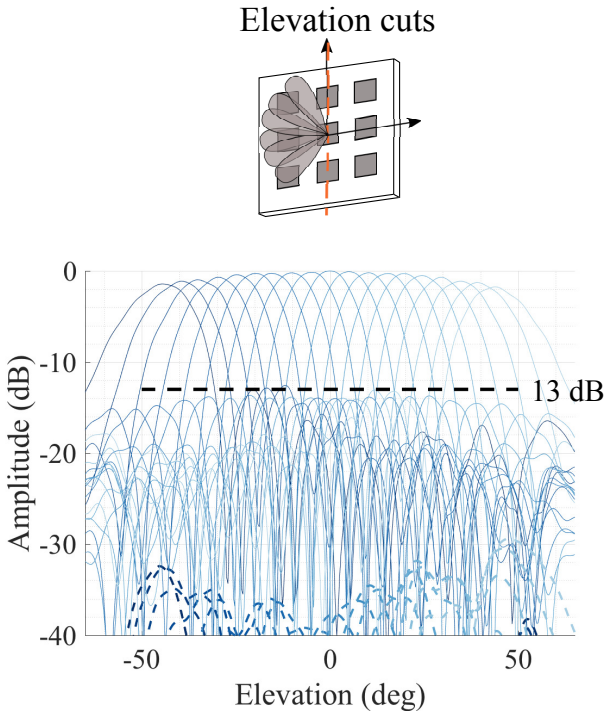

(a) V-Polarization, E-plane cuts

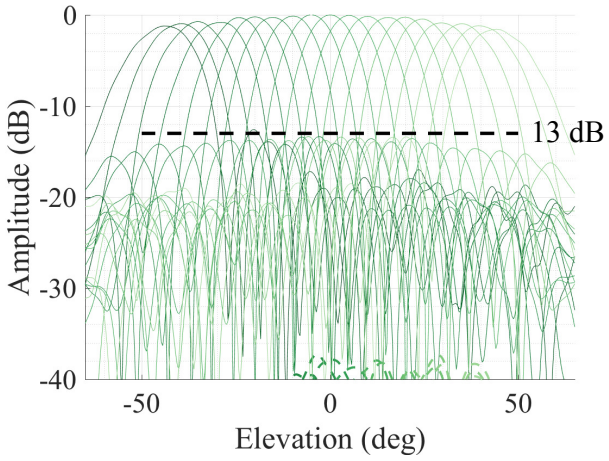

(b) H-polarization, H-plane cuts

Figure 4.10: Measured beam-steered antenna patterns, corresponding to elevation -45° to +45°, in steps of 5°, uniform illumination. (a) Patterns corresponding to V-polarization. (b) Patterns corresponding to H-polarization. The co-polar component is indicated by continuous lines, and cross-polar components by the dashed lines.

indicated by the black dashed lines in Figures 4.9 and 4.10. The SLL for almost all of the patterns is below this maximum level. However, at least one beam-steered pattern in each scan has a sidelobe that is only ≤ 0.2 dB above the -13 dB level. The reason for these errors is the combined effect of two factors: first, manufacturing imperfections in the radiating elements that prevent them from producing an ideal pattern; second, mutual coupling and diffractions that cause ripples on the radiated pattern of the array. This relatively small error can easily be compensated for by slightly tapering the beam-steered pattern. This error provides the motivation for perform NF measurements of the patterns before deployment, as they offer a sound basis for evaluating the realized antenna pattern even after a calibration has been performed. However, it is also possible to predict these errors by using (4.21) in conjunction with the collected TR module data plus embedded element patterns, as described in Section 4.4.4.

To demonstrate and further support the need for calibration, it is important also to depict the problems that may arise if the park and probe calibration technique is not implemented to quantify the phase and amplitude errors between elements. Figure 4.11 shows two measured antenna patterns with the main beam pointing to boresight (0°). On top, Figure 4.11.(a), the uncalibrated pattern is depicted, while on the bottom, Figure 4.11.(b), the calibrated one is presented.

The uncalibrated pattern in the figure reveals an unleveled SLL, nulls that are not as deep as its calibrated version, an overall aspect that is not symmetric, and, the most critical issue, a peak SLL that is ≈ 2.8 dB above its expected value. For this particular case, the root of these problems is the misalignment presented in Figure 4.7, and more critically, that TR module 23, according to

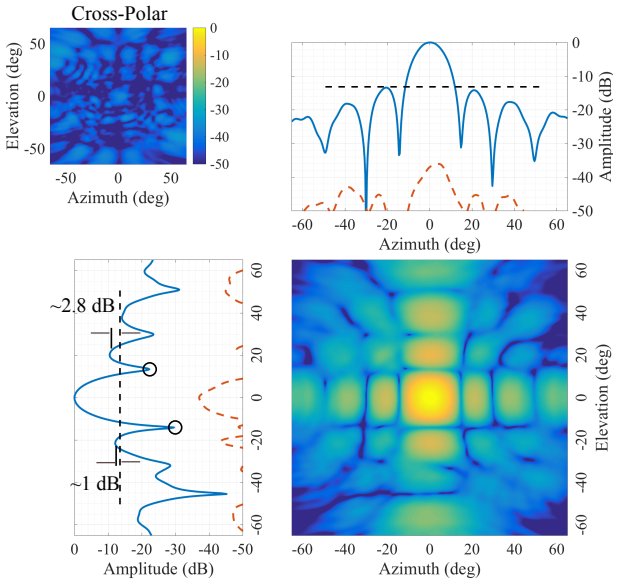

(a) Uncalibrated pattern

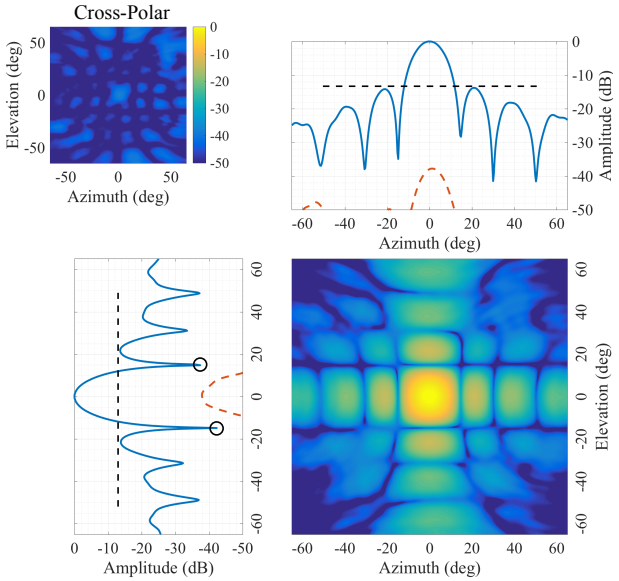

(b) Calibrated pattern

Figure 4.11: Measured boresight antenna patterns on H-polarization, uniformly illuminated, showing the differences between data without and with calibration. (a) Uncalibrated pattern. (b) Compensated pattern calibrated using the collected TR module data. The dashed black lines indicates the expected -13 dB SLL, and the black circles point to the nulls of the main lobe.

the results of the TR module characterization, had lower magnitude and phase levels with respect to the other elements, $\approx$ -6 dB and $\approx$ -45°, respectively. On the other hand, when the pattern is calibrated, the SLL is reduced to $\leq$ -13 dB, and the depth of the nulls are better defined, reaching a $\leq$ -28 dB level in the principal planes, as indicated by the black circles in Figure 4.11.(b).

A more severe case is expected when a taper is applied to the array. To better demonstrate the adverse effect of misalignment, an uncalibrated pattern with a Taylor taper of -20 dB was measured, as shown in Figure 4.12.(a). A taper forces some antenna elements to be excited at higher attenuation stages. As previously stated, at different attenuation stages, a systematic phase error is introduced. As a result, the tapered pattern is severely deteriorated. The SLLs on the elevation cut are 5 dB and 3 dB higher than the target -20 dB level, rendering this pattern unacceptable. Whereas, when the tapered pattern is compensated by calibration, the SLL reaches its expected level, and nulls are deeper making the shape of the lobes better defined.

The reviewed uncalibrated cases demonstrate that misalignment errors, of both types, random and systematic, are present in an uncalibrated pattern, and they severely impact the synthesized beam of the array. It is evident from these results that a phased array calibration must be applied to compensate for the errors, and ensure a correct antenna pattern beam shape.

4.4.4 Pattern Prediction

The pattern prediction is enabled by using the TR module characterization data collected in stage 1 and the embedded elements scanned in stage 2. In this case, the beam-steered patterns scanned in stage 3 were synthesized to verify the capability of the proposed characterization technique to predict phased

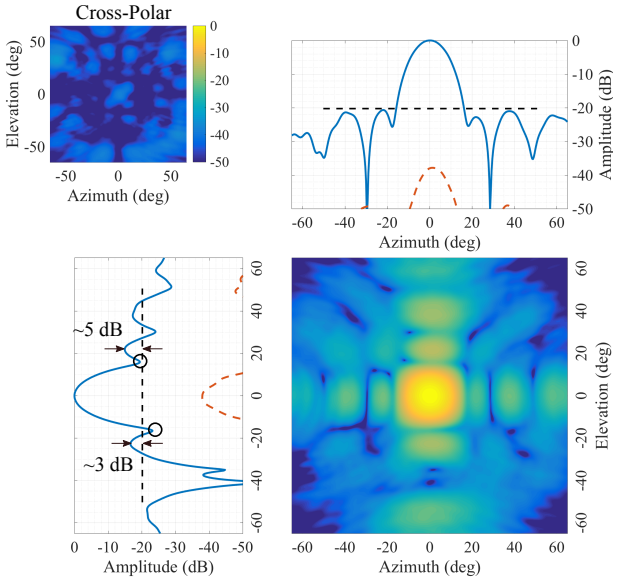

(a) Uncalibrated pattern

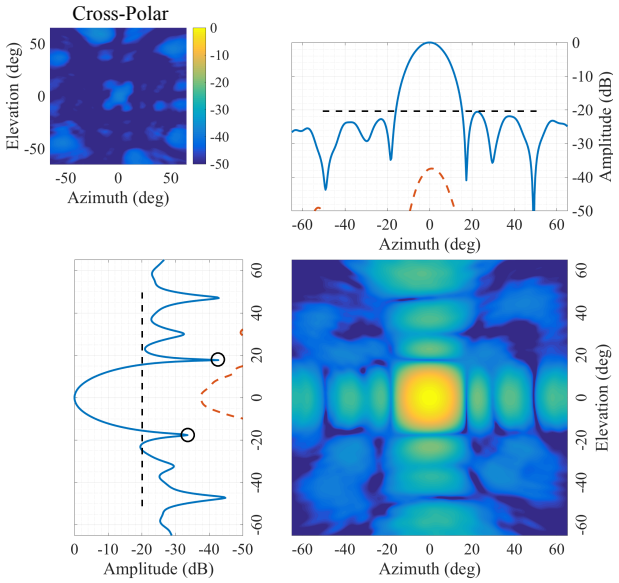

(b) Calibrated pattern

Figure 4.12: Measured boresight antenna patterns on H-polarization, with a -20 dB Taylor taper, showing the differences between data without and with calibration. (a) Uncalibrated pattern. (b) Compensated pattern calibrated using the collected TR module data. The dashed black lines indicates the expected -20 dB SLL, and the black circles point to the nulls of the main lobe

array beams.

Two cases are shown to present the prediction results, a beam pointing at boresight followed by a beam pointing at 45° in elevation. Both cases are depicted by their principle axis cuts and by a 2D plot of the pattern. The first case corresponds to Figure 4.13. The predicted co-polar component, traced in continuous lines in Figure 4.13, reproduce the measured patterns fairly well. . The match is better for azimuth and elevation angles closer to 0°, which is expected since antenna patterns obtained using a planar scanner decrease their accuracy at off-boresight directions.

On the other hand, the prediction of the cross-polar component seems not to be as accurate as the co component case. A 4 dB underestimation at boresight is evident in the azimuth and elevation cuts in the Figure 4.13. The reason for this is that the cross-polar component has its lowest value around boresight. As a consequence, the measurements of the cross-polarization of the embedded elements at positions close to boresight were very low in magnitude, i.e., exhibiting a low SNR. The result is that predictions for cross-polarization will not be as accurate as for off-boresight.

To demonstrate how cross-polarization predictions are better at angles away from boresight, an analysis of the predictions on a beam pointing to -45° in elevation is needed. Such a steered beam has a fairly high cross-polarization level compared to a boresight case, as shown inFigure 4.14. The azimuth cut, which is taken away from boresight, shows a very good match for both co- and cross-polar components, confirming the initial statement that predictions are better at off-boresight patterns.

As stated in the introduction of this chapter, sampling embedded patterns is not a standard part of the characterization procedure of phased arrays.

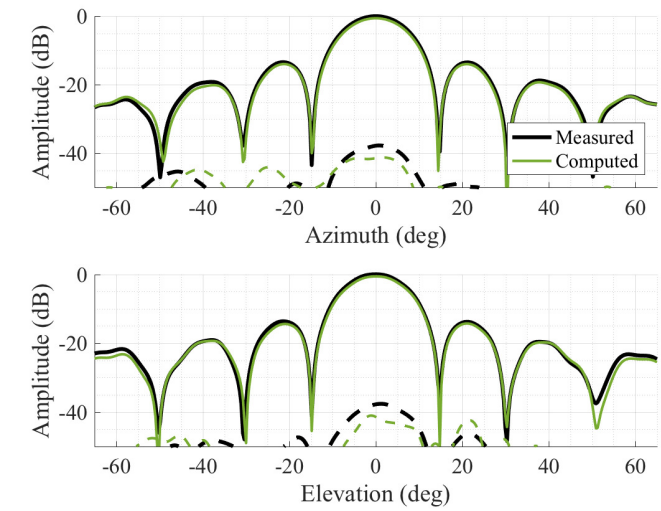

(a)

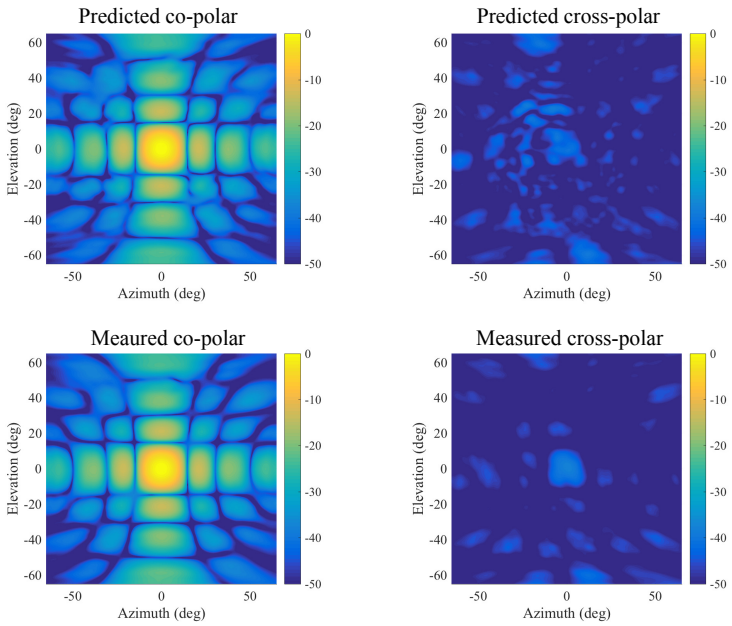

(b)

Figure 4.13: Comparison between measured and predicted antenna patterns at boresight. (a) Principle axis cuts, co- and cross-polar components plotted as continuous and dashed traces, respectively. (b) 2D representation of measured and predicted antenna patterns at boresight. The co-polar components are shown on the left, and cross-polar components on the right.

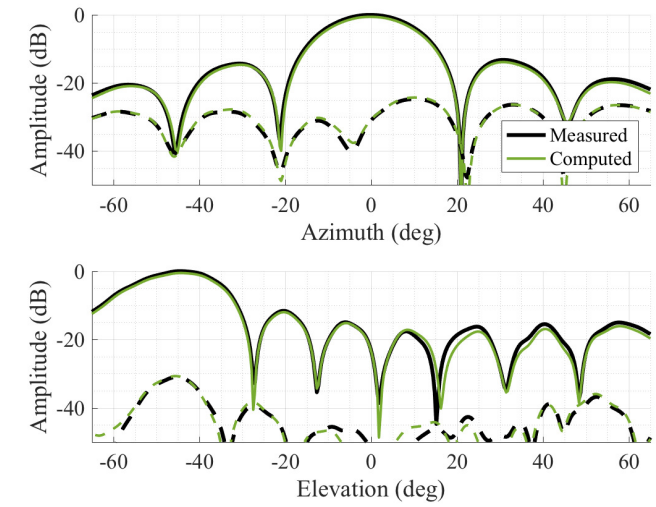

(a)

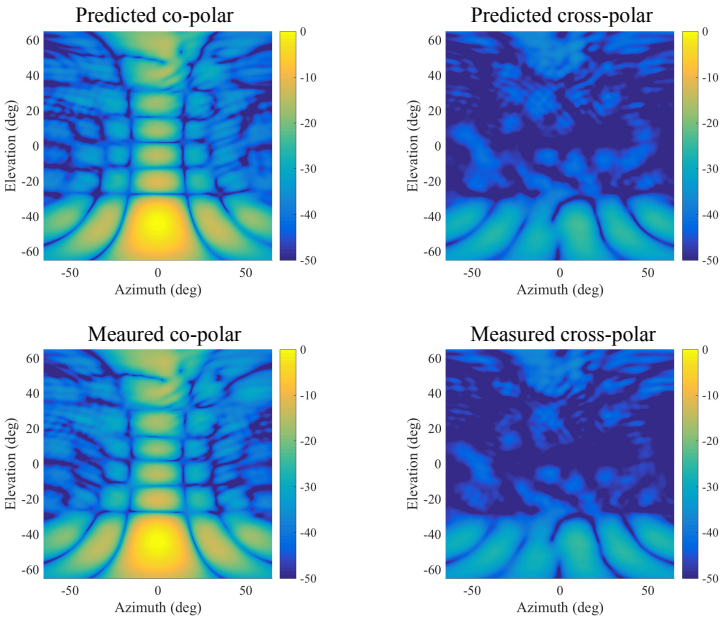

(b)

Figure 4.14: Comparison between measured and predicted beam-steered antenna patterns pointing to elevation -45°. (a) Principle axis cuts, co- and cross-polar components plotted as continuous and dashed traces, respectively. (b) 2D representation of measured and predicted antenna patterns at boresight. The co-polar components are shown on the left, and cross-polar components on the right.

These results show that their employment for pattern prediction is vital for prediction of co- and cross-polar components. It is especially relevant for cross-polar components, since their patterns are currently only obtained either by direct measurement of the beam, or by time consuming numerical computer-assisted simulations.

4.5 Summary

This chapter introduced a proposed complete characterization procedure for assessment of antenna patterns of phased arrays. It described the procedure as consisting of four main stages. First, TR module data is collected using the park and probe technique, which is the standard procedure for phased array calibration. It also added that, for a complete assessment of the phased array patterns, the embedded elements of each active element should be scanned in the second stage. Next, the third stage requires scanning beam-steered patterns of the array. The beam-steered patterns are corrected using the collected TR module data. Finally, the data collected in stages 1 and 2 can be used to predict the beam-steered patterns of the phased array.

The results demonstrated that hardware defects cause the electric paths of the TR modules, antenna, and transmission lines to vary. As a consequence, differences in phase and amplitude are found among antenna elements, and a maximum of 54.4° and -8.7 dB were found in this case. Differences were also found between expected steps in phase shift and attenuation, variations of 40° and 1.8 dB observed in these TR modules. Also, the results of the scanned beam-steered patterns showed that the effect of calibration is often to level sidelobes, deepen the nulls, and improve the overall shape of the beam.

Finally, pattern prediction has been qualitatively evaluated. It was found

that co-polar component patterns were well reproduced by computing them using the collected TR module data and embedded element patterns. However, the cross polarization accuracy can be off by 4 dB when predicting it near boresight. When the cross-polar component is predicted off-boresight, though, the prediction accuracy is largely improved.

5 Mutual Coupling-Based Initial and In-Situ Calibration

5.1 Introduction

This Chapter describes the work of Lebrón et al. [104], which experimentally validates an initial type calibration, and proposes a hybrid in-situ calibration technique, using in both cases mutual coupling feedback mechanisms. As it was explained in Chapter 2, the calibration can be classified in two main types, initial and in-situ [105]. As the name suggests, initial calibration is the first alignment check performed on the phased array system, whereas, in-situ calibration refers to the one performed on operation location.

Initial calibration is performed immediately after fabrication of the system. It is often performed under controlled conditions of temperature and humidity inside of an anechoic chamber. These testing conditions allows the utilization of specialized measurement instruments, as antenna NF or FF test ranges. The popular park and probe technique [28, 94], introduced in Section 4.2.2, is a great example of an initial calibration technique that employs a NF robotic scanner. Other techniques that require external equipment are [59, 64, 66, 67, 69]. By contrast, there are also techniques that take advantage of the inherent property of mutual coupling among elements of the array, and use it to avoid the employment of external equipment. The pioneers of this technique are Aumann et al. [50], and it was further investigated by [51, 32, 53].

On the other hand, misalignment errors that may appear during on-site operation are corrected by in-situ calibration. This type of calibration requires feedback measurements on location. However, in many occasions it is simply not feasible to deploy an external equipment for the sole purpose of calibration.

As a result, it is preferable to use techniques that are self contained as the ones mentioned in the previous paragraph which are based on mutual coupling measurements. In addition, some mutual coupling-based techniques can only be used for in-situ applications only, i.e., they require an initial calibration to be performed first, and the in-situ calibration will compensate only for the changes found between the current state and the initial calibrated state. Examples of this type of technique are [54, 23, 32], which employ embedded elements that monitor the current state of the array, and compare the results with the ones initially obtained.

On this chapter an experimental survey of initial and in-situ calibration techniques using mutual coupling as feedback mechanism is presented. The goal is to assess the performance of mutual coupling-based techniques to calibrate the small sized LRU introduced in Section 4.3.1. For the initial technique case the method proposed and simulated by Bekers et al. [53], and mathematically formulated by Mitchell [56], is implemented. This approach is capable of using the coupling among several different pair of elements to compute a least square minimum error estimate of the phase and amplitude difference between them. However, the approach suffers from biases caused by the discontinuities inherent to elements near the edge. Thereby, the feasibility of this technique is unknown for small-sized array cases. The motivation behind the selection of this technique is that it has not been experimentally validated yet, and its performance on array of small sizes is to be determined.

For the in-situ case a hybrid mutual coupling-based technique has been proposed and tested. The hybrid technique originates from the work of Şeker [32], and has been modified to track changes between the current state of the array and its initial calibrated state. The hybrid technique is motivated by the

need of using only mutual coupling measurements between the active elements of the array, avoiding the use of embedded elements which are required by the original change-tracking approach.

Moreover, to serve as a comparison reference, the reliable park and probe technique was implemented, and its results were used as ground truth to determine the root mean squared error (RMSE) of the misalignment values estimated using the tested mutual coupling-based techniques.

Furthermore, there is also a constant threat of element failure [106], which will compromise the mutual coupling-based calibration efforts, and it can adversely affect the resulting pattern. Thus, it is important to determine whether or not an element has failed. Fortunately, mutual coupling-based techniques not only allow one to quantify phase and amplitude misalignment, but their raw results by themselves contain information about the health of active element components. In case of component failure, the collected coupling data can be analyzed to determine failed active elements, and also to identify which component have failed. For this reason, this dissertation also describes how the raw coupling data was interpreted in order to quickly diagnose failed components.

The chapter is organized as follows, Section 5.2 introduces the theory of the initial type technique proposed by Bekers et al., while Section 5.3 presents the in-situ type calibration proposed in this work. Section 5.4 describes the mutual coupling-based calibration experiments performed on the LRU and their results. Finally, a summary of the discoveries is given in Section 5.5.

5.2 Mutual Coupling-Based Initial Calibration

The purpose of the initial calibration is to exhaustively test each active element of the array, to quantify its excitation levels. The mutual coupling-based calibration used in this work is the one proposed by Bekers et al. [53] and formulated by Mitchell [56]. The main advantage of the selected approach is that it provides a mathematical framework that estimates the misalignment, by least square method, in transmit and receive, using as much information as it is available. This contrasts with the techniques proposed by Aumann et al. [50] and Şeker [32], which do not propose a systematic methodology to use the redundant information provided by the coupling between all the elements. As a consequence, it is expected that the mutual coupling-based approach by Bekers et al. returns the most accurate results among all the techniques of this type.

To introduce the approach it is necessary to formulate the mutual coupling measurements using the coupling diagram shown in Figure 5.1. First, without lost of generalization, lets assume that all elements are configured to a default unitary complex weight, i.e., $w_n = 1$. Then, in a similar fashion as (4.1), a mutual coupling measurement consisting of a signal transmitted from element m and received by n, is formulated as,

$$R_{n,m} = k_n^r C_{n,m} k_m^t T. \tag{5.1}$$

The term $R_{n,m}$ refers to the received signal by element n, transmitted by m. The magnitudes k_n and k_m refer to the errors associated to the electrical path of the signal in the nth and mth elements, respectively. The term k_n lumps together the effect of the active component as well as the effect of transmission

Table 5.1: List of variables involved in the MC calibration technique. Adapted from [32].

Magnitude	**Symbol**	**State**
Signal from the mth element received by the nth element	$R_{n,m}$	measured
Signal transmitted from any antenna element to the probe	T	known
Coupling between mth and nth antenna elements	$C_{n,m}$	unknown
Amplitude/phase errors of the nth element in receive mode, due to active components, transmission lines, antenna and analog beamformer	k_n^r	unknown
Amplitude/phase errors of the nth element in transmit mode, due to active components, transmission lines, antenna and analog beamformer	k_n^t	unknown

lines, antenna, and analog beamformer. The super-indexes t and r indicate the value corresponds to the transmit or receive path. Finally, T indicates the transmitted signal. Notice that the original signal T is always contaminated by the transmit and receive error terms inherent to a microwave electrical path. Refer to Table 5.1 for a list and description of the involved variables.

Furthermore, the transmit/receive order is non-commutative, meaning that in general $R_{n,m} \neq R_{m,n}$. Consequently, swapping the transmit element with the receive element will produce a different pair, containing new information.

As in the case of park and probe, the goal of this approach is also to compute the error ratios k_n/k_{ref} between all active elements and a reference. This is accomplished by making any pair of active elements to test themselves, i.e., one element transmit while the other receives. The consequence of using different pairs of active elements for coupling measurements is that there is no longer a global reference, as opposed to park and probe that uses the probe to test all elements. In this context, the procedure can be seen as a guide

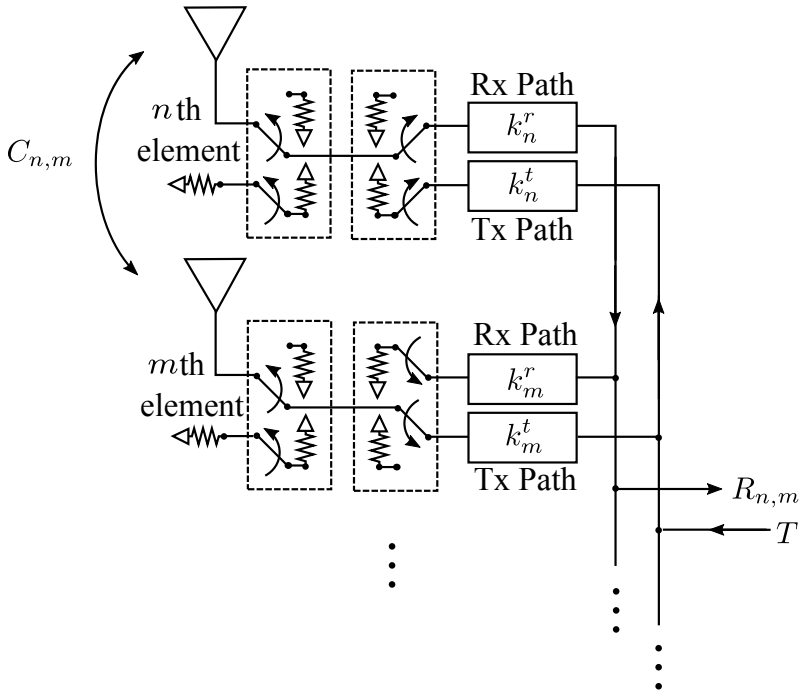

Figure 5.1: Coupling diagram for calibration measurements, in arrays with analog beamformer networks, using mutual coupling measurements. Test the nth element in receive, and the mth element in transmit. Adapted from [104].

describing what measurements should be taken, and formulating the equations to isolate the transmit and receive errors from the coupling samples.

The essence of the approach is based in the assumption that couplings between neighboring symmetrically disposed pair of elements have same values [53]. For this, the first step is to define coupling sets consisting of pairs of antenna elements with approximately equal coupling; e.g., for an square lattice of equally separated antenna elements, all pairs of elements that are immediate neighbors in a row constitute the [1,0] set, and all pairs of elements that are immediate neighbors in a column constitute the [0,1] set. These sets, and other sets that can be defined are depicted in Figure 5.2.

The following step is to identify combinations of two pairs within same sets and calculate ratios. For instance, for the subarray shown in Figure 5.2,

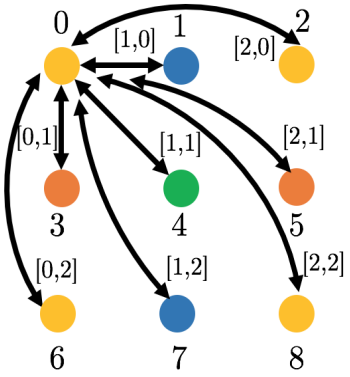

Figure 5.2: Depiction of coupling sets. For the mutual coupling-based initial technique proposed by [53], the couplings that belong to the same set are assumed to be of the same value. Source: [104]

within the set [1,0], one could choose the pair {0,1} and compare it to {1,2}, by assuming that they have approximately the same coupling. The computed ratio is,

$$\frac{R_{0,1}}{R_{1,2}} = \frac{k_0^r C_{0,1} k_1^t T}{k_1^r C_{1,2} k_2^t T} = \frac{k_0^r k_1^t}{k_1^r k_2^t}, \tag{5.2}$$

It follows from (5.2), that the ratio contains information of only the unknown errors.

In order to isolate the unknown error terms from the ratios calculated using (5.2), the technique suggests to linearize all ratios by reformulating their complex terms in magnitude, by using logarithms or by transforming to dB units, and in phase, by calculating their angle argument. In this context, it is possible to create two linear equation systems of the form [56],

$$\begin{bmatrix} 1 & -1 & 0 & 0 & 1 & -1 \\ & & \vdots & & & \end{bmatrix} \begin{bmatrix} (k_0^r)_{dB} \\ (k_1^r)_{dB} \\ (k_2^r)_{dB} \\ (k_0^t)_{dB} \\ (k_1^t)_{dB} \\ (k_2^t)_{dB} \end{bmatrix} = \begin{bmatrix} (R_{0,1})_{dB} - (R_{1,2})_{dB} \\ \vdots \end{bmatrix}, \tag{5.3}$$

$$\begin{bmatrix} 1 & -1 & 0 & 0 & 1 & -1 \\ & & \vdots & & & \end{bmatrix} \begin{bmatrix} \angle k_0^r \\ \angle k_1^r \\ \angle k_2^r \\ \angle k_0^t \\ \angle k_1^t \\ \angle k_2^t \end{bmatrix} = \begin{bmatrix} \angle R_{0,1} - \angle R_{1,2} \\ \vdots \end{bmatrix}. \tag{5.4}$$

The $\angle$ operator retreives the phase of a complex value, and the $(\cdot)_{dB}$ operator refers to,

$$(x)_{dB} = 20 \log_{10}(|x|). \tag{5.5}$$

The sparse matrix on the left side of (5.3), $\mathbf{A}$, is the same as the one in (5.4). Each row of the sparse matrix is composed of 1s and -1s, which represent the error terms that are in the numerator and denominator, respectively, of the linearized ratio. The number of rows of (5.3) and (5.4) depends on the number of previously defined pair combinations to process, while the number of columns is equal to the total number of unknown k_n^r and k_n^t terms involved. The column matrix that contains the unknown error terms is denominated $\mathbf{K}$. Lastly, the column matrix on the right side is $\mathbf{R}$, and it is composed of the measured coupling values $R_{n,m}$. Consequently, (5.3) and (5.4) have the

following form:

$$\mathbf{AK} = \mathbf{R}. \tag{5.6}$$

The objective is now to calculate the ratios K_n^r and K_n^t from (5.3) and (5.4). One way to accomplish this, is to choose a reference element and define,

$$k_{ref}^r = k_{ref}^t = 1, \tag{5.7}$$

which is the same as normalizing the errors with respect to the reference. In this way, (4.8) and (4.9) are simplified to $K_n^r = k_n^r$ and $K_n^t = k_n^t$. As a consequence, by calculating the k_n^r and k_n^t terms from (5.3) and (5.4), the unknown K_n^r and K_n^t ratios are also obtained. Moreover, (5.7) also results in

$$\angle k_{ref}^r = \angle k_{ref}^t = (k_{ref}^r)_{dB} = (k_{ref}^t)_{dB} = 0. \tag{5.8}$$

To solve (5.3) and (5.4) for k_n, Mitchell [56] proposed to split matrices $\mathbf{A}$ and $\mathbf{K}$ to reshape (5.6) into,

$$\mathbf{GK_1} + \mathbf{BK_2} = \mathbf{R}. \tag{5.9}$$

$\mathbf{G}$ is the sparse matrix $\mathbf{A}$ without the columns corresponding to k_{ref}^r and k_{ref}^t, while $\mathbf{B}$ is a two column matrix formed by the two columns removed from $\mathbf{A}$. $\mathbf{K}_1$ is the column matrix $\mathbf{K}$ without k_{ref}^r and k_{ref}^t terms, and $\mathbf{K}_2$ is a column matrix formed solely by k_{ref}^r and k_{ref}^t. Notice that $\mathbf{K}_1$ contains all the unknown variables; hence, to finally obtain the errors it is necessary to solve (5.9) for $\mathbf{K}_1$:

$$\mathbf{K_1} = \mathbf{G^{-1}}(\mathbf{R} - \mathbf{BK_2}). \tag{5.10}$$

$\mathbf{G}^{-1}$ is the pseudo inverse of $\mathbf{G}$.

For instance, if element 2 is chosen as ref, and taking (5.8) into consideration, (5.3) and (5.4) can be rewritten according to (5.10) as

$$\begin{bmatrix} (k_0^r)_{dB} \\ (k_1^r)_{dB} \\ (k_0^t)_{dB} \\ (k_1^t)_{dB} \end{bmatrix} = \begin{bmatrix} 1 & -1 & 0 & 1 \\ & \vdots & & \end{bmatrix}^{-1} \begin{bmatrix} (R_{0,1})_{dB} - (R_{1,2})_{dB} \\ \vdots \end{bmatrix}, \tag{5.11}$$

$$\begin{bmatrix} \angle k_0^r \\ \angle k_1^r \\ \angle k_0^t \\ \angle k_1^t \end{bmatrix} = \begin{bmatrix} 1 & -1 & 0 & 1 \\ & \vdots & & \end{bmatrix}^{-1} \begin{bmatrix} (R_{0,1})_{dB} - (R_{1,2})_{dB} \\ \vdots \end{bmatrix}. \tag{5.12}$$

Notice that there is no $\mathbf{BK_2}$ term in (5.11) or (5.12); this is because the error terms for the reference are zero, as specified by (5.8).

5.3 Mutual Coupling-Based In-Situ Calibration

In contrast to initial calibration, which is often performed indoors and under controlled environmental conditions, the in-situ calibration is periodically performed on the field, during operation of the system. Its objective is to regularly monitor the status of the active elements of the array, and take corrective actions in case partial or complete element failure occurs.

The mutual coupling-based technique detailed on Section 5.2 is a valid option for in-situ calibration. However, the large number of coupling measurements required and the high computational load imposed may increase testing and data processing time, making this technique less attractive for periodi-

cal monitoring of phased array with an analog architecture, because system operation will be interrupted for longer periods of time.

Moreover, the original mutual coupling-based technique proposed by Aumann et al. [50] and its variations [51, 32] are also great options for in-situ calibration of fielded large arrays, and they require less coupling samples compared to its improved version by Bekers et al. Nonetheless, both approaches rely on the assumption that coupling between an antenna element and its neighbors is the same for all elements along the array, which does not hold for small arrays due to unwanted edge effects.

On the other hand, there exists another approach that avoids the equal coupling assumption between neighboring elements, therefore making it an attractive option for in-situ calibration of both small and large arrays. The approach can be introduced as a before/after comparison. First, the status of the array when it has been initially calibrated is sampled and properly stored as a "before" status. Next, during operation, the same samples are repeated and compared to the before status. The ratio between the before and after status will quantify the changes suffered by the electrical path of the active elements. Still, the before/after approach does imply the assumption that the employed sampling coupling mechanism does not change in time, i.e., the coupling between two antenna elements $C_{n,m}$ is the same when taken during initial calibration and while fielded operation.

Examples of the before/after approach are proposed in [54, 32], which employ one or more embedded elements dedicated only to monitor the operation of the active elements. However, the use of embedded elements is also subject to dynamic range issues, i.e., an embedded element may not be able to test elements far away from it with enough SNR. In the case of digital phased ar-

rays, it is common practice to perform a self-calibration employing the active elements only. For instance, [55] exploits the inherent simultaneous reception on multiple elements capability of digital phased arrays to quickly test several elements per sample, and then use the redundant information collected to estimate the transmit and receive misalignment. From the analog phased array perspective, which can test only a pair of elements per sample, the latter approach is not efficient since it involves several coupling sampling repetitions to cover the same number of tested elements. Thus, to adapt the technique to analog cases, more effort should be directed on defining the set of coupling measurements to perform.

Keeping in mind that the goal of this dissertation is to investigate calibration techniques on an 8×8 active phased array, the in-situ technique to test must be compatible with small arrays with analog beamformer networks. Thus, it is proposed to use a hybrid in-situ/self-calibration technique that combines the before/after approach with the initial mutual coupling-based technique proposed by Ş [32]. The reason behind using the before/after approach is to avoid errors introduced by edge effects. Also, to avoid employing dedicated elements, the coupling measurements must be performed between the active elements themselves. This motivates the use of the technique proposed by Şeker, which defines the set of coupling measurements to test, and how to compute ratios from them. The following subsection details the proposed in-situ technique, including its limitations and benefits.

5.3.1 Hybrid In-Situ/Self-Calibration

As mentioned in the previous paragraph, this work proposes to implement a hybrid in-situ calibration technique. The technique consists of three steps:

1. After the initial calibration has been performed, sample and store a "before", or also called factory standard, status.
2. During operation of the system, interrupt it to sample an "after" status.
3. Compare before and after results to estimate changes on the receive and transmit modules.

To introduce the concept of the hybrid technique, the procedure is detailed in two stages. The first stage defines the coupling pairs to sample, and offers a methodology to process the collected data to obtain error ratios between antenna elements. This stage covers steps 1 and 2, and it is based on the mutual coupling-based calibration proposed by Şeker [32]. The second stage deals with the comparison procedure; it introduces the mathematical formulation to calculate the changes covering step 3.

The scheme defining the sample couplings is shown in Figure 5.3.(a). On the left side of the figure there is a simplified representation of a square array, and on the right side there are different coupling schemes for an arbitrary chosen 2×2 subarray. On each scheme there are four couplings depicted; all of the them can be formulated in the same fashion as (5.1). For the first case, the couplings are,

$$R_{2,1} = k_2^r C_{2,1} k_1^t T, \tag{5.13}$$

$$R_{2,4} = k_2^r C_{2,4} k_4^t T, \tag{5.14}$$

$$R_{3,1} = k_3^r C_{3,1} k_1^t T, \tag{5.15}$$

$$R_{3,4} = k_3^r C_{3,4} k_4^t T. \tag{5.16}$$

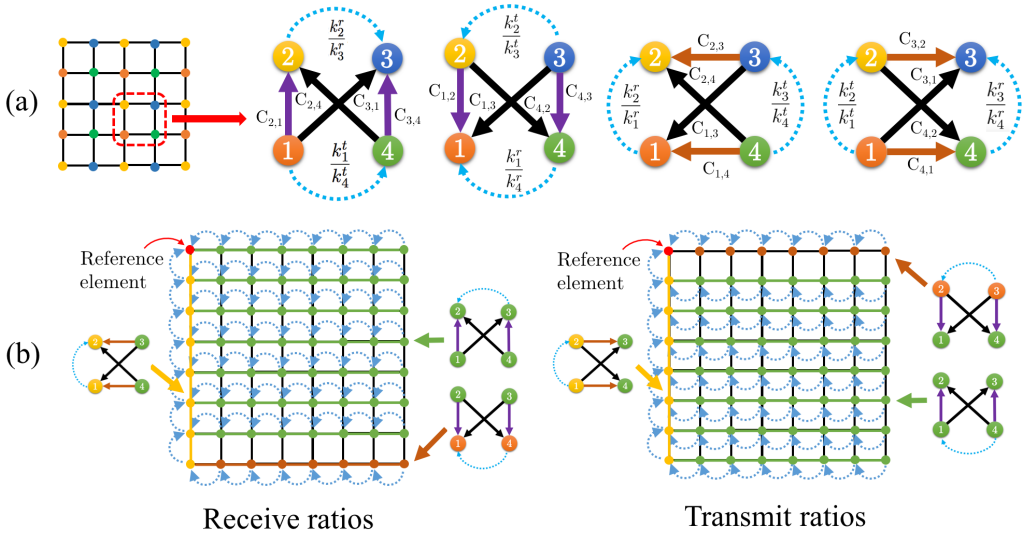

Figure 5.3: Coupling schemes proposed for in-situ/self-calibration. (a) For any 2×2 subarray, performing 4 coupling measurements obtains 2 error ratios between two pair of elements. (b) Different coupling schemes used to calculate error ratios among different pairs of elements. Source: [104].

In order to obtain the error ratios between elements, use (5.13), (5.14), (5.15) and (5.16), in the following expressions [32],

$$K^r_{3,2} = \sqrt{\frac{R_{2,1}R_{2,4}}{R_{3,1}R_{3,4}}} = \frac{k^r_2}{k^r_3}\sqrt{\frac{C_{2,1}C_{2,4}}{C_{3,1}C_{3,4}}}, \tag{5.17}$$

and

$$K^t_{4,1} = \sqrt{\frac{R_{2,1}R_{3,1}}{R_{2,4}R_{3,4}}} = \frac{k^t_1}{k^t_4}\sqrt{\frac{C_{2,1}C_{3,1}}{C_{2,4}C_{3,4}}}. \tag{5.18}$$

Expression (5.17) calculates the receive error ratio $K^r_{3,2}$ between elements 3 and 2 multiplied by a ratio among couplings, while (5.18) returns the transmit error ratio $K^t_{4,1}$ between 4 and 1, also followed by a respective coupling ratio. It is important to notice that the involved couplings in Figure 5.3 belong to set [0,1], shown in purple, to set [1,1], in black, and to set [1,0], in red. In an ideal case, couplings within the same set are similar, thus approximating the coupling ratios on the above two expressions to 1. Therefore, (5.17) and

(5.18) estimate 2 error ratios from 4 coupling measurements, and the level of accuracy depends upon how similar are same set couplings.

Nevertheless, until now only ratios between neighboring elements have been calculated, but the issue of how to relate these ratios to an arbitrary reference is unaddressed. To calculate the error ratios K_n between any element and the reference element, one must define ratio paths that link the reference to all other elements. A ratio path begins at any element and ends at the reference, and its purpose is to serve as a map indicating which ratios should calculated. For example, Figure 5.3.(b) shows a proposed set of ratio paths, for receive and transmit, using the top left corner element as reference. The ratio between any nth element to the reference is obtained as the product of all $K_{n,m}$ terms indicated in the ratio path, which is formulated as,

$$K_n^r = K_{ref,m}^r \cdots K_{q,n}^r, \tag{5.19}$$

and

$$K_n^t = K_{ref,m}^t \cdots K_{q,n}^t. \tag{5.20}$$

Indexes m and q represent the elements along the path. Moreover, Figure 5.3.b also details which 2×2 scheme type is used to sample the couplings.

In the context of the in-situ calibration, step 1 consist in implementing (5.19) and (5.20) immediately after the initial calibration to obtain a factory standard status set of $K_n^r|_{bef}$ and $K_n^t|_{bef}$ values, while step 2 repeats the same procedure as step 1, but while the phased array system is in operation at the deployment location, to obtain a new set of $K_n^r|_{aft}$ and $K_n^t|_{aft}$ values. Finally, to cover step 3 and calculate the amplitude and phase deviation from the

factory standard use [104],

$$(K_n^r)' = \frac{K_n^r|_{aft}}{K_n^r|_{bef}} = \frac{K_{ref,m}^r|_{aft} \cdots K_{q,n}^r|_{aft}}{K_{ref,m}^r|_{bef} \cdots K_{q,n}^r|_{bef}}, \tag{5.21}$$

and

$$(K_n^t)' = \frac{K_n^t|_{aft}}{K_n^t|_{bef}} = \frac{K_{ref,m}^t|_{aft} \cdots K_{q,n}^t|_{aft}}{K_{ref,m}^t|_{bef} \cdots K_{q,n}^t|_{bef}}. \tag{5.22}$$

Moreover, the assumption for this case is that couplings among elements do not change with time [104], i.e.,

$$C_{n,m}|_{bef} = C_{n,m}|_{aft}. \tag{5.23}$$

Replacing (5.17), (5.18), and assumption (5.23) in (5.21) and (5.22) yields [104],

$$(K_n^r)' = \frac{(k_n^r/k_{ref}^r)|_{aft}}{(k_n^r/k_{ref}^r)|_{bef}}, \tag{5.24}$$

and

$$(K_n^t)' = \frac{(k_n^t/k_{ref}^t)|_{aft}}{(k_n^t/k_{ref}^t)|_{bef}}. \tag{5.25}$$

The resultant expressions (5.24) and (5.25) calculate deviations from the original factory standard state. They must be used to track changes occurring after the system has been deployed, and they do not represent by themselves the current state. The most important advantage of these two expressions is that the coupling terms are canceled using (5.23) rather than the less likely assumption of equal same set coupling. Hence, there is no array minimum size imposition, and edge effects are no longer an issue for initial calibration. Another advantage is that this approach proposes a reduced number of coupling measurements, in contrast to the initial technique which requires as much

information as is available.

On the other hand, there are limitations that must be considered. The square root of complex numbers in (5.17) and (5.18) produces two possible results which are 180° apart. The first result, and the one used in this work, is in the range of -90° to 90°, which means that errors larger than |90°| will be incorrectly computed. However, large phase errors are not expected to arise during operation, unless the active element antenna and/or electronics have been damaged, in which case, it should be neglected from the calibration. Also, expressions (5.19) and (5.20) are prone to error propagation, i.e., measurement errors, caused by noise or repeatability, are present on each $K_{n,m}$ term, and they will accumulate along the ratio path. In other words, the longer the ratio path, the greater the possibility of larger accumulated error.

5.4 Case of Study - APAR

To validate the technique by Bekers et al. and the hybrid technique proposed in this work, both of them are tested on the LRU. The goal is to investigate the accuracy of mutual coupling-based calibration techniques to quantify the misalignment errors. For this, park and probe tests are performed to serve as a ground truth reference. The RMSE between the mutual coupling-based estimates and the park and probe reference is calculated as a figure of merit to evaluate the accuracy of the techniques.

The experiments performed in this work can be grouped in three categories, initial calibration, in-situ calibration, and detection and diagnosis of component failure. The initial type technique detailed in Section 5.2 is implemented to obtain the original misalignment of the system. For the in-situ type calibration the experiment forced an excitation change on few arbitrarily selected

elements, and then applied the technique proposed on Section 5.3.1 to quantify the changes. Finally, an overview of component failure cases encountered during testing is presented. The feedback data obtained from mutual coupling samples are instrumental to identify and diagnose component failure.

5.4.1 System Description and Requirements

The antenna under test (AUT) is the 8×8 C-band active phased array LRU prototype introduced in Section 4.3.1, and shown again in Figure 5.4. The AUT is dual polarized, however, for this work, only the vertical polarization was investigated. As previously explained, the TR module PCB boards were designed with two independent beamformer networks, one for transmit signals and another for receive. These independent networks are essential for mutual coupling measurements. All 8 beamformers are connected to a 8:1 power combiner, one combiner for transmit signals and another for receive, see Figure 4.3 for more details.

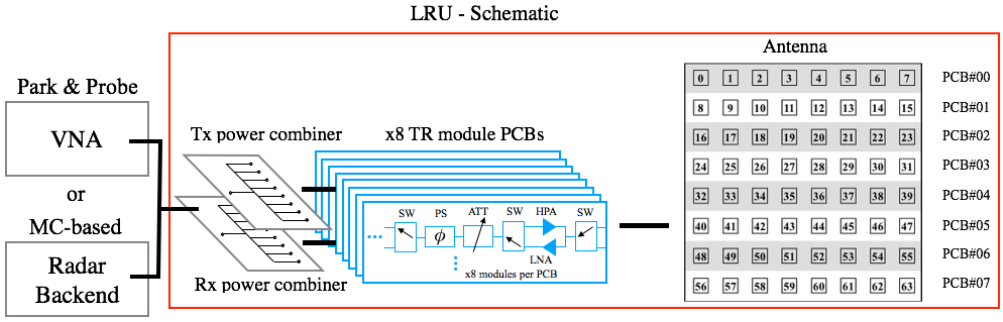

Figure 5.4: Simplified schematic of the LRU. Two independent analog beamformer networks are used to allow simultaneous transmission and reception. Source: [104].

The measurements were performed inside the custom made anechoic chamber developed by NCAR and introduced in Section 3.2, consisting of a metallic box covered with microwave absorber foam. The 4 degrees-of-freedom scanner

attached to the chamber enabled performing park and probe measurements, which serves as ground truth. The antenna probe used during these experiments is a WR-187 open ended waveguide. A VNA is employed to generate and digitize the signals for the park and probe experiments. The employed VNA included extra hardware features to allow pulsed measurements, which are required for the transmit mode. Whereas, for all mutual coupling samples, a radar backend was implemented instead of the VNA, which also allowed for pulsed measurements among elements. The signal generation and processing, for the radar backend, were executed using a Pentek transceiver board.

Figure 5.5 shows the setup for the experiment. The park and probe experiments were performed according to the configuration on Figure 5.5.(a). On the other hand, to perform the mutual coupling measurements, a metal plate covered with microwave absorbers was placed in front of the LRU. The absorber cover is used to block unwanted reflections from the metal frame of the scanner. Figure 5.5.(b) depicts the covered chamber, the microwave absorber stuck on the metal plate is inside the chamber.

5.4.2 Initial Calibration

The park and probe and mutual coupling-based technique by Bekers et al. were implemented. The former technique employed the scanner attached to the custom made anechoic chamber, and sampled all 64 elements in both receive and transmit modes, for a total of 128 samples. The error ratios between elements were computed using equations (4.6) and (4.7).

On the other hand, the mutual coupling-based technique was carried out connecting the transmit and receive beamformers to the radar backend. Several measurements were performed, for this case it was chosen to sample all

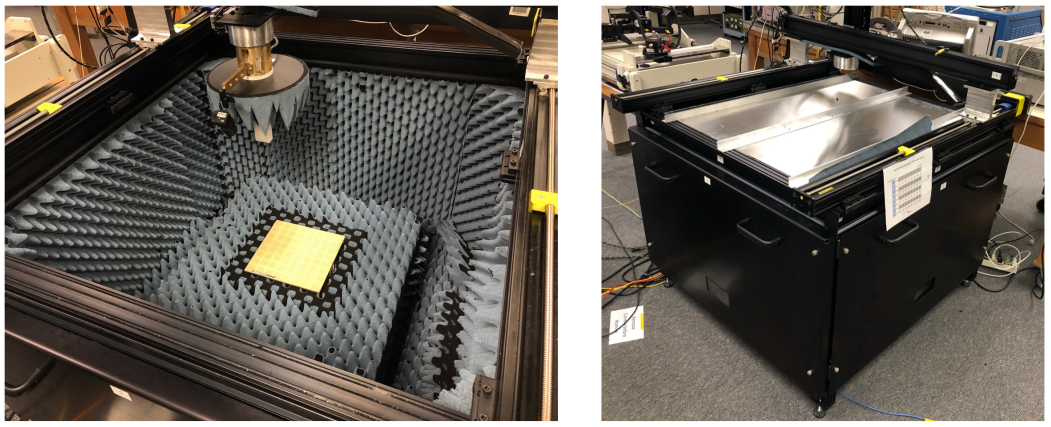

(a) (b)

Figure 5.5: Experimental setup utilized to perform the measurements. (a) The AUT is the 8×8 LRU mounted on the custom made anechoic chamber. For park and probe testing the 4 degrees of freedom scanner attached to the chamber is used to accurately position the open ended waveguide acting as antenna probe. (b) Configuration for mutual coupling measurements. A metal plate lined with microwave absorber is used on top the scanner to avoid reflections.

possible pairs that belong to sets [0,1], [1,0], [1,1], [2,0], [0,2] and [2,1], as proposed by [53]. A total of 780 samples were collected, which is a considerable larger amount of samples than the number of samples required for park and probe. Nonetheless, even though the mutual coupling-based technique requires more samples, there is no need for mechanical movements, which severely reduces testing time.

An important consideration of the techinique by Bekers et al. is its vulnerability edge effect. Antenna elements located at the edges of the array are exposed to a different environment than those located at the middle of the array, which causes their coupling values to vary, thereby compromising the assumption that couplings within the same set are equal. Simulations performed by Bekers et al. [53] indicate that estimation errors for an 8×8 array are low, e.g., in the order of 0.16 dB and 2.1°. However, the simulations assumed an array with an infinite ground plane, which is impossible to realize.

Table 5.2: Summary of RMSE of the mutual coupling-based initial calibration approach in reception and transmission.

Subarray	Reception - K_n^r	
	RMSE amplitude (dB)	RMSE phase (deg)
4×4	0.27	2.66
6×6	0.36	2.67
8×6	0.46	2.50
8×8	1.11	2.47
Subarray	Transmission - K_n^t	
	RMSE amplitude (dB)	RMSE phase (deg)
4×4	0.39	2.76
6×6	0.51	2.51
8×6	0.52	2.50
8×8	1.07	2.39

Consequently, the impact of the discontinuities occasioned by the finite nature of physical arrays is unknown, and it is particularly more relevant for the case of a small 8×8 array.

As a result, in order to properly assess the accuracy of the technique it is necessary to investigate different subarray arrangements. For this reason, 4 different subarray configurations were considered, as shown in Figure 5.6. For the first two cases the computation of the error estimations were performed on subarrays that consider only inner elements. In contrast, the last 2 cases consider configurations were edge elements are also included. The motivation behind using two different cases, 8×6 and 8×8 arrangements, to depict edge effect is that in this case it was found that couplings of elements located in vertical edges are more perturbed than in horizontal edges.

The results of these experiments, for both receive and transmit, are summarized in Table 5.2, and the estimated K_n^r in reception are shown in Figure 5.6. For each subarray case, the magnitude and phase estimations of the misalignment from the mutual coupling-based technique are compared to the

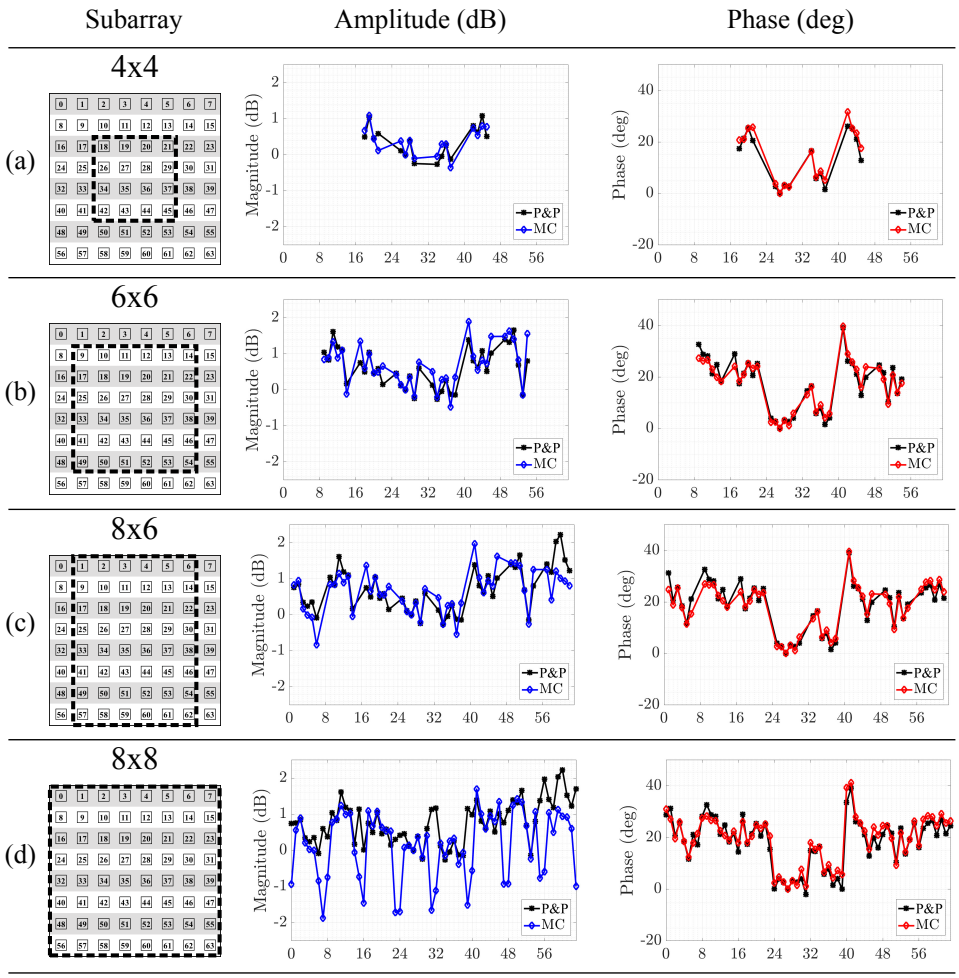

Figure 5.6: Estimations of the initial misalignment, in receive mode, of the LRU. The park and probe (P&P) results are compared to the ones obtained using the mutual coupling-based (MC) technique for different subarray configurations. The unwanted edge effect is most notorious on the vertical edges, affecting mostly the magnitude estimations. Source: [104].

ones from park and probe, which are defined as ground truth. As a figure of merit, the RMSEs are computed, the lower the RMSE the better the mutual coupling-based estimation. Element 27 was chosen as reference element for all subarray cases due to its center location, away from the edges and relatively close to all other elements.

By inspection of the values given in Table 5.6, one can notice that there

is a significant variation of the amplitude RMSE for the different cases. The closer the involved elements are to the edges, the worst the estimation. The worst result, $\text{RMSE}_{8\times8} > 1$ dB, occurs for the 8×8 case, which covers all edges, the estimated excitations for the elements on the left and right edges are completely biased. In contrast, if these edges are avoided, i.e., considering the 8x6 subarray, the error is reduced to $\text{RMSE}_{8\times6} \approx 0.5$ dB. This suggests that couplings on vertical edges are more perturbed than on horizontal edges for vertical polarization.

In contrast with the magnitude estimations, the phase estimations in this particular array were improved by increasing the array size. Still, the improvements are relatively small, 0.19 and 0.37 deg, for reception and transmission, respectively. This indicates that the errors are being reduced by averaging associated to the increased number of involved elements. The RMSE for all cases is close to 2.5°, which is a similar result to the RMSE predicted by simulations [53], 2.1°. As a consequence, it is possible to state that the mutual coupling-based technique, by Bekers et al., is a great option for phase estimation of misalignment on this small-sized array. However, for amplitude estimations it is recommended to either avoid including edge elements, or add dummy elements surrounding the active ones [106].

Moreover, a comparison between estimations in reception and transmission indicates that the RMSE are in the same order for both cases. This should not be a surprise considering that the main source of errors of this approach is the amplitude and phase differences among same set couplings, which were only assumed to be the same, and affect both transmission and reception in a similar manner.

5.4.3 In-Situ Calibration

The in-situ experiment was performed under similar conditions as the initial calibration. The LRU was located inside the custom-made anechoic chamber, and the transmit and receive power combiners were connected to the radar backend. However, for the in-situ case, arbitrarily defined amplitude and phase perturbations were introduced to the initial state of the array excitations. In this manner, the goal of the test is to accurately quantify the imposed changes using the hybrid technique proposed in Section 5.3.1.

The excitation changes were introduced by modifying the receive TR module configurations of a set of 6 arbitrarily chosen elements. Simultaneously, the TR module configurations of another set of 6 arbitrarily chosen elements were modified but for transmit. As a result, the new state of the active array comprehends 6 variations in both receive and transmit conditions.

In order to quantify the added changes, the measurements depicted in Figure 5.3 were performed, with the difference that for this test the reference element was element 27, located on the center of the array. Next, the recently collected data set, were used to compute a set of $K_n^r|_{aft}$ and $K_n^t|_{aft}$ coefficients using (5.19) and (5.20), respectively. Then, in an analog manner, to obtain a set of $K_n^r|_{bef}$ and $K_n^t|_{bef}$ values required for comparison, the data set collected during the initial calibration experiment, described in Section 5.4.2, was used in conjunction with (5.19) and (5.20). Finally, the added changes, $(K_n^r)'$ and $(K_n^t)'$, were computed with the help of (5.21) and (5.22), respectively.

The estimated amplitude and phase changes in receive and transmit are shown in Figure 5.7. As it is possible to appreciate, there are 6 peaks per plot, each representing the estimated value of the introduced modification. The unaltered elements are clearly noticeable since their values are close to

0, hence indicating they suffered no change. However, small variations within the unaltered elements are observed. The small variation can be contribution from factors such as temperature changes, measurement repeatability, non-linearity of the HPA, and low-level leakage within the T/R module channels. For this reason, as a ground truth reference, the park and probe technique was implemented to measure the introduced changes. The comparison between estimations and ground truth values are detailed in Table 5.3.

The phase estimation in reception are one order of magnitude less than those obtained using the initial calibration technique. In transmission the estimations are not as good as in reception. This is likely due to the HPAs not working in an ideal linear regime. In addition, the VNA calibration for park and probe measurements in transmission and reception were different, because they have different microwave circuits. For reception the calibration included all the setup, whereas for transmission only portion of the microwave setup was calibrated and de-embedded. A more precise calibration of the VNA plus microwave setup in transmission must be performed for the park and probe measurements to improve its estimation accuracy.

Nevertheless, the real advantage of the proposed in-situ calibration technique is that it greatly enhances the amplitude estimation for both cases, regardless of the location of the element. As it can be verified, the estimation in amplitude for any element is < 0.19 dB, while for the initial calibration case elements on the edges were underestimated by > 1 dB. The reason, as explained in the previous section, is that the passive coupling values are removed from the calculation by comparing the before and after states.

Table 5.3: Summary of the excitations changes, estimations, and RMSE obtained during in-situ calibration experiments.

Reception - $(K_n^r)'$						
Element	Amplitude (dB)			Phase (deg)		
	Value	Estimation	Error	Value	Estimation	Error
4	-2.91	-2.89	-0.02	-23.30	-23.03	-0.27
28	-1.16	-1.13	-0.03	21.60	21.70	-0.10
32	-1.88	-1.87	-0.01	29.38	29.90	-0.52
45	-1.97	-1.97	-0.00	2.15	2.12	0.03
46	-2.37	-2.31	-0.06	18.20	18.13	0.07
63	-2.04	-2.05	0.01	-7.73	-7.61	-0.12
RMSE	0.03			0.25		
Transmission - $(K_n^t)'$						
Element	Amplitude (dB)			Phase (deg)		
	Value	Estimation	Error	Value	Estimation	Error
15	-1.03	-1.07	0.04	-8.01	-8.04	0.03
28	-0.97	-1.14	0.17	22.50	21.10	1.38
29	0.18	0.37	-0.19	-5.53	-5.35	-0.18
32	-0.02	-0.12	0.10	-8.80	-9.70	0.90
54	-1.58	-1.66	0.08	12.70	11.92	0.78
56	-1.94	-2.05	0.11	22.30	22.28	0.02
RMSE	0.12			0.75		

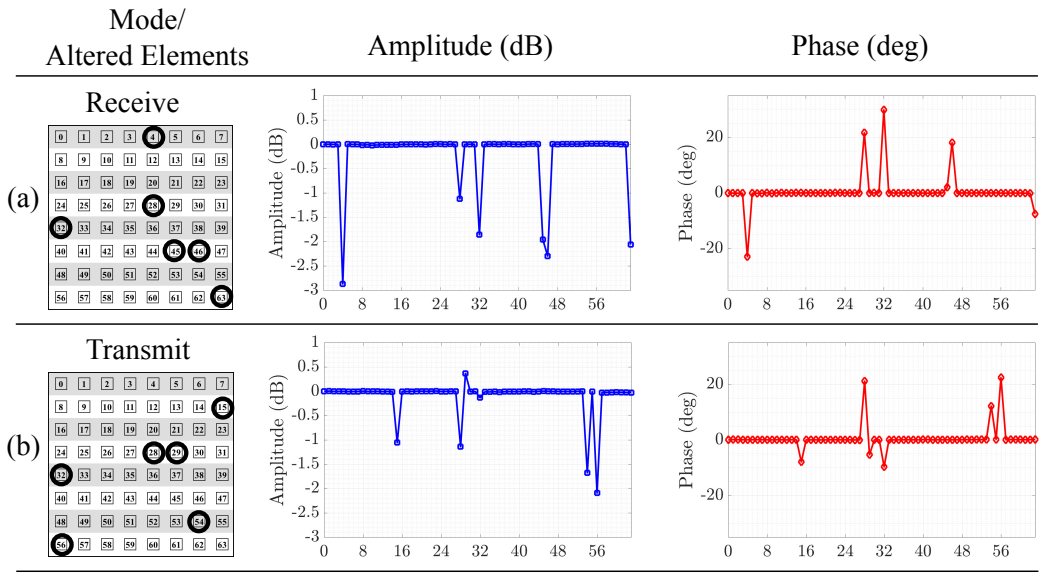

Figure 5.7: Estimations of the introduced changes in amplitude and phase, in receive and transmit mode, of the LRU. For each mode, the excitations of 6 elements were modified and later detected by the proposed mutual coupling-based in-situ error tracking technique. Source [104].

5.4.4 Component Failure Diagnosis

In addition to calculate amplitude and phase misalignment along the array, mutual coupling measurements can be used to quickly identify component failure in a system. In order to support this statement a collection of common failure cases, which were found over the course of the experimentation period, is presented. The cases include examples of damaged high power amplifier, bad antenna connection, and complete failure of TR module board.

Figure 5.8 shows the aforementioned cases. The cases are introduced in terms of sampled coupling values, which are summarized in the square grids shown in the figure. Each pixel in the grid represents the received value resulting from transmitting a signal with one element and receiving it using another element, while the rest of the elements are terminated. These samples are taken exactly as specified by Section 5.3.1. The rows of the grid indicate the

transmitting element, while the columns indicate the receiving element. As a result, the values contained in the nth row represent the received signals by all elements that were transmitted by element n. Whereas, the nth column displays the received values by the nth element, which were transmitted from all other elements.

Figure 5.8.(a) is the measured result of sampling all possible couplings within the 8×8 array in the absence of failed components. It represents a "healthy" array state. Notice that self-coupling terms, represented in white and located in the main diagonal, were not measured due to hardware limitations, however they are not necessary for calibration. On the other hand, the grids shown in cases (b), (c), and (d) represent the coupling values when component failures are present. By examining the differences between cases (b), (c), and (d) in comparison with the healthy case (a), it is possible correlate the errors to the failed component, ultimately diagnosing the array malfunction.

The diagnose begins with case (b), which compared to case (a) presents 3 rows with low power, -50 dB. The rows correspond to elements 11, 19, and 56. A row of low power signals indicates that the signals transmitted by the element corresponding to the row are not sensed by any element, thus, denoting the failure of the transmitting element. As a consequence, case (b) is indicating that the elements 11, 19, and 56 have completely failed in transmission. In addition, by inspection of the schematic given in Figure 5.4, it is possible to conclude that, within the transmission path, the component most likely to fail is the HPA. Hence, case (b) is the result of three failed HPAs.

On the other hand, case (c) conspicuously displays a large area of low power signals, possibly implying a major failure. The low power signals are found along rows, and also along columns. These results along rows indicate

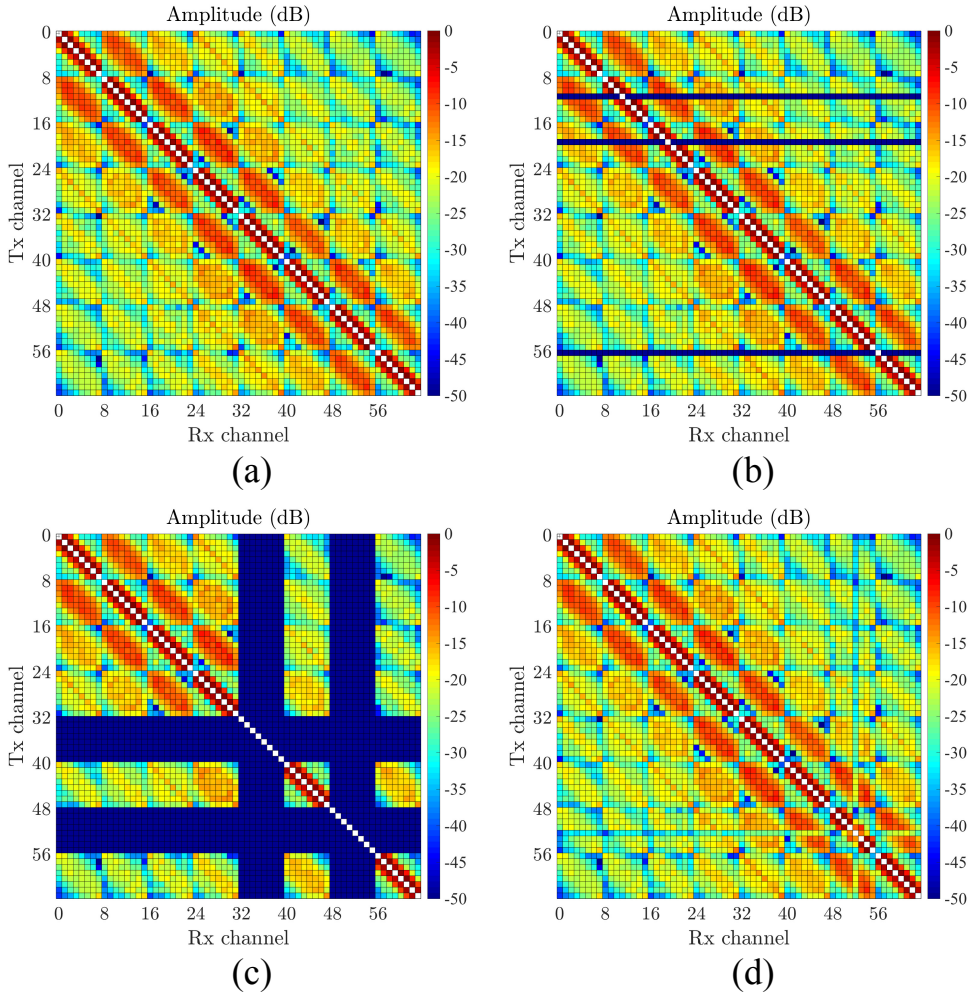

Figure 5.8: Examples of element failure depicted using coupling among elements of the phased array. Each pixel represents the amplitude in dB of the received signal on "Rx channel", transmitted by the "Tx channel". Case (a) represents a normal operation. Case (b) shows elements 11, 19, and 56 with damaged high power amplifiers. Case (c) depicts complete failure of the boards corresponding to PCB 04 and PCB 06. Finally, case (d) is the result of a bad antenna connection. Source: [104]

failed transmitting element, whereas, low signals along columns indicate failed elements in reception. The affected rows are the same as the affected columns, which correspond to elements 32 to 39, and 48 to 55. In addition, one can notice that the mentioned elements comprise TR module boards PCB 04 and

PCB 06, see Figure 5.4. Consequently, if all the elements that belong to boards PCB 04 and PCB 06 neither transmit nor receive, then both boards have completely failed. The components that cause this type of failure are the power supplies or voltage regulators, which later were confirmed to be damaged in this case.

In contrast to cases (b) and (c), that involved signal levels close to noise floor, Figure 5.8.(d) depicts only an attenuated signal at both transmission and reception for element 52. The attenuation value is $\approx$ 10 dB, calculated by either mutual coupling-based initial or in-situ techniques. This attenuation level is about four times the maximum peak-to-peak amplitude misalignment between elements, $\approx$ 2.5 dB, found using the park and probe technique (Figure 5.6.(d)). Thus, the issue stems from a more severe cause rather than a simple untuned attenuator or phase shifter. On the other hand, the cause is not as severe to completely disable the element, and thus there is no damaged active component. Thereby, the issue is likely to be a passive component as the antenna or transmission lines. It was verified that this particular error was caused by a bad connection between the antenna and the TR module board.

The cases reviewed demonstrated how the feedback obtained from mutual coupling measurements can quickly identify element failure, and be used for diagnosing component damage. It is important to notice that, even though the cases were illustrated using coupling data between all possible element pair combination, the diagnose will be possible using a reduced amount of data. For instance, the limited amount of data collected using the in-situ mutual coupling-based technique presented in Section 5.3, is just enough to diagnose failed components.

Additionally, data obtained from failed components should be left out of

the computation of mutual coupling-based techniques, since these techniques rely on relative ratios from element to element. Signals acquired using failed elements will bias the estimations of elements away from the reference. For this reason, before calculating the error ratios K^r and K^t, it is necessary to check for low power signals in the same manner as discussed in the previous paragraphs, identify possible failed components, and exclude them from the calculations. Methodologies on how to avoid faulty elements have already been presented in the literature, the reader can refer to [32, 106] for more information.

5.5 Chapter Summary

This Chapter successfully implemented mutual coupling-based initial and in-situ calibration techniques in the 8×8 active phased array LRU. The park and probe technique was compared to the mutual coupling-based technique by Bekers et al.; since the latter relies on symmetric coupling assumptions, the former technique was used as ground truth. It is found that phase estimations using the approach by Bekers et al. were fairly good, in the order of 2.5°. By contrast, the magnitude estimations are heavily affected by edge effects, making the estimations only acceptable for element subsets chosen away from the edges.

For the in-situ case, a phase and amplitude mutual coupling-based monitoring technique was adapted from the literature to be implemented in this case. The proposed hybrid technique allows to track excitation changes that may arise during fielded operation, and the current state can be calculated based on the state estimated by the initial calibration stage. The technique does not rely on the same assumptions as its initial type counterpart, and removes the

coupling values from the calculation. Thus, its misalignment estimations are more accurate, i.e., yielding a RMSE $< 1^{\circ}$ and < 0.12 dB, regardless of the size of the array. Moreover, diagnosis of component damage has been successfully demonstrated on real failure cases. It was found that mutual coupling measurements can be used as a fast feedback mechanism to identify component failure and bad connections across the array.

6 Conclusion

This work presented a compilation of research focused on calibration of phased arrays. Motivated by the goal to investigate possible calibration techniques for the APAR project by the NCAR-EOL, this research shows valuable experimental results from performing both current state-of-the-art and novel techniques on the LRU test-bed. In addition, instrumentation related to phased array characterization and calibration is also presented that shows commercial options and custom-made novel scanners specifically designed for phased array calibration applications.

Phased array calibration issues originate from the inherent excitation misalignment problem, which can have a random or systematic distribution. This research found that random misalignment errors are less impactful than systematic ones. A systematic error can focus the adverse effects of excitation errors on critical performance parameters of the phased array. The simulated example shown in Section 2.2 indicated that systematic errors, of 10° and 1 dB of RMSE can cause an intolerable SLL error of more than 10 dB. By contrast, for an equal level amplitude and phase RMSE, random errors result in only a 4 dB SLL error. After compensation is performed, the remaining misalignment is expected to be of random nature only. Moreover, in the past, great effort has been dedicated to finding the relationship between random amplitude and phase errors, and their effects on the synthesized pattern of the phased arrays. The error theory calculates that the beam pointing accuracy of the aforementioned simulated example is less than 0.005°, and its directivity can change by $\approx$ -0.2 dB. These degradations of performance are modest compared to the 4 dB SLL errors; thus, when testing phased arrays, the SLL is the most significant indicator of misalignment errors.

The extensive review of the state-of-the-art of current calibration techniques presented in Section 2.4 proposes to categorize them under different criteria. The categories are initial versus in-situ, external versus built-in, NF versus FF, specialized versus MC, and direct versus encoded. The most important category is initial vs. in-situ, because both types of calibrations are necessary in order to ensure the correct function of any phased array. Among all the cited techniques, the most common and straight-forward is the park and probe technique; however, it requires the employment of a robotic manipulator, and the AUT architecture must allow for only one element to be enabled, while the others should be terminated. The author prepared a useful summary, Table 2.4, that categorizes each of the cited sources according to the proposed criteria. In this manner, the reader can use the table as a catalogue to find literature related to the requirements of his/her application.

Chapter 3 presented the most common instrumentation for phased array measurement and calibration, the NF planar scanner. This scanner configuration offers the probe positioning capability required for park and probe tests. As an example, the commercial NF planar scanner located at the RIL was introduced. Its three linear actuators enable the scanner to position the probe anywhere in a 2D plane parallel to the array aperture, and a rotary joint allows dual polarization testing. In addition, as a more affordable option, the custom made planar scanner designed exclusively for LRU testing and calibration was also described. This scanner proved to be an excellent tool for characterizing the performance of the LRU, even though it is not suitable to perform NF to FF scans, as the commercial versions can. Finally, a new trend of using articulated robotic manipulators was discussed. Articulated manipulators often include more degrees of freedom in a compact packaging, which allows for ar-

bitrary scan grids that typically require several types of specialized hardware. Therefore, implementing robotic manipulators on antenna measurements allows more flexible scan geometry. However, they are recommended for higher frequency applications, when the AUTs are smaller.

Inspired by the new trend of implementing articulated robotics, the ARRC is developing its own phased array characterization tool. The RF scanner is a novel automatic tool conceived for phased array calibration, and based on a 6-degrees-of-freedom robotic arm. Its core function is to perform park and probe calibration of phased arrays, with a probe positioning accuracy of 100 μm. However, unlike regular antenna ranges, it also allows the user to control the environment temperature over a range of 0-50 °C. Moreover, its sensor suite includes an HD camera that enables inspection of the surface and, as a result, is used to locate the center of the phased array elements. The sensor suite also includes a thermal camera to capture pictures of the temperature distribution along the surface of the aperture. Preliminary results were taken to demonstrate these capabilities. This tool allows testing of high power phased array prototypes, many of which suffer from high-temperature gradients across their surface.

A full characterization and initial calibration procedure of the patterns of the LRU was presented in Chapter 4. It was demonstrated that the proposed procedure not only calibrated the excitation of the phased array, but also exhaustively characterized the TR modules behavior, and allowed the calibration engineer to collect enough information to permit pattern prediction as well. The proposed procedure implements the park and probe technique to quantify the misalignment between antenna elements, and to characterize the non-ideal behavior of the attenuators and phase shifters mounted on the TR modules.

It was found that, for higher levels of attenuation, there is an unwanted phase shift caused by the attenuator chip. Since this type of error is systematic, it can lead to a severe reduction of performance. The characterization process uncovers this error and allows it to be corrected. Thus, after compensation is applied, the systematic errors are removed, and the random errors are reduced to a minimum defined by the attenuation and phase shift resolution.

Additionally, the proposed initial calibration includes NF planar pattern scans of embedded element and beam-steered patterns. By measuring the embedded element pattern of each antenna element, the calibration engineer is collecting a set of patterns that can be post-processed to predict the array patterns. Moreover, by combining the collected embedded element patterns with the TR module data, more accurate array pattern prediction is achieved. The result is a digital tool that simulates any antenna pattern that can be synthesized by the AUT, considering both errors from the TR modules, and irregularities of the antenna pattern particular to the AUT. Experimental results demonstrated that the predicted patterns agree for the co-polar component of the fields. For the cross-polar component, the prediction is accurate off-boresight (error $\leq$ 1 dB), but on boresight, errors of $\approx$ 4 dB were found. The inaccuracies at boresight are due to the low SNR of the cross component fields in this area.

As an alternative to the use of external calibration instrumentation, mutual coupling-based techniques were tested. The approach by Bekers et al. proved to be the most accurate initial type mutual coupling-based calibration technique. The reason for this is its mathematical framework, which allows taking into consideration as much information as possible, and thus the error caused by the differences in coupling values is reduced by averaging. The es-

timation error results, obtained by experimentation, are $\approx 2.5^\circ$ in phase, and can be improved by extending the subarray size. On the other hand, amplitude error of ≈ 0.5 dB is obtained for a 6×6 subarray, but it reaches ≥ 1 dB when elements on the edges are considered in the calculations. From these results it is possible to infer that, for a larger array, phase estimations will have an error of $\leq 2.5^\circ$ regardless of the chosen subarray configuration, and amplitude estimation errors will be ≤ 0.5 dB, as long as elements on the edges are avoided. It was also noted that for vertically polarized microstrip patches the amplitude of the coupling between elements on the left and right columns suffers great variations when compared to that for coupling between elements on the inner columns. Therefore, to apply the approach by Bekers et al. it is advisable to avoid including elements located on the columns near the edges, or to add dummy elements surrounding the active elements.

This work proposes a hybrid in-situ calibration technique as a complement to the approach by Bekers et al. The hybrid technique tracks changes that occur after the initial calibration by comparing the before and after excitation states. To accomplish this, it employs all antenna elements to sample the coupling between them, which avoids the use of embedded antenna elements. Since the elements are coupled with their neighbors, the dynamic range problem, resulting from using embedded antenna elements, is avoided. The RMSE estimation errors are 0.75° in phase and 0.12 dB in amplitude, which are much lower than the in-situ case. In addition, the approach is also insensitive to edge effects, and is scalable, thus applicable to arrays of any size.

Finally, an important advantage of mutual coupling-based measurements is to identify component failure. Mutual coupling-based measurements proved to be a fast test to determine the health of antenna elements. Experiments show

that they not only detect failed antenna elements, but they also can identify what component has failed. Among the cases reviewed, the measurements revealed failed high power amplifiers and power supplies, and bad connections. The ability to identify failed components is crucial for mutual coupling-based calibrations, as algorithms for this type of calibration must avoid using data from a damaged element. Because malfunctioning components are harmful to the synthesized antenna pattern, it is important for the radar engineer to be aware of the of the problem so that attempts to correct such problems can be made

A NF planar measurements: Fundamentals and Technical Details

A.1 Near Field Planar System

Ideally antenna patterns should be measured by having an ideal plane wave source/receiver, rotating the AUT to the angular coordinates of interest and sampling the received signal at each position. A typical example of this is a Far-Field (FF) test, where the AUT is positioned far enough from an antenna probe, and the AUT is rotated to capture its antenna pattern at different angles. This is called a direct measurement, because the long probe-to-AUT distance directly collimates the radiated waves [107]. Other direct methods involve using lenses and/or reflective surfaces, as in compact antenna test ranges. On the other hand, for electrically large AUTs where the FF distance may be simply too large to arrange a direct test type, an indirect measurement is more convenient. Indirect methods are often tests that sample the AUT at its NF region, and later post-process the antenna patterns to a FF distances. Since the NF region is just a few wavelengths away from the AUT, shorter distances are needed and smaller chambers can be used.

NF tests are typically performed by planar, cylindrical and spherical systems, mainly because the required robotic mechanical scanners are relatively easy to build, and convenient mathematical approaches can be applied to process FF data from the sampled NF data, i.e., the Helmholtz equation is separable on these coordinate systems. Each system has its own advantages over the others; planar scans are used on high-gain antennas, spherical on omnidirectional antennas, and cylindrical on fan beam antennas. A list of the main differences can be found in Table A.1, which clearly indicates that, to

characterize, a high-gain antenna like the LRU, the suitable scan configuration should be planar.

Parameter	Planar	Cylindrical	Spherical
High-gain	excellent	good	good
Low-gain	poor	poor	excellent
Probe correction	simple	complex	complex
Speed	fast	slow	slow
Alignment	easy	difficult	more difficult

Table A.1: NF scan types classification, main differences and advantages. Source: [76]

The NF planar scanner used in this project is located at the Radar Innovation Laboratory, and was manufactured by NSI. The dimensions of its scanning windows are a horizontal span of 62.46 in, vertical of 62.46 in, and a short course of 4 in of transverse movement, which is used to finely adjust the probe-to-AUT distance. The window dimension defines the maximum FF angle range that can be measured, i.e., the larger the window, the wider the FF range that can be processed. The relation can be expressed as [76]

$$H = D + P + 2Ztan\theta, \tag{A.1}$$

where H is the scan height, D is the antenna aperture height, P is the probe height, Z is the probe-to-AUT distance, and θ is the maximum FF angle that can be accurately calculated. There is not enough information from the scan to obtain the pattern at angles $> |\theta|$ away from the boresight axis. For this project the values of H, D, P, Z, and θ are given in Table A.2. Notice that θ was defined as $65°$ because often there is no need to have information on the steering capability of a phased array above $45°$, and also a smaller angle results in a smaller scan height, which also translates to a lower scan time. The value of H was calculated using (A.1) for θ =$65°$.

Symbol	Magnitude	Value	Unit
D	Antenna aperture height	9	in
P	Probe height	1.872	in
H	Scan height	43.31	in
Z	Probe to AUT distance	7.57	in

Table A.2: Definition of the NF scan parameters

A.2 NF Probe Correction

All NF tests require the use of an antenna probe, and due to the fact that all antennas have their own radiation pattern, the data sampled by the probe is influenced by its own radiation. Hence, an essential step to process the FF patterns from NF sampled data is probe correction, which analytically removes the effect of the probe from the calculated FF pattern. An in depth revision of the theory behind planar NF to FF transformation is given by [108, 109]. The scans for this project were performed using a WR-187 open ended waveguide (OEWG).

In the case of planar NF, the probe correction is a straightforward procedure. However, as will be explained later, despite its relative simplicity, the accuracy of the technique to process the cross-polarization pattern is poor. The full probe correction in planar scans requires a deep knowledge of the co- and cross-polarization patterns of the probe, which, for an OEWG, are a broad beam for the co-, and a lower power beam with a narrow null along the principal planes for the cross-polarization, as shown in Figure A.1. Moreover, the alignment of the probe with respect to the AUT is crucial to the procedure. The boresight axes of both antennas should always be parallel, since any deviation will incur a systematic error and preclude the correct FF computation.

The mentioned misalignment issue is especially problematic for the compu-

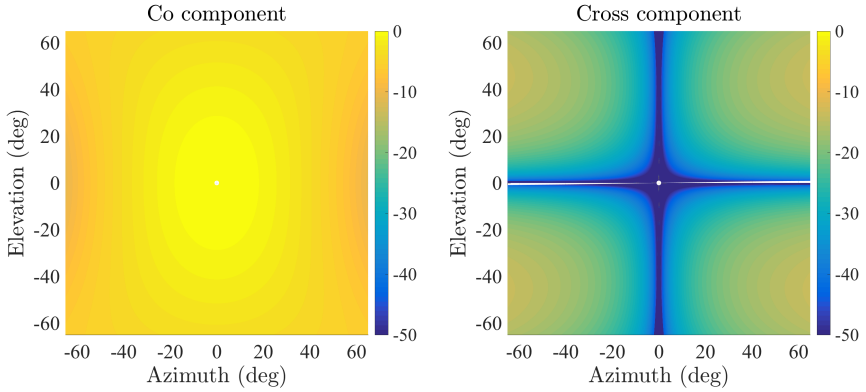

Figure A.1: Analytically computed co and cross patterns of an OEWG.

tation of the cross-polarization pattern of the AUT, which is heavily affected by the nature of the inherent cross-polarization of the probe. Since the cross-polarization pattern has a narrow null, any misalignment will misplace a deep null in a position where a higher signal was expected, rendering errors to the computation of the cross pattern of the AUT. Furthermore, it is not common to have an accurate measurement of the co- and cross-polarization patterns of the probe. However, due to its simple radiating mechanism the co-pattern is usually calculated, either analytically or by simulation, with sufficient accuracy.

Commercial scanners often employ an approximate technique instead of the full probe correction. The approximation assumes that the co-polarization is much larger than its cross counter-part, and simply neglects its value during the pattern correction. This approximation works very well for co-pattern computation, with errors <0.1 dB, although the cross-polarization may have errors of 3dB when using an OEWG with -40dB cross-polarization nulls to measure an AUT as APAR with -30dB level cross-polarization [110]. For this project, the probe correction was performed using the scanner software, which

employs the approximated probe correction.

A.3 Coordinate System and Polarization

The representation of an antenna pattern consists of quantifying the electric or magnetic vector fields over a section of the spatial domain. Usually, one plots the tangential components of the fields of the FF pattern at a finite number of sample points. The sample points are represented according to the selected coordinate system, and the tangential components, often named co- and cross-components, are represented according to the selected polarization. A great summary of this topic can be found in [111].

The antenna patterns plotted in this dissertation are described using Ludwig III definition, which is commonly use to plot any antenna pattern. However, according to [112], for microstrip patch antennas, the Ludwig II definition describes their polarization nature better because the cross-polarization component is closer to this definition rather than the third definition. The transformation from second to third definition is straight forward [111].

To further discuss the differences between Ludwig's second and third definitions, Figures A.2 and A.3 help to compare a beam-steered antenna pattern plot at Az = -45^o and El = 45^o for both definitions. Figure A.2 shows the antenna patterns for V polarization, while Figure A.3 shows the H polarization case. To the left of each figure is the Ludwig II representation, and on the right the Ludwig III. One can notice from Figure A.3 that the cross-polarization for the second definition is lower than in the third, demonstrating the statement made by [112].

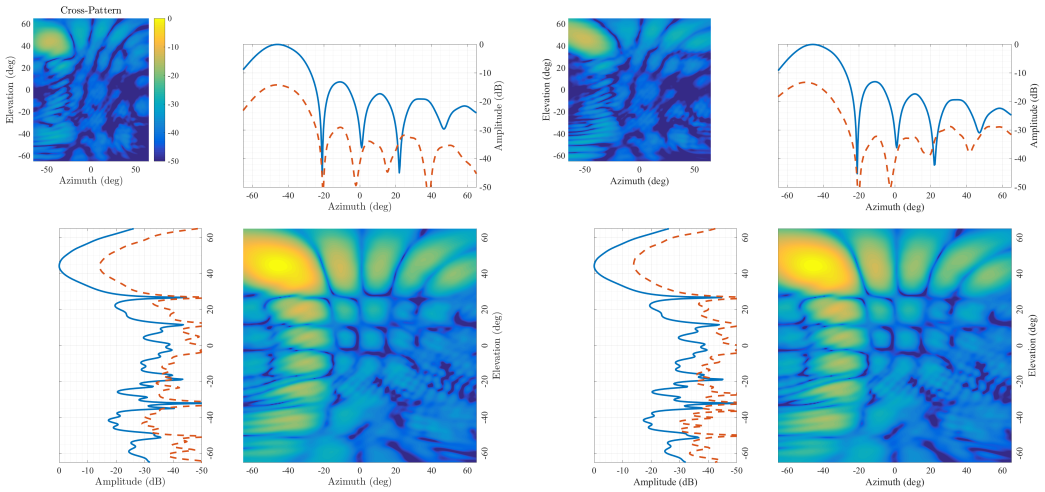

(a) Ludwig II definition, V polarization. (b) Ludwig III definition, V polarization.

Figure A.2: Ludwig II vs Ludwig III comparison, V polarization. Co-component indicated by continuous lines, and cross-components by dashed lines.

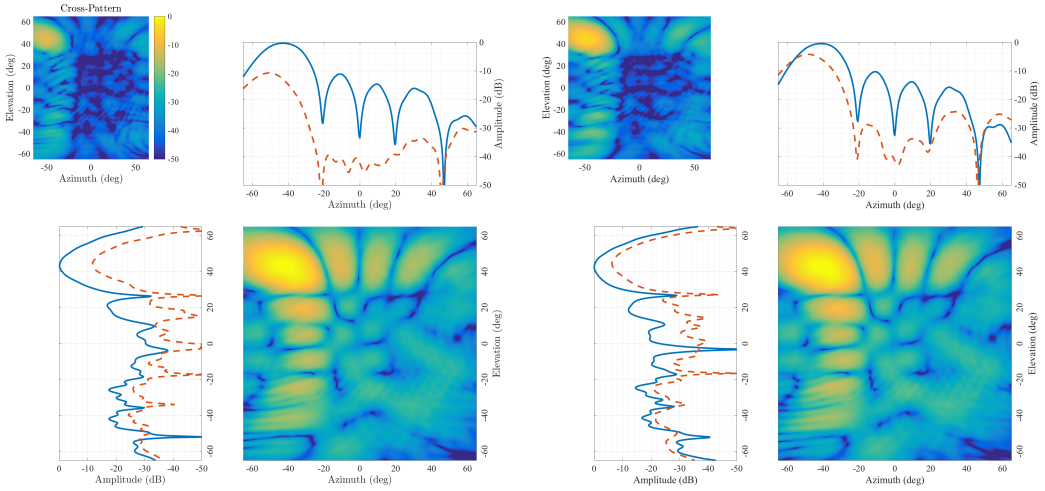

(a) Ludwig II definition, H polarization. (b) Ludwig III definition, H polarization.

Figure A.3: Ludwig II vs Ludwig III comparison, H polarization. Co-component indicated by continuous lines, and cross-components by dashed lines.

A.4 Antenna Fixture and Setup

For all tests, the antenna and its fixture rested on top of microwave absorber blocks as illustrated in Figure 4.5. The AUT was aligned to the waveguide

probe by positioning the probe in front the AUT's corners and measuring the Z distance between the probe's end and the AUT's corner, using a laser displacement sensor. The AUT is adjusted manually until the distance measured of all corners differ from each other by only 0.01 inch (25.5 um).

A.5 Array Interface

The complete procedure was commanded by an Excel macro written in Visual Basic. The script is executed on the PC controlling the scanner, as shown in Figure 4.4, and it defines, coordinates and executes all steps of the procedure. A typical program will setup the measurements parameters of the scanner, configure the AUT excitation, trigger a measurement, log the results and repeat for all required measurements.

The communication between the controlling PC and the APAR is via ethernet using a UDP protocol as required by the APAR. The macro sequentially sends the configuration commands to the AC controller, which will interpret the data and communicate with the TR modules to configure their phase and attenuation states accordingly.

A.6 Microwave Power Level

A C-band low-noise amplifier is added on the receiver port path. This amplification will provide a +3 dBm input power at the SMA connector of the antenna probe. The Minicircuits ZX60-83LN-12+ is used. The addition of the LNA improves the SNR level of the measurements. This is important because it enhances accuracy, especially when sampling individual channels of the TR module boards which yield considerable lower power.

Moreover, for the TR module characterization and pattern scans a +5dB

attenuator was added to the microwave circuit, immediately at the output of the LNA, because the extra +13dB is excessive when all TR modules are active. However, for embedded element pattern scans, the attenuator was removed.

B List of Abbreviations

5G	Fifth generation
APAR	Airborne phased array radar
ARRC	Advanced Radar Research Center
ATT	Attenuation
AUT	Antenna under test
CROMMA	Configurable robotic millimeter-wave antenna
DUT	Device under test
EOL	Earth Observing Laboratory
FF	Far field
HD	High definition
HPA	High power amplifier
LRU	Line replaceable unit
MC	Mutual coupling
MIMO	Multiple input multiple output
NCAR	National Center for Atmospheric Research
NF	Near field
OEWG	Open ended waveguide
PCB	Printed circuit board
PP	Park and probe
PS	Phase shift
REV	Rotation of electric vector
RF	Radio frequency
RMSE	Root mean squared error

Rx	Reception
SLL	Sidelobe level
SNR	Signa-to-noise ration
SW	Switch
TR	Transmit/Receive
Tx	Transmission
VB	Visual Basic
VNA	Vector network analyzer

References

[1] R. J. Mailloux, *Phased Array Antenna Handbook*, 2nd ed. Artech House, 2005.

[2] J. Ruze, "The Effect of Aperture Errors on the Antenna Radiation Pattern," *Il Nuovo Cimento*, vol. 9, no. 3 Supplement, pp. 364–380, 1952.

[3] J. L. Allen, "The Theory of Array Antennas," MIT Lincoln Laboratory, Tech. Rep., 1963.

[4] J. K. Hsiao, "Design of Error Tolerance of a Phased Array," *Electronics Letters*, vol. 21, no. 19, pp. 834–836, 1985.

[5] ——, "Array Sidelobes, Error Tolerance, Gain, and Beamwidth," 1984.

[6] D. N. McQuiddy Jr, R. L. Gassner, P. Hull, J. S. Mason, and J. M. Bedinger, "Transmit/receive module technology for X-band active array radar," *Proceedings of the IEEE*, vol. 79, no. 3, pp. 308–341, 1991.

[7] C. Parini, S. Gregson, J. McCormick, and D. J. V. Rensburg, *Theory and Practice of Modern Antenna Range Measurements*. IET, 2014.

[8] M. E. Weber, J. Y. Cho, J. S. Herd, J. M. Flavin, W. Benner, and G. Torok, "The Next-Generation Multimission U.S. Surveillance Radar Network," *Bulletin of the American Meteorological Society*, no. November 2007, pp. 1739–1752, 2007.

[9] B. J. E. Stailey and K. D. Hondl, "Multifunction Phased Array Radar for Aircraft and Weather Surveillance," *Proceedings of the IEEE*, vol. 104, no. 3, pp. 649–659, 2016.

[10] D. S. Zrnic, J. F. Kimpel, D. E. Forsyth, A. Shapiro, G. Crain, R. Ferek, J. Heimmer, W. Benner, T. J. McNellis, and R. J. Vogt, "Agile-beam Phased Array Radar for Weather Observations," *Bulletin of the American Meteorological Society*, no. November 2007, pp. 1753–1766, 1998.

[11] J. L. Salazar, "The Feasibility of Low-Cost , Dual-Polarized , Phase-Tilt Antenna Arrays for Dense Radar Networks," Ph.D. dissertation, University of Massachussetts Amherst, 2012.

[12] C. Fulton, G. Zhang, W. Bocangel, L. Lei, R. Kelley, and M. McCord, "Cylindrical Polarimetric phased array radar: A multi-function demonstrator and its calibration," *2013 IEEE International Conference on Microwaves, Communications, Antennas and Electronic Systems, COMCAS 2013*, no. October, pp. 1–5, 2013.

[13] D. S. Zrnic and R. J. Doviak, "System requirements for phased array weather radar," NOAA/NSSL, Tech. Rep., 2005.

[14] Y. Wang and V. Chandrasekar, "Polarization isolation requirements for linear dual-polarization weather radar in simultaneous transmission mode of operation," *IEEE Transactions on Geoscience and Remote Sensing*, vol. 44, no. 8, pp. 2019–2028, 2006.

[15] J. S. Herd, "Multifunction Phased Array Radar Panel," *Tech Notes*, vol. 13, no. 7, 2011.

[16] D. Schvartzman and S. Torres, "Distributed beams: A technique to reduce the scan time of an active rotating phased array radar system," in *AMS 100th Annual Meeting*, 2015.

[17] D. Conway, D. DuRussel, A. Morris, and C. Parry, "Multifunction Phased Array Radar Advanced Technology Demonstrator Nearfield Test Restults," in *2018 IEEE Radar Conference*, 2018, pp. 1412–1415.

[18] J. Vivekanandan, W.-C. Lee, E. Loew, J. L. Salazar, V. Grubišić, J. Moore, and P. Tsai, "The next generation airborne polarimetric Doppler weather radar," *Geoscientific Instrumentation, Methods and Data Systems*, vol. 3, no. 2, pp. 111–126, 2014.

[19] J. Vivekanandan, A. Karboski, and E. Loew, "Airborne Polarimetric Doppler Weather Radar : Antenna Aperture and Beam Forming Architecture," in *IEEE International Symposium on Phased Array Systems and Technology*, 2019.

[20] N. Peccarelli, B. James, R. Irazoqui, J. Metcalf, C. Fulton, and M. Yeary, "Survey: Characterization and Mitigation of Spatial/Spectral Interferers and Transceiver Nonlinearities for 5G MIMO Systems," *IEEE Transactions on Microwave Theory and Techniques*, vol. 67, no. 7, pp. 2829–2846, 2019.

[21] E. G. Larsson, O. Edfors, F. Tufvesson, and T. L. Marzetta, "Massive MIMO for next generation wireless systems," *IEEE Communications Magazine*, vol. 52, no. 2, pp. 186–195, 2014.

[22] A. Kawakubo, S. Tokoro, Y. Yamada, K. Kuroda, and T. Kawasaki, "Electronically-Scanning Millimeter-Wave RADAR for Forward Objects Detection," in *SAE Technical Paper*. SAE International, 2004. [Online]. Available: https://doi.org/10.4271/2004-01-1122

[23] R. H. Medina-sanchez, "Beam Steering Control System for Low-Cost Phased Array Weather Radars: Design and Calibration Techniques," Ph.D. dissertation, University of Massachusetts Amherst, 2013.

[24] R. C. Hansen, *Phased Array Antenna*, 2nd ed. Wiley-Interscience, 2009.

[25] K. R. Carver, W. K. Cooper, and W. L. Stutzman, "Beam-Pointing Errors of Planar-Phased Arrays," *IEEE Transactions on Antennas and Propagation*, vol. 21, pp. 199–202, 1973.

[26] M. I. Skolnik, "Nonuniform Arrays," in *Antenna Theory*, R. E. Collin and F. J. Zuker, Eds. McGraw-Hill, 1969, pp. 227–234.

[27] U. Hackenberg, H. Dreher, and R. Rieger, "Polarisation agile, highly accurate T/R-Module for Synthetic Aperture Radar," in *33rd European Microwave Conference*, 2003, pp. 875–878.

[28] J. K. Mulcahey and M. G. Sarcione, "Calibration and Diagnostics of the THAAD Solid State Phased Array in a Planar Nearfield Facility," *Proceedings IEEE International Conference on Phased Array Systems and Technology*, pp. 322–326, 1996.

[29] Y. Hwang, "Satellite Antennas," *Proceedings of the IEEE*, vol. 80, no. 1, pp. 183–193, 1992.

[30] C. Fulton, R. Palmer, M. Yeary, J. L. Salazar, H. Sigmarsson, M. E. Weber, and A. Hedden, "Horus: A Testbed for Fully Digital Phased Array Radars," *Microwave Journal*, pp. 20–34, 2020.

[31] C. J. Fulton, "Digital Array Radar Calibration and Performance Monitoring Techniques for Direct Conversion and Dual Polarization Architectures," Ph.D. dissertation, Purdue University, 2011.

[32] I. Şeker, "Calibration Methods for Phased Array Radars," *Proceedings of SPIE*, vol. 8714, pp. 87 140W–1 87 140W–15, 2013.

[33] M. G. Sarcione, J. K. Mulcahey, D. Schmidt, K. Chang, M. Russel, R. Enzmann, P. Rawlinson, W. Guzak, R. Howard, and M. Mitchell, "The Design, Development and Testing of the THAAD (Theater High Altitude Area Defense) Solid State Phased Array (formerly Ground Based Radar)," in *International Symposium on Phased Array Systems and Technology*, 1996, pp. 260–265.

[34] W. Haselwander, M. Uhlmann, S. Wustefeld, and M. Bock, "Measurement on an active phased array antenna on a near-field range and an anechoic far-field chamber," *2001 31st European Microwave Conference, EuMC 2001*, 2001.

[35] G. Sadowy, K. Brown, N. Chamberlain, H. Figueroa, C. Fisher, M. Grando, G. Hamilton, V. Vorperian, and M. Zawadzki, "UAVSAR active electronically-scanned array," *IEEE International Symposium on Phased Array Systems and Technology*, pp. 763–770, 2010.

[36] R. H. Medina, J. L. Salazar, E. J. Knapp, and D. J. McLaughlin, "Calibration and Validation of the CASA Phased Array Antenna," *European Microwave Week 2012: "Space for Microwaves", EuMW 2012, Conference Proceedings - 42nd European Microwave Conference, EuMC 2012*, pp. 940–943, 2012.

[37] N. Chamberlain, C. Andricos, A. Berkun, K. Kumley, V. Krimskiy, R. Hodges, and S. Spitz, "T/R module development for large aperture L-band phased array," *IEEE Aerospace Conference Proceedings*, 2005.

[38] M. Lorcher and H. Brugger, "Advanced RF sensors for SAR earth observation using high precision T/R-Modules," *Synthetic Aperture Radar (APSAR), 2011 3rd International Asia-Pacific Conference on*, pp. 1–6, 2011.

[39] J. G. Van Hezewijk, "Fast determination of the element excitation of active phased array antennas," *Antennas and Propagation Society Symposium 1991 Digest*, vol. 3, pp. 1478–1481, 1991.

[40] H. M. Aumann and F. G. Willwerth, "Phased-Array Calibration By Adaptive Nulling Lexington Massachusetts," Massachusetts Institute of Technology Lincoln Labs, Tech. Rep. May, 1991.

[41] C.-n. Hu, "A Novel Method for Calibrating Deployed Active Antenna Arrays," *IEEE Transactions on Antennas and Propagation*, vol. 63, no. 2, pp. 1650–1657, 2015.

[42] C. Fulton, J. L. Salazar, Y. Zhang, G. Zhang, R. Kelly, J. Meier, M. Mccord, D. Schmidt, A. D. Byrd, L. M. Bhowmik, S. Karimkashi, D. S. Zrnic, R. J. Doviak, A. Zahrai, M. Yeary, and R. D. Palmer, "Cylindrical Polarimetric Phased Array Radar: Beamforming and Calibration for Weather Applications," *IEEE Transactions on Geoscience and Remote Sensing*, vol. 55, no. 5, pp. 2827–2841, 2017.

[43] I. Ivić, C. Curtis, E. Forren, R. Mendoza, D. Schvartzman, S. Torres, D. J. Wasielewsk, and F. A. Zahrai, "An Overview of Weather Calibration for the Advanced Technology Demonstrator," in *IEEE International Symposium on Phased Array Systems and Technology*, 2019.

[44] W. P. M. N. Keizer, "An Overview of Test Techniques for Characterizing Active Phased Array Antennas," *Perspectives on Radio Astronomy_Technologies for Large Antenna Arrays, Netherland Foundation for Research in Astronomy*, no. January 2000, pp. 191–199, 1999.

[45] J. S. Herd, "Experimental results from a self-calibrating digital beamforming array," *Antennas and Propagation Society Internation Symposium*, no. AP-S Merging Technologies for the 90's, 1990.

[46] K. M. Lee, R. S. Chu, and S. C. Liu, "A Built-In Performance-Monitoring/Fault Isolation and Correction (PM/FIC) System for Active Phased-Array Antennas," *IEEE Transactions on Antennas and Propagation*, vol. 41, no. 11, pp. 1530–1540, 1993.

[47] E. Lier, D. Purdy, J. Ashe, and G. Kautz, "On-board integrated beam conditioning system for active phased array satellite antennas," *IEEE International Symposium on Phased Array Systems and Technology*, pp. 509–512, 2000.

[48] T. Takahshi, N. Nakamoto, M. Ohtsuka, T. Aoki, Y. Konishi, and M. Yajima, "A SIMPLE ON-BOARD CALIBRATION METHOD AND ITS ACCURACY FOR MECHANICAL DISTORTIONS OF SATELLITE PHASED ARRAY ANTENNAS," in *3rd European Conference on Antennas and Propagation*, no. 2, 2009, pp. 1573–1577.

[49] T. Takahashi, N. Nakamoto, M. Ohtsuka, T. Aoki, Y. Konishi, I. Chiba, and M. Yajima, "On-Board Calibration Methods for Mechanical Distortions of Satellite Phased Array Antennas," *IEEE Trans. Antennas Propag.*, vol. 60, no. 3, pp. 1362–1372, 2012.

[50] H. M. Aumann, a. J. Fenn, and F. G. Willwerth, "Phased Array Antenna Calibration and Pattern Prediction Using Mutual Coupling Measurements," *IEEE Transactions on Antennas and Propagation*, vol. 37, no. 7, pp. 844–850, 1989.

[51] C. Shipley and D. Woods, "Mutual Coupling-based Calibration of Phased Array Antennas," *Proceedings 2000 IEEE International Conference on Phased Array Systems and Technology*, pp. 0–3, 2000.

[52] T. Gao, Y. Guo, J. Wang, and X. Chen, "Large Active Phased Array Antenna Calibration," in *Antennas and Propagation Society International Symposium*, 2001, pp. 606–609.

[53] D. Bekers, R. Van Dijk, and F. Van Vliet, "Mutual-coupling based phased-array calibration: A robust and versatile Approach," *IEEE International Symposium on Phased Array Systems and Technology*, no. 1, pp. 630–637, 2013.

[54] A. Agrawal and A. Jablon, "A Calibration Technique for Active Phased Array Antennas," *Phased Array Systems and Technology*, pp. 223–228, 2003.

[55] C. Fulton and W. Chappell, "Calibration techniques for digital phased arrays," *2009 IEEE International Conference on Microwaves, Communications, Antennas and Electronics Systems, COMCAS 2009*, pp. 1–10, 2009.

[56] A. Mitchell, "Coupling-based wideband digital phased array calibration techniques," Master's Thesis, The University of Oklahoma, 2014.

[57] S. Mano and T. Katagi, "A Method for Measuring Amplitude and Phase of Each Radiating Element of a Phased Array Antenna," *Electronics and Communications in Japan*, vol. 65-B, no. 5, 1982.

[58] T. Takahashi, H. Miyashita, Y. Konishi, and S. Makino, "Theoretical study on measurement accuracy of rotating element electric field vector (REV) method," *Electronics and Communications in Japan, Part I: Communications (English translation of Denshi Tsushin Gakkai Ronbunshi)*, vol. 89, no. 1, pp. 22–33, 2006.

[59] T. Takahashi, Y. Konishi, S. Makino, H. Ohmine, and H. Nakaguro, "Fast Measurement Technique for Phased Array Calibration," *IEEE Transactions on Antennas and Propagation*, vol. 56, no. 7, pp. 1888–1899, 2008.

[60] T. Takahashi, S. Member, Y. Konishi, S. Member, and I. Chiba, "A Novel Amplitude-Only Measurement Method to Determine Element Fields in Phased Arrays," *IEEE Transactions on Antennas and Propagation*, vol. 60, no. 7, pp. 3222–3230, 2012.

[61] M. Liu and Z. Feng, "Combined Rotating-element Electric-field Vector (CREV) Method for nearfield Calibration of Phased Array Antenna," in *International Conference on Microwave and Millimeter Wave Technology*, 2007, pp. 3–6.

[62] R. Long, J. Ouyang, F. Yang, W. Han, and L. Zhou, "Fast Amplitude-Only Measurement Method for Phased Array Calibration," *IEEE Transactions on Antennas and Propagation*, vol. 65, no. 4, pp. 1815–1822, 2017.

[63] T. Moon, J. Gaun, and H. Hassanieh, "Online Millimeter Wave Phased Array Calibration Based on Channel Estimation," *2019 IEEE 37th VLSI Test Symposium (VTS)*, pp. 1–6, 2019.

[64] S. D. Silverstein and S. Member, "Application of Orthogonal Codes to the Calibration of Active Phased Array Antennas for Communication Satellites," *IEEE Transactions on Signal Processing*, vol. 45, no. 1, pp. 206–218, 1997.

[65] S. D. Silverstein, "Algorithms for Remote Calibration of Active Phased Array Antennas for Communication Satellites," in *Conference Record of The Thirtieth Asilomar Conference on Signals, Systems and Computers*, 1997, pp. 1181–1185.

[66] D. S. Purdy, "An Automated Process for Efficiently Measuring the Patterns of All Elements Located in a Phased-Array Antenna," in *Proceedings 2000 IEEE International Conference on Phased Array Systems and Technology (Cat. No.00TH8510)*, vol. 00, no. c, 2000, pp. 1–4.

[67] E. Lier, M. Zemlyansky, D. Purdy, and D. Farina, "Phased Array Calibration and Characterization Based on Orthogonal Coding: Theory and Experimental Validation," *Phased Array Systems and Technology (ARRAY), 2010 IEEE International Symposium on*, pp. 271–278, 2010.

[68] Y. Lin, X. Bu, W. Zhao, and S. Wang, "A Parallel Calibration Method for Phased Array Antennas with Orthogonal and Nonorthogonal Codes," *2015 10th International Conference on Communications and Networking in China (ChinaCom)*, pp. 883–886, 2015.

[69] R. Long, J. Ouyang, F. Yang, W. Han, and L. Zhou, "Multi-Element Phased Array Calibration Method by Solving Linear Equations," *IEEE Transactions on Antennas and Propagation*, vol. 65, no. 6, pp. 2931–2939, 2017.

[70] F. Zhang, W. Fan, Z. Wang, Y. Zhang, G. F. Pedersen, A. S. Model, and B. Ax, "Improved Over-the-Air Phased Array Calibration Based on Measured Complex Array Signals," *IEEE Antennas and Wireless Propagation Letters*, vol. 18, no. 6, pp. 1174–1178, 2019.

[71] A. O. Fadamiro, A. A. Semomhe, O. J. Famoriji, and F. Lin, "A Multiple Element Calibration Algorithm for Active Phased Array Antenna," *IEEE Journal on Multiscale and Multiphysics Computational Techniques*, vol. 4, pp. 163–170, 2019.

[72] P. L. Ransom and R. Mittra, "A Method of Locating Defective Elements in Large Arrays," *Proceedings Letters of the IEEE*, vol. 58, pp. 1029–1030, 1970.

[73] J. J. Lee, E. M. Ferren, D. P. Woollen, and K. M. Lee, "Near-Field Probe Used as a Diagnostic Tool to Locate Defective Elements in an Array Antenna," *IEEE Trans. Antennas Propag.*, vol. 36, no. 6, pp. 884–889, 1988.

[74] H. Steyskal and J. S. Herd, "Mutual Coupling Compensation in Small Array Antennas," *IEEE Transactions on Antennas and Propagation*, vol. 38, no. 12, pp. 1971–1975, 1990.

[75] P. Darwood, P. Fletcher, and G. Hilton, "Mutual coupling compensation in small planar array antennas," *IEEE Proceedings - Microwaves,*

Antennas and Propagation, vol. 145, no. 1, p. 1, 1998. [Online]. Available: http://digital-library.theiet.org/content/journals/10.1049/ip-map_19981450

[76] D. Slater, *Near-Field Antenna Measurements*. Artech House, 1991.

[77] R. Sauerman, "A compact antenna test range built to meet the unique testing requirements for active phased array antennas," 1999.

[78] J. A. Gordon, D. R. Novotny, M. H. Francis, R. C. Wittmann, M. L. Butler, A. E. Curtin, and J. R. Guerrieri, "Millimeter-Wave Near-Field Measurements Using Coordinated Robotics," *IEEE Transactions on Antennas and Propagation*, vol. 63, no. 12, pp. 5351–5362, 2015.

[79] J. A. Gordon, D. Novotny, M. Francis, R. Wittmann, M. Butler, and J. Guerrieri, "The CROMMA Facility at NIST Boulder: A Unified Coordinated Metrology Space for Millimeter-Wave Antenna Characterization," *AMTA 36th Annual Meeting and Symposium*, pp. 351–356, 2014.

[80] D. Novotny, J. Gordon, and J. Guerrieri, "Antenna Alignment and Positional Validation of a mmWave Antenna System Using 6D Coordinate Metrology," *AMTA 36th Annual Meeting and Symposium*, pp. 247–252, 2014.

[81] A. C. Newell, "Error Analysis Techniques For Planar NF," *IEEE Trans. Antennas Propag.*, vol. 36, no. 6, 1988.

[82] L. Boehm, F. Boegelsack, M. Hitzler, and C. Waldschmidt, "An automated millimeter-wave antenna measurement setup using a robotic arm," *IEEE Antennas and Propagation Society, AP-S International Symposium (Digest)*, vol. 2015-Octob, pp. 2109–2110, 2015.

[83] P. A. Slater, J. M. Downey, M. T. Piasecki, and B. L. Schoenholz, "Portable laser guided robotic metrology system," *41st Annual Symposium of the Antenna Measurement Techniques Association, AMTA 2019 - Proceedings*, pp. 1–6, 2019.

[84] A. Mancini, J. L. Salazar, R. M. Lebrón, and B. L. Cheong, "A novel instrument for real-time measurement of attenuation of weather radar radome including its outer surface. Part I: The concept," *Journal of Atmospheric and Oceanic Technology*, vol. 35, no. 5, pp. 953–973, 2018.

[85] ——, "A novel instrument for real-time measurement of attenuation of weather radar radome including its outer surface. Part II: Applications," *Journal of Atmospheric and Oceanic Technology*, vol. 35, no. 5, pp. 975–991, 2018.

[86] R. M. Lebron, J. L. Salazar, C. Fulton, S. Duthoit, D. Schmidt, and R. Palmer, "A novel near-field robotic scanner for surface, RF and thermal characterization of millimeter-wave active phased array antenna," *IEEE International Symposium on Phased Array Systems and Technology*, vol. 0, pp. 1–6, 2016.

[87] D. Schmidt, J. L. Salazar-Cerreno, R. D. Palmer, C. Fulton, R. M. Lebrón, S. Duthoit, A. Mancini, M. McCord, J. Meier, and R. C. Kelley, "Radio Frequency Scanner," 2018.

[88] U. Robots, "Technical Specifications UR10," 2014. [Online]. Available: https://www.universal-robots.com/media/50880/ur10_bz.pdf

[89] D. J. Van Rensburg, B. Walkenhorst, Q. Ton, and J. Demas, "A robotic near-field antenna test system relying on non-canonical transformation

techniques," *41st Annual Symposium of the Antenna Measurement Techniques Association, AMTA 2019 - Proceedings*, 2019.

[90] J. D. Díaz, J. L. Salazar-cerreno, J. A. Ortíz, N. A. Aboserwal, R. M. Lebrón, C. Fulton, and R. D. Palmer, "A Cross-Stacked Radiating Antenna With Enhanced Scanning Performance for Digital Beamforming Multifunction Phased-Array Radars," *IEEE Trans. Antennas Propag.*, vol. 66, no. 10, pp. 5258–5267, 2018.

[91] J. A. Ortiz, J. L. Salazar-cerreno, J. D. Diaz, R. M. Lebrón, N. A. Aboserwal, and L. Jeon, "Low-Cost CMOS Active Array Solution for Highly-Dense X-band Weather Radar Network," *IEEE Transactions on Antennas and Propagation*, vol. XX, no. Xx, pp. 1–10, 2020.

[92] D. F. Kelley, "Embedded element patterns and mutual impedance matrices in the terminated phased array environment," *IEEE Antennas and Propagation Society, AP-S International Symposium (Digest)*, vol. 3 A, no. 1, pp. 659–662, 2005.

[93] P. Couper, K. Thompson, R. Davis, and T. Barnes, "Active Array High-Power Superposition Near-Field Measurement Technique: Restults, Analysis, and Practical Considerations," in *Proc. of Antenna Measurement Techniques Association*, 2000, pp. 198–203.

[94] K. Hassett, "Phased Array Antenna Calibration Measurement Techniques and Methods," in *European Conference on Antennas and Propagation*, 2016.

[95] D. F. Kelley, "Array Antenna Pattern Modeling Methods That Include Mutual Coupling Effects," *IEEE Trans. Antennas Propag.*, vol. 41, no. 12, pp. 1625–1632, 1993.

[96] R. Lebrón, J. D. Diaz, and J. L. Salazar-cerreno, "A Procedure to Characterize and Predict Active Phased Array Antenna Radiation Patterns from Planar Near-Field Measurements," in *Annual Meeting and Symposium of the Antenna Measurement Techniques Association*, 2018.

[97] N. A. Aboserwal, C. A. Balanis, and C. R. Birtcher, "Impact of finite ground plane edge diffractions on radiation patterns of aperture antennas," *Progress In Electromagnetics Research B*, vol. 55, no. 55, pp. 1–21, 2013.

[98] ——, "Coated ground plane edge diffractions and amplitude patterns of coated circular apertures," *IEEE Antennas and Propagation Society, AP-S International Symposium (Digest)*, pp. 2226–2227, 2014.

[99] ——, "Impact of coated ground-plane edge diffractions on amplitude patterns of circular apertures," *IEEE Antennas and Wireless Propagation Letters*, vol. 14, pp. 221–224, 2015.

[100] J. L. Salazar, N. Aboserwal, J. D. Díaz, J. A. Ortiz, and C. Fulton, "Edge diffractions impact on the cross polarization performance of active phased array antennas," in *2016 IEEE International Symposium on Phased Array Systems and Technology (PAST)*, 2016, pp. 1–5.

[101] J. A. Ortiz, N. Aboserwal, and J. L. Salazar, "A New Analytical Model Based on Diffraction Theory for Predicting Cross-polar Patterns of Antenna Elements in a Finite Phased Array," in *2019 IEEE International*

Symposium on Phased Array Systems and Technology (PAST), 2019, pp. 1–4.

[102] C. A. Balanis, *Antenna Theory: Analysis and Design*, 3rd ed. Wiley-Interscience, 2005.

[103] A. Mancini, R. M. Lebron, and J. L. Salazar, "The Impact of a Wet S-Band Radome on Dual-Polarized Phased-Array Radar System Performance," *IEEE Transactions on Antennas and Propagation*, vol. 67, no. 1, pp. 207–220, 2019.

[104] R. M. Lebrón, P.-s. Tsai, J. Emmett, C. Fulton, and J. L. Salazar-Cerreno, "Validation and Testing of Initial and Calibration of a Dual-polarized Active Phased Array Antenna," *IEEE Access*, vol. 4, 2020.

[105] C. Fulton and J. Salazar, "Polarimetric Phased Array Calibration for Large- Scale Multi-Mission Radar Applications," *2018 IEEE Radar Conference (RadarConf18)*, pp. 1272–1277, 2018.

[106] Y. Niedman, R. Shavit, and A. Bronshtein, "Diagnostic of phased arrays with faulty elements using the mutual coupling method," *IET Microw. Antennas Propag.*, vol. 3, no. 2, pp. 235–241, 2009.

[107] S. Gregson, J. McCormick, and C. Parini, *Principles of Planar Near-Field Antenna Measurements*. The Institution of Engineering and Technology, 2007.

[108] A. G. Repjar, A. C. Newell, and M. H. Francis, "Accurate Determination of Planar Near-Field Correction Parameters for Linearly Polarized," *IEEE Trans. Antennas Propag.*, vol. 36, no. 6, pp. 855–868, 1988.

[109] D. M. Kerns, "Plane-Wave Scattering-Matrix Theory of Antennas and Antenna-Antenna Interactions : Formulation and Applications," *Journal of the National Bureau of Standards*, vol. 80, no. 1, pp. 5–51, 1976.

[110] F. Boldissar and A. Haile, "Near Field Measurement Errors Due To Neglecting Probe Cross-Polarization," in *AMTA*, no. 1, 2007.

[111] G. F. Masters and S. F. Gregson, "Coordinate system plotting for antenna measurements," in *AMTA 29th Annual Symposium of the AMTA*, 2007.

[112] N. A. Aboserwal, J. L. Salazar, S. Member, J. A. Ortiz, S. Member, J. D. Díaz, S. Member, C. Fulton, S. Member, and R. D. Palmer, "Source Current Polarization Impact on the Cross-Polarization Definition of Practical Antenna Elements : Theory and Applications," vol. 66, no. 9, pp. 4391–4406, 2018.